Spectroscopy of exciton-polaritons in Cu_2O and GaAs-based microcavities

Dissertation

presented to the Faculty of Physics of the
TU Dortmund University, Germany,
in partial fulfillment of the requirements
for the degree of

Doktor rer. nat.

by
Johannes Schmutzler

technische universität
dortmund

Dortmund, October 2014

Accepted by the Faculty of Physics of the TU Dortmund University, Germany.

Day of the oral examination: 14th November 2014

Examination board:
Prof. Dr. Manfred Bayer
Prof. Dr. Metin Tolan
Prof. Dr. Heinrich Päs
Dr. Bärbel Siegmann

Contents

Chapter 1

Motivation

The discovery of the giant magnetoresistance (GMR) effect at the end of the 1980s [1, 2] is considered as a textbook example of the influence of fundamental research on our everyday life on a short timescale. Less than 10 years later, hard disk drives with read heads using the GMR-effect, allowing for a further increase of data storage density, have already been commercially available [3].

Another class of devices which is expected to be affected by fundamental research in the next decades are integrated circuits. For about 50 years Moore's empirical law has accurately described the increasing integration level, which predicts a doubling of the number of components per chip roughly every 24 months. However, when structure sizes will reach the range between $5-7$ nm during the years $2020-2025$, conventional complementary metal-oxide-semiconductor (CMOS) technology is expected to be exhausted [4]. To achieve a further gain of computational power, several concepts such as vertical integration of layers with active electronic components [5], semiconductor based spintronics [6] or quantum computation [7] have been intensely studied in the last decades.

Very recently there was a debate if all-optical logic circuits could provide a significant contribution for future computation devices [8–11]. In its course, major challenges for all-optical circuits to compete with state-of the art CMOS technology regarding device footprint, energy consumption and production costs have been outlined [9–11]. Nevertheless, there is the hope that all-optical circuits could be superior to current CMOS-technology regarding heat dissipation and operation speed [8, 12].

A very promising system for the realization of all-optical logic circuits are exciton-polaritons in semiconductor microcavities. Exciton-polaritons are light-matter quasiparticles, the theoretical concept of which was developed in the 1950s [13–16], and intensely studied in the following decades in bulk material. The observation of strong coupling between photons and excitons in semiconductor microcavities in 1992 [17] stimulated two discoveries, which might pave the way towards an all-optical logic circuit: Firstly, the realization of an electrically pumped polariton laser [18–20], which operates without occupation inversion and is therefore expected to be more efficient with respect to power consumption as compared to conventional semiconductor lasers [21]. Secondly, the demonstration of an all-optical polariton transistor [22], which fulfills several essential requirements for the operation of a logic device such as cascadability and logic gate operation [9, 12, 23].

However, the realization of devices based on exciton-polaritons is still in the proof of principle stage and up to now it is not clear if there will be a technological impact comparable to the discovery of the GMR-effect. Nevertheless, exciton-polaritons provide an ideal system to study a broad spectrum of fundamental physical phenomena such as polariton condensation which is closely related to Bose-Einstein-Condensation (BEC) [24], harmonic oscillator potentials [25], Josephson oscillations [26] and superfluid phenomena [27–30].

The scope of this thesis is twofold: On the one hand a contribution to the understanding of the fundamental physics of exciton-polaritons in semiconductors shall be provided, on the other hand the potential for prospective applications such as polariton lasing devices and all-optical integrated circuits shall also be evaluated.

The structure of this thesis is as follows: In chapter 2 a comprehensive overview of the concept of exciton-polaritons in semiconductors is given. In its course, similarities and fundamental differences between polaritons in bulk materials as well as in microcavities are elucidated. Furthermore, an introduction into the physics of BEC and its application to polariton condensates in microcavities is provided.

Chapter 3 focuses on spectroscopy of polaritons in bulk materials. As outlined in chapter 2, semiconductor crystals of very high quality are required for the observation of signatures of polaritons in bulk materials, which are provided by high-quality natural Cu_2O crystals. While the energetically lowest exciton-polariton series, which is known as the so-called yellow series, has been investigated in detail in Cu_2O, only little is known about the higher lying exciton-polariton series. Using two single frequency lasers in the visible and infrared spectral range, respectively, the blue exciton-polariton is investigated in this chapter by means of sum-frequency generation. The main result is the observation of a coherent propagation of the blue exciton-polariton over macroscopic distances despite a large absorption coefficient in this spectral region.

In chapter 4 the feasibility of different types of polariton based laser operation in a microcavity is evaluated for the case of GaAs-based compound semiconductors. In the first part of this chapter, workable operating parameters for a polariton laser in the visible spectral range are investigated. Among other things, an upper bound of 90 K for the lattice temperature is determined. The second part deals with the evaluation of a new concept for a terahertz lasing source [31], in which the transition between the dark $2p$ exciton state and the lower polariton state shall be exploited by means of two-photon pumping of the $2p$ state. A prerequisite for an actual detection of terahertz radiation according to this concept is a detailed understanding of the two-photon processes occurring in a microcavity, which is provided in this chapter.

Chapter 5 deals with different aspects of the propagation of polariton condensates in GaAs-based microcavities exhibiting high quality factors on the order of 10000. In the first part of this chapter, propagating polariton condensates in a photonic wire are considered, which are injected by non-resonant optical excitation. In this connection, the interaction between the polariton condensate and background carriers is studied by two complementary experimental techniques, namely a second order correlation measurement as well as a Young's double-slit experiment. The key finding here is a pronounced decrease of coherence of the polariton condensate mediated by interaction with the background carriers. The second part of this chapter elucidates the feasibility to steer and manipulate polariton condensates by reconfigurable optically induced potentials, which might pave the way towards all-optical logic circuits based on microcavity polaritons.

Finally, in chapter 6, a comprehensive summary and conclusion of the key results of this thesis is provided as well as an outlook for further investigations based on the results presented in this work.

Chapter 2

Exciton-Polaritons

In this chapter the fundamental properties of exciton-polaritons (in the following the term polariton will be used as a synonym for exciton-polariton) are introduced. As a starting point the seminal work of Hopfield [15], who launched the quantum mechanical theory of polaritons together with Fano [14] and Agranovich [16], is briefly reviewed. This is followed by an analysis of the Jaynes-Cummings Hamiltonian in the rotating wave approximation [32] and a detailed discussion of the physical requirements for the validity of the polariton concept. Thereafter, polaritons in semiconductor microcavities are introduced using the Jaynes-Cummings Hamiltonian. In the final part of this chapter the fundamental concepts of BEC are explained and applied to microcavity polaritons.

2.1 Hopfields description of polaritons and rotating wave approximation

The elementary excitations of the electronic system of a semiconductor which possesses the lowest energy are the so-called excitons. Excitons are bound quasiparticles which consist of a hole in the valence band and an electron in the conduction band. The energetic states of an exciton can usually be described in the framework of the Bohr model:

$$E_n(\mathbf{k}) = E_g - \frac{R^*}{n^2} + \frac{\hbar^2 k^2}{2M},\ n = 1{,}2{,}... \tag{2.1}$$

where R^* is the effective Rhyberg constant, also known as exciton binding energy, E_g the bandgap energy, k the wavenumber and $M = m_e^* + m_h^*$ the total mass of the electron and the hole, respectively. Depending on the semiconductor material the effective Rhyberg constant lies in a range of $1 - 100$ meV, for example $R^* = 4.2$ meV in GaAs [33] and $R^* \approx 100$ meV in Cu_2O [34][*]. The third term in Eq. (2.1) describes the kinetic energy, which is also known as spatial dispersion. Here, a parabolic dispersion is assumed which

---

[*] Here it should be mentioned that the energetic structure of the yellow exciton series in Cu_2O is not completely captured by the hydrogen model. Whereas the effective Rhyberg constant $R^* \approx 100$ meV describes accurately the higher energy states $n \geq 2$ of the yellow exciton in Cu_2O, the exciton binding energy amounts to $E_b = 153$ meV [35]. The deviation of the $1s$ state arises mainly due to the fact that the Bohr radius of the lowest exciton is on the order of magnitude of the lattice constant and the nonparabolicities of the bands have to be taken into account [35].

is a valid approximation near the band minima.

When excitons couple to the light field (so-called bright excitons), interaction effects between photons and excitons have to be considered. Depending on the interaction strength, the experimental approach and the quality of the investigated sample (see Sec. 2.2 for further details), these interaction can be treated as small perturbation where photons and excitons remain eigenstates of the system (the so-called weak coupling regime), or new eigenstates, which are called polaritons, are generated due to the interaction (the so-called strong coupling regime). Within this section the latter case will be discussed.

In Refs. [15, 16] the second-quantized Hamiltonian, which describes the photons, excitons and their mutual interaction, is derived. As an approximation only quadratic terms are considered, which allows for an analytical diagonalization of the corresponding Hamiltonian. Damping effects mediated by exciton-phonon interaction or terms of higher order are not considered within this model. In Ref. [36] the model was extended for spatial dispersion effects of the excitonic resonance according to Eq. (2.1). The resulting Hamiltonian reads [37]

$$\begin{aligned} H &= \sum_{\gamma}[\hbar c' k(a_{\gamma}^{\dagger}a_{\gamma}+\frac{1}{2})+\hbar\omega_{ex,\gamma}(b_{\gamma}^{\dagger}b_{\gamma}+\frac{1}{2}) \\ &+ iC_{\gamma}(a_{\gamma}^{\dagger}+a_{-\gamma})(b_{\gamma}-b_{-\gamma}^{\dagger})+D_{\gamma}(a_{\gamma}^{\dagger}+a_{-\gamma})(a_{\gamma}+a_{-\gamma}^{\dagger})], \end{aligned} \tag{2.2}$$

where

$$\hbar\omega_{\mathrm{ex},\gamma} = \hbar\omega_0+\frac{\hbar^2k^2}{2M}, \tag{2.3}$$

$$C_{\gamma} = \hbar\omega_0\left[\frac{\pi\beta\omega_{\mathrm{ex},\gamma}}{c'k\epsilon_b}\right]^{\frac{1}{2}}, \tag{2.4}$$

$$D_{\gamma} = \hbar\omega_0\frac{\pi\beta\omega_{\mathrm{ex},\gamma}}{c'k\epsilon_b}, \tag{2.5}$$

$$c' = \frac{c}{\sqrt{\epsilon_b}}. \tag{2.6}$$

$\gamma = (\mathbf{k}, p)$ is a combined index which accounts for the wavevector $\mathbf{k}$ and the polarization p for the two transverse electromagnetic modes.† β (ϵ_b) denotes the polarizability (background dielectric constant). $a_{\gamma}^{\dagger}$ ($b_{\gamma}^{\dagger}$) is the photonic (excitonic) creation operator and a_{γ} (b_{γ}) is the photonic (excitonic) annihilation operator. The first two terms in Eq. (2.2) describe the non-interacting photons and excitons, respectively. The third term considers exciton-photon interactions, the fourth photon-photon interactions. The introduction of polariton operators, which are linear combinations of the photon and exciton operators, allows for the calculation of the eigenvalues and eigenstates of the Hamiltonian in Eq. (2.2). This yields an eigenvalue problem and the expansion coefficients of the polariton operators as well as the eigenvalues can be determined analytically. This approach is known as Hopfield-transformation in this context, further details can be found in Refs. [15, 36, 37].

---

† $-\gamma$ means $-\gamma = (-\mathbf{k}, p)$.

However, for the description of polaritons in this thesis the Hamiltonian in Eq. (2.2) is further simplified. Firstly, the photon-photon interaction term is neglected, which corresponds to the $\mathbf{A}^2$-term arising from the minimal substitution of the momentum-operator $\hat{\mathbf{p}} \rightarrow (\hat{\mathbf{p}} - q\mathbf{A})$ in the semiclassical treatment of quantum mechanics. Secondly, antiresonant contributions $a_\gamma^\dagger b_\gamma^\dagger$ $(a_\gamma b_\gamma)$, which describe the simultaneous creation (annihilation) of a photon and an exciton, are not considered. This approach is known as rotating wave approximation, the corresponding Hamiltonian is called Jaynes-Cummings Hamiltonian [32]. Finally, the vacuum energy is neglected, since an occupation number of $\langle a_\gamma^\dagger a_\gamma \rangle >> 1$ for photons ($\langle b_\gamma^\dagger b_\gamma \rangle >> 1$ for excitons) is expected. The simplified Hamiltonian reads

$$\begin{aligned} H &= H_{\text{photon}} + H_{\text{exciton}} + H_{\text{interaction}} = \\ &= \sum_\gamma [\hbar c' k a_\gamma^\dagger a_\gamma + \hbar\omega_{ex,\gamma} b_\gamma^\dagger b_\gamma + \frac{\hbar\Omega_\gamma}{2}(a_\gamma^\dagger b_\gamma + a_\gamma b_\gamma^\dagger)], \end{aligned} \tag{2.7}$$

where $\frac{\hbar\Omega_\gamma}{2}$ corresponds to C_γ defined in Eq. (2.4). One obtains the following relation [37]

$$\hbar\Omega_\gamma = \left(\frac{k_0}{k}\right)^{\frac{1}{2}} \hbar\Omega_{\text{r}}, \tag{2.8}$$

where k_0 is the wavenumber at crossing point of the photon and exciton dispersion and $\hbar\Omega_r$ is the so-called Rabi splitting. Near the crossing point of the photon and exciton dispersion, i.e. $k \rightarrow k_0$, $\hbar\Omega_\gamma \approx \hbar\Omega_{\text{r}}$ can be assumed.

The rotating wave approximation holds as long as the Rabi splitting is significantly smaller compared to the exciton transition energy, which is typically the case for excitonic transitions in the visible spectral range in anorganic semiconductors. The GaAs-based microcavity structures investigated in this thesis, for example, exhibit a Rabi splitting of $\hbar\Omega_{\text{r}} \approx 10$ meV, whereas the exciton transition energy is $\hbar\Omega_{\text{ex}} \approx 1600$ meV.

However, for intersubband transitions between quantized subbands of quantum wells [38] and cyclotron resonances of a high-mobility two-dimensional electron gas [39], the Rabi splitting can lie in the same order of magnitude as the transition energy of the unperturbed system. In this connection, the antiresonant contributions $a_\gamma^\dagger b_\gamma^\dagger$ $(a_\gamma b_\gamma)$ have to be considered and the rotating wave approximation breaks down [40, 41]. In this case one typically speaks of the ultrastrong coupling regime.

As no interaction between states with different wavevectors $\mathbf{k}$ and polarization p is included in the Hamiltonian of Eq. (2.7), the corresponding eigenvalue problem can be solved for each wavevector $\mathbf{k}$ independently. Therefore the Hamiltonian can be rewritten in the following matrix representation

$$H = \begin{pmatrix} E_{\text{ph}}(\mathbf{k}) & \frac{\hbar\Omega_{\text{r}}}{2} \\ \frac{\hbar\Omega_{\text{r}}}{2} & E_{\text{ex}}(\mathbf{k}) \end{pmatrix}, \tag{2.9}$$

where $E_{\text{ph}}(\mathbf{k}) = \hbar c' k$ ($E_{\text{ex}}(\mathbf{k}) = \hbar\omega_0 + \frac{\hbar^2 k^2}{2M}$) denotes the energy of the photon (exciton). The diagonalization of this Hamiltonian yields new eigenstates, which are called lower polariton (LP) and upper polariton (UP):

$$|LP\rangle = X_{\mathbf{k}}\,|X\rangle + C_{\mathbf{k}}\,|P\rangle\,, \tag{2.10}$$

$$|UP\rangle = -C_{\mathbf{k}}\,|X\rangle + X_{\mathbf{k}}\,|P\rangle\,, \tag{2.11}$$

where $|P\rangle$ ($|X\rangle$) is the photonic (excitonic) basis state of the noninteracting system. The new eigenstates are a linear combination of the photonic and excitonic states. The expansion coefficients $C_{\mathbf{k}}$ and $X_{\mathbf{k}}$ are the so-called Hopfield coefficients and the square of the mean value determines the photonic and excitonic fraction of the corresponding polariton, respectively. They satisfy the relation

$$|C_{\mathbf{k}}|^2 + |X_{\mathbf{k}}|^2 = 1. \tag{2.12}$$

$|C_{\mathbf{k}}|^2$ and $|X_{\mathbf{k}}|^2$ are given by the following relations

$$|C_{\mathbf{k}}|^2 = \frac{1}{2}\left(1 - \frac{\Delta E(\mathbf{k})}{\sqrt{\Delta E(\mathbf{k})^2 + (\hbar\Omega_{\mathrm{r}})^2}}\right), \tag{2.13}$$

$$|X_{\mathbf{k}}|^2 = \frac{1}{2}\left(1 + \frac{\Delta E(\mathbf{k})}{\sqrt{\Delta E(\mathbf{k})^2 + (\hbar\Omega_{\mathrm{r}})^2}}\right), \tag{2.14}$$

where $\Delta E(\mathbf{k}) = E_{\mathrm{ph}}(\mathbf{k}) - E_{\mathrm{ex}}(\mathbf{k})$ is the so-called exciton-photon detuning (in the following abbreviated as detuning). A large negative detuning corresponds to a Hopfield coefficient $|C_{\mathbf{k}}|^2 \approx 1$ and a mainly photon-like LP (exciton-like UP). For a large positive detuning the situation is reversed: $|X_{\mathbf{k}}|^2 \approx 1$ and the LP (UP) is mainly determined by the excitonic (photonic) properties. However, for the case of degeneracy of the unperturbed states, i.e. $E_{\mathrm{ph}}(k_0) = E_{\mathrm{ex}}(k_0)$ and therefore $\Delta E(k_0) = 0$, $|C_{k_0}|^2 = |X_{k_0}|^2 = \frac{1}{2}$, the LP and the UP exhibit both 50 % excitonic and photonic character (at $|k| = k_0$). The corresponding eigenenergies are

$$E_{\mathrm{LP,UP}} = \frac{1}{2}\left[E_{\mathrm{ph}}(\mathbf{k}) + E_{\mathrm{ex}}(\mathbf{k}) \mp \sqrt{(E_{\mathrm{ph}}(\mathbf{k}) - E_{\mathrm{ex}}(\mathbf{k}))^2 + (\hbar\Omega_{\mathrm{r}})^2}\right]. \tag{2.15}$$

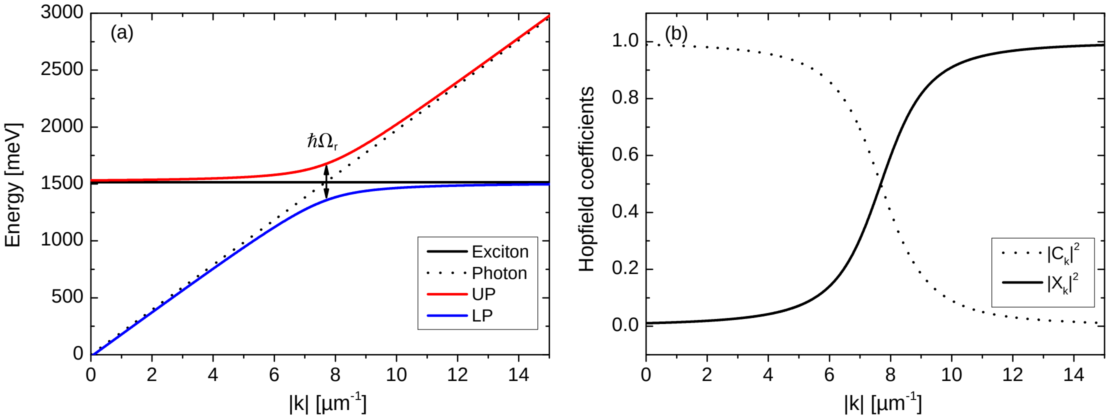

Figure 2-1: (a) Calculated polariton dispersions for the 1s heavy hole bulk exciton resonance in GaAs. For better visibility the Rabi splitting is enhanced by a factor of 20 and indicated by a black arrow. (b) Corresponding squared Hopfield coefficients.

The $\mp$-sign indicates an anticrossing behavior of the new eigenstates, which is characteristic for coupled quantum systems. The minimal energy level separation occurs for the degeneracy case $\Delta E(\mathbf{k_0}) = 0$ and corresponds to the Rabi splitting $\hbar\Omega_\mathrm{r}$.

Fig. 2-1 (a) shows a schematic polariton dispersion at the 1*s* bulk exciton resonance in GaAs (E_1s = 1515 mev), which is calculated by diagonalization of the Hamiltonian given in Eq. (2.9). For simplicity other exciton resonances are neglected. The Rabi splitting is increased by a factor 20 for better visibility. The following properties of bulk polaritons are evident from Fig. 2-1:

(i) For wavenumbers far away from the crossing point of the eigenstates of the noninteracting system, the LP and UP dispersions approach the dispersions of the exciton and photon, respectively, which is also reflected by squared Hopfield coefficients of unity and zero value.

(ii) At the point of degeneracy an anticrossing of the polariton branches can be observed, which is characteristic for light-matter interaction.

(iii) The polariton dispersion exhibits a monotonous behavior, i.e. there is no polaritonic state exhibiting a minimum in energy. In contrast, polaritons in microcavities possess a well-defined energetic minimum (see Sec. 2.3.2).

For the description of the interaction of the light field with n excitonic resonances, the Hamiltonian of Eq. (2.9) can be extended to a $(n+1)$x$(n+1)$-matrix, which is used to model a polariton dispersion in chapter 3.

2.2 Validity of the polariton model

As already mentioned in Sec. 2.1, the outlined polariton model is only valid under certain conditions, at which the build-up of new eigenstates can be observed. For the assessment of the prerequisites for the observation of polaritons it is necessary to include damping effects into the model outlined in the previous section. Damping effects are mediated e.g. by exciton-lattice interaction by phonons and by leakage of photons out of the semiconductor. A comprehensive quantum field theoretical treatment of polaritons including phonon interaction was given by Tait [42] and also the requirements for the observation of polariton effects were derived in this work. In this connection, two kinds of solutions for the polariton dispersion are discussed: Firstly, a quasiparticle solution where polaritons are introduced into the system with fixed momentum $\mathbf{k}$ at a time t and are not influenced further by an excitation source. In this case the semiconductor is uniformly excited. This situation typically occurs in a nonlinear optics experiment as described in chapter 3. In this case polariton effects occur as long as

$$\hbar\Gamma < \frac{\hbar\Omega_\mathrm{r}}{2}, \tag{2.16}$$

where $\hbar\Gamma$ describes the broadening of the linewidth induced by damping. This condition is fulfilled in most cases, e.g. for the 1*s* exciton in bulk GaAs a homogeneous broadening of the linewidth of $\hbar\Gamma = 0.2$ meV has been observed [43], whereas the Rabi splitting is about 16 meV [37]. This condition can also be interpreted in terms of Rabi-oscillations between the eigenstates of the undisturbed system: Polariton effects can be observed as long as there is coherent energy transfer between a photon and an exciton at least once.

Secondly, a forced harmonic solution which has a fixed frequency and damps out exponentially in space which is characteristic for linear optical experiments, e.g. transmission and absorption experiments. The following condition was derived in a quantum field theoretical approach [42] and also in the classical treatment of polaritons [44]:

$$\hbar\Gamma < \left(\frac{4\hbar\omega_0}{Mc^2}\right)^{\frac{1}{2}} \sqrt{\epsilon_\mathrm{b}}\hbar\Omega_\mathrm{r}. \tag{2.17}$$

Using typical parameters for bulk GaAs $M = 0.3m_\mathrm{e}$, $\sqrt{\epsilon_\mathrm{b}} = 3.55$ and $\hbar\omega_0 = 1515$ meV [45] the rhs of Eq. (2.17) yields a value of 0.35 meV, which is about the size of the broadening of the linewidth in high quality samples. Therefore, the observation of signatures of polariton effects is very challenging within the frame of linear optical experiments and requires very pure samples exhibiting narrow linewidths [45].

From the considerations outlined above, it is evident that the occurrence of polariton effects in bulk semiconductors depends very strongly on the experimental situation. The requirements for a linear optical experiment are much more stringent [Eq. (2.17)] compared to the situation of a nonlinear optical experiment [Eq. (2.16)]. Therefore, a large extent of different nonlinear optical spectroscopic techniques has been developed to investigate polariton effects in bulk semiconductors [46].

However, as will be discussed in the next section, semiconductor microcavities possess the huge advantage that only the condition of the quasiparticle solution [Eq. (2.16)] has to be fulfilled due to wavevector confinement independent of the experiment performed. Therefore, the observation of polariton effects is much easier to achieve than in bulk semiconductors.

2.3 Polaritons in semiconductor microcavities

Polaritons in bulk semiconductors are subject to several restrictions, which prevent a further evolution from fundamental research to applications. These are especially: (i) Observation of polariton effects imposes high requirements on sample quality and experimental approach as outlined in the previous section, (ii) the three physical parameters entering Eq. (2.7), i.e. the exciton-energy $\hbar\omega_0$, the Rabi splitting $\hbar\Omega_\mathrm{r}$ and the photon dispersion, cannot be designed at will and (iii) the LP in bulk material does not possess an energetic minimum.

However, the confinement of the wavevector of the light field in one direction using a microcavity can resolve all these issues as will be discussed within this section.

2.3.1 Semiconductor microcavities

The description of microcavities and the implications on the dispersion of the photon mainly follows Refs. [47–49], unless otherwise stated. A microcavity is an optical resonator with spatial extent in the range of the wavelength of light. Due to the very small resonator dimensions, the time for a round trip of a photon within the resonator is rather short, which imposes high requirements on the reflectivity of the microcavity mirrors to allow for a storage time of photons within the microcavity of several picoseconds. Metallic mirrors typically do not provide reflectivities larger than 99%, whereas dielectric mirrors can be designed as such, that in principle arbitrarily high reflectivities can be realized. Fig. 2-2 shows a typical design of a semiconductor microcavity surrounded by dielectric mirrors on both sides, so-called distributed Bragg reflectors (DBRs). The DBR consists of alternating layers of different materials with different index of refraction and optical thickness of $\lambda_{\mathrm{DBR}}/4$. Partial reflection of light occurs at each layer boundary and the reflected beams of light with an optical wavelength close to λ_{DBR} interfere constructively, i.e. the DBR acts as a high quality reflector within a certain spectral range around λ_{DBR}. Within this spectral range, light cannot propagate into the structure. In analogy to the energy bandgap of a semiconductor one speaks of a photonic bandgap or a photonic stopband, respectively. The reflectivity of a DBR is given by the relation

$$R = 1 - 4\frac{n_{\mathrm{ext}}}{n_{\mathrm{c}}}\left(\frac{n_1}{n_2}\right)^{2n}, \tag{2.18}$$

where n_1 (n_2) is the lower (higher) index of refraction of the DBR layers, n the number of alternating layer pairs, n_{c} the index of refraction of the cavity material and n_{ext} the index of refraction of the substrate or the vacuum depending on whether the upper or lower DBR is considered. Due to the different values of n_{ext} for the upper and lower DBR, respectively, it is convenient to extend the lower DBR by four more pairs of layers to obtain the same reflectivity for both DBRs. For the structure shown in Fig. 2-2, using the index of refractions $n_{\mathrm{AlAs}} = 3$ and $n_{\mathrm{Al_{0.2}Ga_{0.8}As}} = 3.5$, respectively, [50] one obtains a reflectivity as high as $R = 0.99993$.

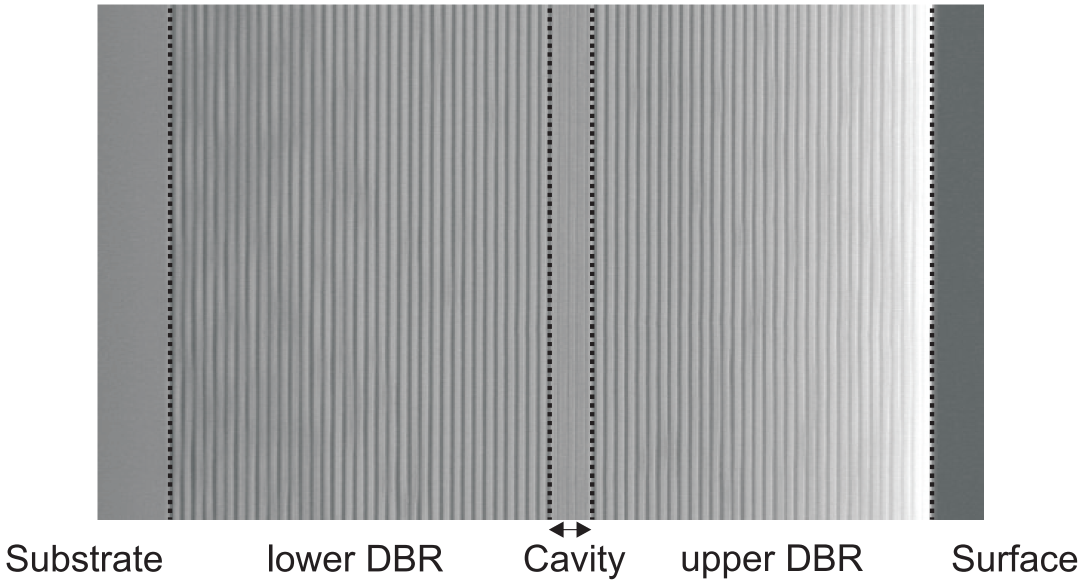

Figure 2-2: Scanning electron microscope (SEM) image of the cross section of a typical microcavity structure investigated in this thesis. The central cavity layer, consisting of AlAs, is surrounded on both sides by DBR structures consisting of 32 and 36, alternating pairs of AlAs and $\mathrm{Al_{0.2}Ga_{0.8}As}$ layers, respectively, which provide high reflectivities larger than 99%. SEM image has been provided by the institute of Technical Physics of Würzburg University.

The cavity layer is designed for a certain target wavelength λ_c and has an optical thickness of $\lambda_\mathrm{c}/2$ or a multiple of $\lambda_\mathrm{c}/2$. The cavities investigated in this thesis are all of $\lambda_\mathrm{c}/2$-type. The cavity layer, sandwiched between two DBRs, can be considered as a defect or impurity in an ideal photonic crystal, which allows for the propagation of a localized photonic mode within the photonic bandgap. The quality factor Q (Q-factor) of a microcavity is defined as

$$Q = \frac{\lambda_\mathrm{c}}{\delta\lambda_\mathrm{c}}, \tag{2.19}$$

where $\delta\lambda_\mathrm{c}$ is the linewidth of the cavity resonance. The Q-factor describes the rate of dissipation of optical energy and the characteristic lifetime τ of a photon within the cavity is given by

$$\tau = \frac{Q}{\omega_\mathrm{c}}. \tag{2.20}$$

For a $\lambda_\mathrm{c}/2$-cavity the free spectral range is the same as the cavity mode frequency, therefore the Q-factor and the finesse F are equivalent:

$$Q = F = \frac{\pi\sqrt{R}}{1-R}. \tag{2.21}$$

However, Eq. (2.21) holds only if one assumes that leakage of photons due to imperfect mirrors is the only source of energy dissipation. In realistic structures other dissipation processes (e.g., scattering and absorption) also play a role, therefore the Q-factor cannot be increased arbitrarily by adding more and more DBR layers. Consequently, F only gives an upper bound for the Q-factor.

An additional complication arises from the fact that the electromagnetic (EM) field of the cavity mode penetrates into the DBR structure due to the low reflection coefficient of the single $\lambda_\mathrm{DBR}/4$-layers of the DBR. The effective penetration depth is given by:

$$L_\mathrm{DBR} = \frac{\lambda_\mathrm{c}}{2n_\mathrm{c}} \frac{n_1 n_2}{|n_1 - n_2|}, \tag{2.22}$$

which yields an effective cavity length of $L_\mathrm{eff} = L_\mathrm{c} + L_\mathrm{DBR}$, where $L_\mathrm{c} = \frac{\lambda_\mathrm{c}}{2n_\mathrm{c}}$ is the length of a $\lambda_\mathrm{c}/2$-cavity. For the microcavity shown in Fig. 2-2 this gives an effective cavity length 20 times larger compared to the length of a $\lambda_\mathrm{c}/2$-cavity. Therefore the frequency of the cavity mode ω_m is mainly affected by the DBR structure according to [51]

$$\omega_\mathrm{m} = \frac{L_\mathrm{c}\omega_\mathrm{c} + L_\mathrm{DBR}\omega_\mathrm{DBR}}{L_\mathrm{eff}}, \tag{2.23}$$

at which ω_DBR denotes the center frequency of the DBR given by the optical thickness of the single layers of the DBR. Therefore the cavity-mode frequency is mainly determined by the DBR and the relation $\omega_\mathrm{m} = \omega_\mathrm{c}$ holds only for the idealized case that the DBR layers have exactly half the optical thickness of the cavity.

The dispersion of the EM-field inside the cavity is given by the relation

$$E_\mathrm{c} = \frac{\hbar c}{n_\mathrm{c}} k = \frac{\hbar c}{n_\mathrm{c}} \sqrt{k_\perp^2 + k_{||}^2} = \frac{\hbar c k_\perp}{n_\mathrm{c}} \sqrt{1 + (k_{||}/k_\perp)^2}, \tag{2.24}$$

where $k_{||}$ is the in-plane wavenumber and $k_\perp = n_\mathrm{c}(2\pi/\lambda_\mathrm{c})$ the wavenumber perpendicular to the DBR structure. A Taylor expansion for small in-plane wavenumbers $k_{||} << k_\perp$

leads to

$$E_{\mathrm{c}} \approx \frac{\hbar c k_{\perp}}{n_{\mathrm{c}}}\left(1+\frac{k_{||}^{2}}{2k_{\perp}^{2}}\right) = E_{\mathrm{c}}(k_{||}=0)+\frac{\hbar^{2}k_{||}^{2}}{2m_{\mathrm{c}}}, \tag{2.25}$$

where the cavity photon effective mass is

$$m_{\mathrm{c}} = \frac{E_{\mathrm{c}}(k_{||}=0)n_{\mathrm{c}}^{2}}{c^{2}}, \tag{2.26}$$

which is typically on the order of $10^{-5}m_{\mathrm{e}}$. Due to the confinement of the EM-field in the direction perpendicular to the DBR structure, a parabolic dispersion of the EM-field is obtained according to Eq. (2.25). This results in the dispersion of the LP also being parabolic and therefore in an energetic minimum, which will be derived within the next section.

2.3.2 Interaction of the confined cavity mode with confined excitonic states

To obtain a polaritonic system using a microcavity, an interaction between the confined EM-field of the microcavity and the excitonic states must be provided. A common approach to realize this coupling is depicted in Fig. 2-3. Several stacks of quantum wells are placed within the central antinodes of the EM-field. A quantum well is a narrow layer of a semiconductor material (GaAs in the samples investigated in this thesis), which is surrounded by two barriers of semiconductors with a wider bandgap (AlAs in the investigated samples). In consequence, the exciton motion is confined in the growth direction of the sample in analogy to the well-known particle in a box problem in quantum mechanics. There are two benefits arising from the coupling of quantum well excitons to the EM-field of the cavity:

Firstly, the exciton binding energy is significantly increased with respect to bulk excitons. For the idealized condition of an infinitely high barrier and a quantum well thickness $L_{\mathrm{qw}} \to 0$, the theoretical limit for the exciton binding energy is [52]

$$R^{*2\mathrm{D}} = 4R^{*3\mathrm{D}}. \tag{2.27}$$

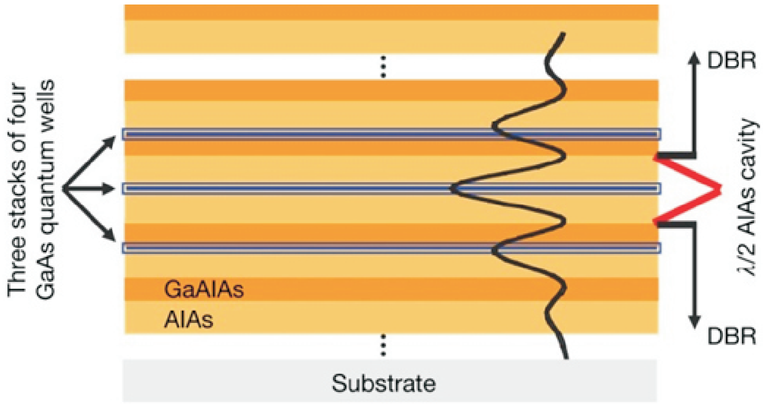

Figure 2-3: Schematic drawing of a typical GaAs-based microcavity design with three stacks of four GaAs quantum wells embedded within the three central antinodes of the EM-cavity field. The black solid line represents the field distribution of the cavity mode. Adapted from Ref. [55].

However, under realistic conditions of finite barrier height and quantum well thickness, typical exciton binding energies for GaAs quantum wells lie in a range of $2-3R^{*3\mathrm{D}}$, which corresponds to $R^{*2\mathrm{D}} = 8-12$ meV [52]. In consequence, due to the larger exciton binding energy, excitonic features in GaAs quantum wells are more robust concerning thermal dissociation compared to excitons in GaAs bulk material. Moreover, the oscillator strength of excitons in quantum wells is largely increased compared to bulk material [53]. Therefore, signatures of excitonic states in quantum wells can still be observed at room temperature, whereas no such feature can be seen in the case of bulk GaAs [54].

Secondly, the Rabi splitting can be designed at will by the choice of the number of quantum wells placed in the antinodes of the EM-field. The more quantum wells are embedded in the microcavity, the more excitons interact with the confined EM-field, and in consequence the oscillator strength of the excitons as well as the Rabi splitting is also increased. The Rabi splitting depends on the number of quantum wells N inserted into

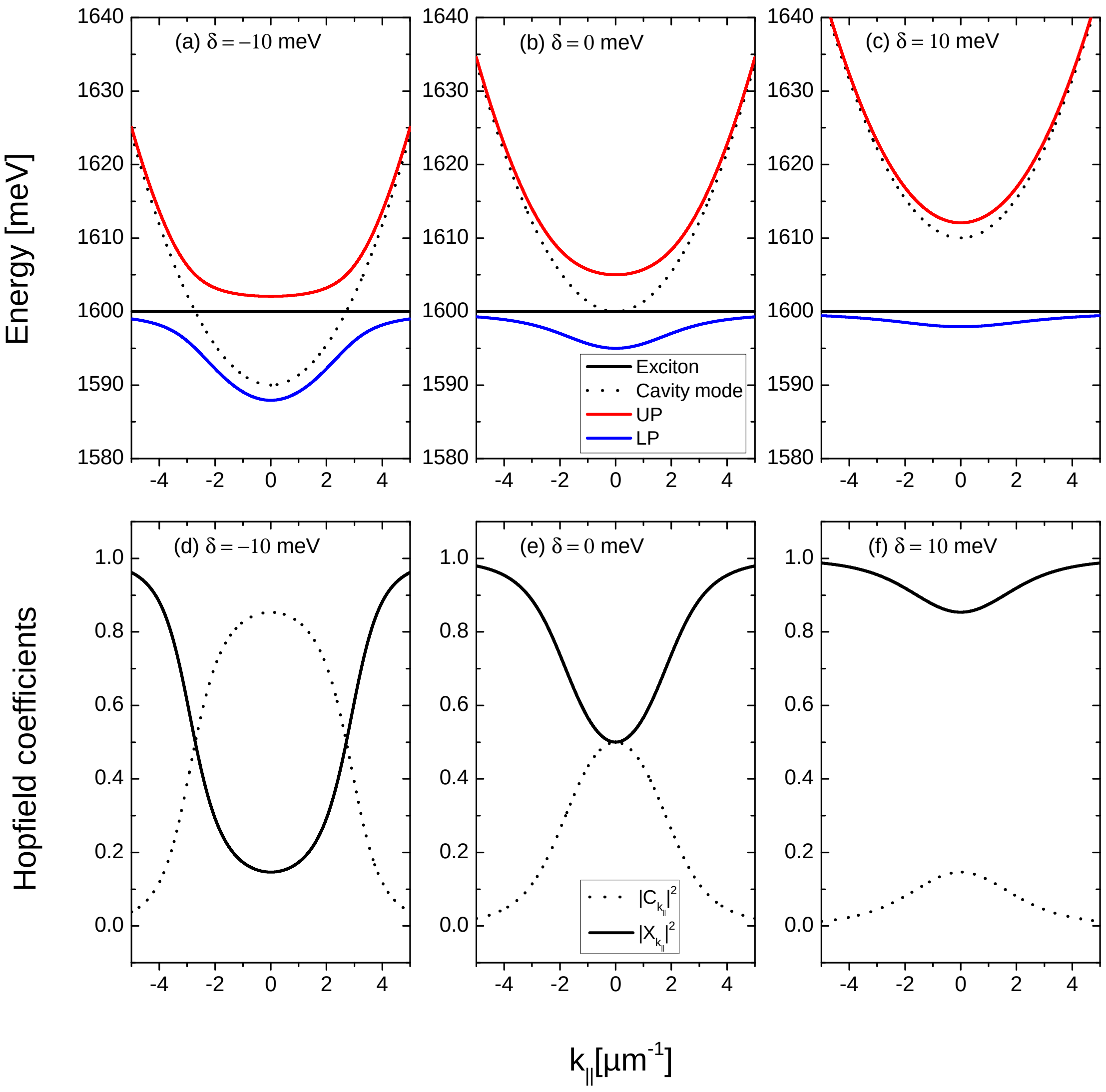

Figure 2-4: Calculated polariton dispersions for $\delta = -10$ meV (a), $\delta = 0$ meV (b) and $\delta = 10$ meV (c), respectively. The panels (d), (e) and (f) show the corresponding squared Hopfield coefficients $|C_{k_{||}}|^2$ and $|X_{k_{||}}|^2$.

the microcavity by the relation [56]

$$\Omega_{\mathrm{r}} \propto \sqrt{N}. \tag{2.28}$$

For the microcavity design depicted in Fig. 2-3, at which three stacks of four GaAs quantum wells are placed in the three central antinodes of the confined EM-field inside of the cavity, typically Rabi splittings on the order of 10 meV can be achieved.

The Eqs. (2.7)-(2.15) presented in Sec. 2.1 remain valid for polaritons in microcavities with the substitution $k \to k_{||}$ and the use of the parabolic photon dispersion derived in Eq. (2.25) due to the wavevector confinement perpendicular to the DBR. The diagonalization of the Hamiltonian given in Eq. (2.9) using the parabolic photon dispersion of Eq. (2.25) results in the polariton dispersions shown in Fig. 2-4. Here, an energy of $E_{\mathrm{ex}} = 1600$ meV for the $1s$ heavy hole exciton of the energetically lowest intersubband transition, which interacts with the cavity mode, is assumed and three different energies for the cavity mode of 1590 meV, 1600 meV and 1610 meV, respectively, at zero in-plane wavenumber are chosen. For the Rabi splitting $\hbar\Omega_{\mathrm{r}} = 10$ meV is selected. For convenience we define the detuning $\delta = E_{\mathrm{ph}}(k_{||} = 0) - E_{\mathrm{ex}}(k_{||} = 0)$ as the difference in energy between the cavity mode and the exciton at zero in-plane wavenumber. The calculated dispersions allow for the following statements:

(i) For large in-plane wavenumbers the LP (UP) approaches the exciton (photon) dispersion and the corresponding squared Hopfield coefficient reaches unity value independent of the chosen detuning.

(ii) For negative detuning, the LP is mainly determined by the photonic fraction for small in-plane wavenumbers, which is reflected by a steep parabolic dispersion and a large $|C_{\mathrm{k}_{||}}|^2$-coefficient. The UP, on the other hand, exhibits a rather flat dispersion and is therefore dominated by excitonic properties.

(iii) For positive detuning, the situation is reversed. The LP is rather exciton-like for small in-plane wavenumbers, whereas the UP is photon-like.

(iv) In the case of zero detuning, the photonic and excitonic fraction at $k_{||} = 0$ is 50% for the LP and UP, respectively, and the dispersions of both polariton branches exhibit the largest deviation from the dispersions of the undisturbed eigenstates.

(v) Finally, contrary to bulk polaritons the LP exhibits an energetic minimum for $k_{||} = 0$.

For small in-plane wavenumbers, the dispersion of both polariton branches can be approximated by a parabola [49]:

$$E_{\mathrm{LP,UP}}(k_{||}) = E_{\mathrm{LP,UP}}(0) + \frac{\hbar^2 k_{||}^2}{2m_{\mathrm{LP,UP}}}, \tag{2.29}$$

where the polariton effective mass is given by the harmonic mean of the effective masses of the photon and the exciton, weighted with the corresponding squared Hopfield coefficients:

$$\frac{1}{m_{\mathrm{LP}}} = \frac{|C_{\mathrm{k}_{||}=0}|^2}{m_{\mathrm{c}}} + \frac{|X_{\mathrm{k}_{||}=0}|^2}{m_{\mathrm{ex}}}, \tag{2.30}$$

$$\frac{1}{m_{\mathrm{UP}}} = \frac{|X_{\mathrm{k}_{||}=0}|^2}{m_{\mathrm{c}}} + \frac{|C_{\mathrm{k}_{||}=0}|^2}{m_{\mathrm{ex}}}. \tag{2.31}$$

Due to the much larger effective mass of the exciton compared to the EM-cavity mode, the effective mass of both polariton branches is mainly determined by the effective mass of the light field:

$$m_{\mathrm{LP}} \approx \frac{m_{\mathrm{c}}}{|C_{\mathrm{k}_{||}=0}|^2}, \tag{2.32}$$

$$m_{\mathrm{UP}} \approx \frac{m_{\mathrm{c}}}{|X_{\mathrm{k}_{||}=0}|^2}. \tag{2.33}$$

Consequently, depending on the detuning, the polaritons exhibit an effective mass on the order of $10^{-4} m_{\mathrm{e}}$. This extraordinarily small effective mass allows for the observation of condensation of polaritons similar to Bose-Einstein condensation (BEC) in condensed matter as will be discussed in Sec. 2.4.

So far it has been shown that two of the main restrictions of bulk polaritons can be resolved by the use of microcavities. Firstly, polariton dispersions can be tailored at will by selection of the cavity resonance, exciton resonance and the Rabi splitting, which are accessible by the design of the microcavity and the embedded quantum wells. Secondly, the LP branch exhibits a well defined energetic minimum. Finally, the question arises, which of the criteria necessary for the observation of bulk polaritons, as derived in Sec. 2.2, is of relevance for microcavity based structures. However, due to the vertical confinement of the polariton along the cavity axis, the less stringent quasiparticle solution [given by Eq. (2.16)] is relevant for microcavity polaritons independent of the experiment performed [37]. Commonly, broadening parameters γ_{ex} (γ_{c}), which represent the half-width at half maximum of the linewidth of the exciton (cavity resonance), are phenomenologically introduced by the substitutions $E_{\mathrm{ex}} \rightarrow E_{\mathrm{ex}} - i\gamma_{\mathrm{ex}}$ and $E_{\mathrm{c}} \rightarrow E_{\mathrm{c}} - i\gamma_{\mathrm{c}}$, respectively. For the case of $\delta = 0$, this leads to the modified eigenenergies:

$$E_{\mathrm{LP,UP}} = \frac{1}{2}\left[E_{\mathrm{c}}(k_{||}) + E_{\mathrm{ex}}(k_{||}) - i\gamma_{\mathrm{c}} - i\gamma_{\mathrm{ex}} \mp \sqrt{(\hbar\Omega_{\mathrm{r}})^2 - (\gamma_{\mathrm{c}} - \gamma_{\mathrm{ex}})^2}\right]. \tag{2.34}$$

Here, the polariton concept remains valid as long as the expression within the square root is positive, i.e.

$$\hbar\Omega_{\mathrm{r}} > |\gamma_{\mathrm{c}} - \gamma_{\mathrm{ex}}|. \tag{2.35}$$

For the investigated GaAs-based microcavities, exhibiting Q-factors larger than 1000, this relation holds as long as the carrier density is below the Mott-density (see Sec. 4.1.1). Therefore, the observation of polariton effects is largely facilitated compared to bulk semiconductors, as the polariton dispersion can be typically measured by means of photoluminescence experiments.

2.4 Condensation of polaritons

As a composite particle, consisting of a linear superposition of two bosons, i.e. a photon and an exciton, the polariton behaves as a bosonic particle, too. Due to their very low effective mass and the existence of a well defined energetic minimum, the LPs in a microcavity are especially appealing for the realization of a macroscopic occupation of the ground state similar to BEC. Within this section common theoretical concepts to describe BECs are explained, which will be followed by a short discussion on the question whether the nomenclature BEC is appropriate for polariton condensates.

2.4.1 Einsteins proposal: The ideal Bose gas

The fundamental difference between fermions and bosons relies on the fact that the Pauli exclusion principle does not apply to bosons. Consequently, bosons can accumulate in unlimited quantity in a degenerate state. On the basis of a work of Satyendra Nath Bose on the quantum statistics of light, Albert Einstein predicted the existence of a phase transition, at which the ground state of a bosonic system is populated in a macroscopic way, and derived an explicit expression for the critical temperature T_c of the phase transition. In the following a brief derivation of Einsteins argument is given [57]:
As a starting point, a system of N noninteracting bosons possessing a mass m is considered distributed in a volume V at a temperature T. The average number of bosons $\overline{n_p}$ occupying a specific single particle state E_p is given by the Bose-Einstein distribution function

$$\overline{n_p} = \frac{1}{exp\{\beta[E_p - \mu(T)]\} - 1}, \tag{2.36}$$

where $\beta = 1/k_\mathrm{b}T$ and $\mu(T)$ is the chemical potential, which depends on the temperature T. For the noninteracting bosons a parabolic dispersion is assumed:

$$E_p = \frac{p^2}{2m}. \tag{2.37}$$

According to Eq. (2.36), $E_0 \geq \mu(T)$ has to be fulfilled, otherwise the occupation number for states with $E_p < \mu(T)$ would become negative. The overall particle number N is connected with the Bose-Einstein distribution function by the relation

$$N = \overline{n_0} + \sum_{p,p\neq 0} \overline{n_p}, \tag{2.38}$$

where the occupation number of the ground state is treated separately. For large systems, i.e. $V \to \infty$, the sum in Eq. (2.38) can be replaced by an integral which leads to

$$N = \overline{n_0} + \frac{V}{(2\pi\hbar)^3} \int d^3p\ \overline{n_p}. \tag{2.39}$$

The integral can be evaluated analytically and one obtains

$$N = \overline{n_0} + \frac{V}{\lambda_T^3} g_{3/2}(z), \tag{2.40}$$

where $g_{3/2}(z)$ is a polylogarithm of the order 3/2, $z = exp(\beta\mu)$ and the thermal wavelength λ_T is given by

$$\lambda_T = \frac{2\pi\hbar}{\sqrt{2\pi m k_\mathrm{b} T}}. \tag{2.41}$$

As $g_{3/2}(z)$ is a monotonic function, the second expression in Eq. (2.40) reaches its maximum value for a value of $\mu = 0$ for the chemical potential. This means, there is a maximum number of particles at a given temperature T which can occupy excited states. Consequently, the excess particles are forced to accumulate the ground state in accordance with Eq. (2.40). The critical temperature, at which a significant population of the ground state sets in, is therefore given by the relation

$$N = \frac{V}{\lambda_T^3} g_{3/2}(1). \tag{2.42}$$

Solving the equation for T_c leads to an explicit expression for the critical temperature:

$$k_\mathrm{b} T_\mathrm{c} = \frac{2\pi\hbar^2}{m}\left(\frac{n}{\zeta(3/2)}\right)^{2/3}, \tag{2.43}$$

where $\zeta(3/2) = g_{3/2}(1) \approx 2.6124$ is the Riemann zeta function for the argument $x = 3/2$ and $n = N/V$ the particle density. From Eq. (2.43) it is immediately evident that a low mass of the bosonic particle is beneficial for reaching a high critical temperature. Whereas for atomic gases temperatures within a range of $0.2 - 2$ μK are required to observe a phase transition to a BEC [58, 59], the very low effective polariton mass in microcavities allows for the observation of condensation phenomena up to room temperature in wide bandgap [60, 61] and organic semiconductors [62, 63]. Despite the simplifying assumptions of an infinite system and noninteracting particles, Eq. (2.43) already provides a good estimate. For example, for the parameters of liquid ^{4}He, one obtains a critical phase transition temperature of 3.13 K, which is in reasonable agreement with the experimentally determined temperature of 2.18 K for a phase transition to a superfluid state [57].

2.4.2 Interacting Bose gas

For a more precise description of a bosonic many-particle system, interactions between bosons and the inclusion of additional single particle potentials V_ext have to be considered. A convenient starting point for the theoretical treatment of the system is the nonrelativistic many-body Hamiltonian in second quantization:

$$\begin{aligned} \hat{H} &= \int \left(\frac{\hbar^2}{2m}\nabla\hat{\Psi}^\dagger(\mathbf{r})\nabla\hat{\Psi}(\mathbf{r})\right) d\mathbf{r} + \int \left(V_\mathrm{ext}(\mathbf{r})\hat{\Psi}^\dagger(\mathbf{r})\hat{\Psi}(\mathbf{r})\right) d\mathbf{r} \\ &+ \frac{1}{2}\int \left(\hat{\Psi}^\dagger(\mathbf{r})\hat{\Psi}^\dagger(\mathbf{r}')V(\mathbf{r}-\mathbf{r}')\hat{\Psi}(\mathbf{r})\hat{\Psi}(\mathbf{r}')\right) d\mathbf{r}d\mathbf{r}'. \end{aligned} \tag{2.44}$$

Here, $\hat{\Psi}^\dagger(\mathbf{r})$ $[\hat{\Psi}(\mathbf{r})]$ denotes the field operator creating [annihilating] a particle at the point $\mathbf{r}$. The definition of the field operators is given by

$$\begin{aligned}\hat{\Psi}(\mathbf{r}) &= \sum_i \varphi_i(\mathbf{r}) a_i, && (2.45)\\ \hat{\Psi}^\dagger(\mathbf{r}) &= \sum_i \varphi_i^*(\mathbf{r}) a_i^\dagger, && (2.46)\end{aligned}$$

where $\varphi_i(\mathbf{r})$ is the single-particle wavefunction in the state i. The field operators obey the well-known commutation relations for bosons:

$$\begin{aligned}[\hat{\Psi}(\mathbf{r}), \hat{\Psi}^\dagger(\mathbf{r}')] &= \delta(\mathbf{r}-\mathbf{r}'), && (2.47)\\ [\hat{\Psi}(\mathbf{r}), \hat{\Psi}(\mathbf{r}')] &= 0. && (2.48)\end{aligned}$$

The equation of motion for the field operator $\hat{\Psi}(\mathbf{r})$ can be derived in the Heisenberg representation using Eq. (2.44) and the commutation relations for the field operator [64]:

$$\begin{aligned}i\hbar\frac{\partial}{\partial t}\hat{\Psi}(\mathbf{r},t) &= [\hat{\Psi}(\mathbf{r},t), \hat{H}] = && (2.49)\\ &= \left[-\frac{\hbar^2\nabla^2}{2m} + V_{\text{ext}}(\mathbf{r},t) + \int \hat{\Psi}^\dagger(\mathbf{r}',\mathbf{t}) V(\mathbf{r}-\mathbf{r}')\hat{\Psi}(\mathbf{r}',t) d\mathbf{r}'\right]\hat{\Psi}(\mathbf{r},t).\end{aligned}$$

2.4.3 The Gross-Pitaevskii equation

For the further treatment of Eq. (2.49), the following assumptions and approximations are made [65]:

(i) The temperature of the Bose gas is lower than the critical temperature for BEC. In consequence, the momenta of the bosons are small. Therefore the inequality

$$kR << 1, \tag{2.50}$$

is always satisfied, where R denotes the length scale at which the bosons interact with each other. The inequality (2.50) determines the low energy regime in standard scattering theory [66]. In this case the differential scattering cross section becomes independent of energy and scattering angle and is only determined by the so-called s-wave scattering length a.

(ii) A dilute Bose gas is considered, which warrants an interaction of more than two particles to be negligible. This assumption has already been used for the ansatz of Eq. (2.44), where only two-particle interactions are considered. The diluteness criterion can be formulated in terms of the following inequality

$$|a| << n^{-1/3}, \tag{2.51}$$

where n is the density of the Bose gas. This means that the average particle separation is much larger than the scattering length a.

(iii) The ground state is occupied with a large number of bosons $N_0 >> 1$, and the number of uncondensed bosons is much smaller than N_0. This allows for the replacement of the field operator $\hat{\Psi}(\mathbf{r},t)$ with a classical wavefunction $\Psi_0(\mathbf{r},t)$ with the normalization

$$\int |\Psi_0(\mathbf{r},t)|^2 d\mathbf{r} = N_0, \tag{2.52}$$

which is also called the order parameter for the phase transition to BEC.

(iv) $\Psi_0(\mathbf{r},t)$ varies slowly on the length scale R of boson interaction. This allows for the substitution $\Psi_0(\mathbf{r}',t) \rightarrow \Psi_0(\mathbf{r},t)$ in the integral of Eq. (2.49).

Under this assumptions one can write down the famous Gross-Pitaevskii equation (GPE) straight forward:

$$i\hbar\frac{\partial}{\partial t}\Psi_0(\mathbf{r},t) = \left[-\frac{\hbar^2\nabla^2}{2m} + V_{\text{ext}}(\mathbf{r},t) + g|\Psi_0(\mathbf{r},\mathbf{t})|^2\right]\Psi_0(\mathbf{r},t), \tag{2.53}$$

where $g = \int V(\mathbf{r})d^3\mathbf{r}$ is the interaction coupling constant, which is related to the s-wave scattering length a by the relation:

$$g = \frac{4\pi\hbar^2 a}{m}. \tag{2.54}$$

From Eq. (2.53) one can derive the same continuity equation as for the linear Schrödinger equation:

$$\frac{\partial n}{\partial t} + \nabla\mathbf{j} = 0, \tag{2.55}$$

where the density of the Bose gas n and the current density $\mathbf{j}$ are given by:

$$n(\mathbf{r},t) = |\Psi_0(\mathbf{r},t)|^2 \tag{2.56}$$

$$\mathbf{j}(\mathbf{r},t) = -\frac{i\hbar}{2m}(\Psi_0^*\nabla\Psi_0 - \Psi_0\nabla\Psi_0^*) = n\frac{\hbar}{m}\nabla S. \tag{2.57}$$

Here, S denotes the phase of the order parameter given by:

$$\Psi_0(\mathbf{r},t) = \sqrt{n(\mathbf{r},t)}e^{iS(\mathbf{r},t)}. \tag{2.58}$$

The velocity of the condensate flow can now be defined as

$$\mathbf{v}_s(\mathbf{r},t) = \frac{\mathbf{j}}{n} = \frac{\hbar}{m}\nabla S, \tag{2.59}$$

with the important consequence that $\mathbf{v}_s$ is irrotational in any region of space, where $n(\mathbf{r},t)$ is nonzero:

$$\nabla \text{ x } \mathbf{v}_s(\mathbf{r},t) = 0. \tag{2.60}$$

However, if one considers a closed contour C around a region, where the condensate is absent, i.e. $\Psi_0(\mathbf{r},t) = 0$, the circulation is given by the so-called Onsager-Feynman quantization condition due to the fact that the phase is defined only modulo 2π:

$$\oint_C \mathbf{v}_s d\mathbf{l} = \frac{\hbar}{m}\oint_C \nabla S d\mathbf{l} = \frac{2\pi\hbar}{m}\cdot l, \tag{2.61}$$

where l is an integer number. The occurrence of such phase shifts of multiples of 2π around the singularity of a BEC are called quantized vortices and the quantization number l is termed vortex charge. Quantized vortices are excitations of a superfluid and the experimental observation of such is regarded as strong evidence for superfluid behavior.

For the theoretical description of polariton condensates, generalized versions of the GPE, including losses, amplification and energy relaxation terms [67–69] have emerged as valuable tools for the explanation of several experimental observations such as propagation and repulsion of polariton condensates [69], pattern formation [70, 71] vortex dynamics [72] and long range spin transport [73]. In this thesis, a generalized GPE is used for the simulations of flows of polariton condensates steered by optically generated potentials (see Sec. 5.2).

2.4.4 Bogoliubov theory

The momentum representation of Eq. (2.44) also poses as point of origin for the Bogoliubov theory. In contrast to the considerations in the previous section, the influence of external potentials is neglected, i.e. $V_{\text{ext}} = 0$. By accounting only for quadratic terms in particle operators a_p and $a_p^\dagger$ with nonzero momentum $\mathbf{p} = \hbar\mathbf{k}$ and executing a linear operator transformation similar to the Hopfield-transformation mentioned in Sec. 2.1, which is known as Bogoliubov-transformation in this context, one can derive the so-called Bogoliubov dispersion [65]:

$$E(k) = \left[\frac{gn}{m}(\hbar k)^2 + \left(\frac{(\hbar k)^2}{2m}\right)^2\right]^{1/2}. \tag{2.62}$$

For small momenta $\hbar k << \sqrt{gnm}$ this dispersion takes a linear form

$$E(k) = c_s \hbar k, \tag{2.63}$$

where $c_s = \sqrt{gn/m}$ is the speed of sound for the elementary excitation of the BEC. In simple words, low energy excitation of a BEC can be considered as sound waves similar to acoustic phonons in condensed matter and are a consequence of the spontaneous breaking of a gauge symmetry caused by the phase transition to BEC. The occurrence of a Bogoliubov-like linear dispersion has already been observed for polariton condensates [74,75], which is considered as evidence that polariton condensates are closely related to BEC.

2.4.5 Condensation of a 2D Bose gas

Following the approach presented in Sec. 2.4.1, it becomes evident that in an infinite one- or two-dimensional system, a BEC cannot occur at finite temperature as the integral in Eq. (2.39) diverges for $\mu \to 0$. Consequently, Eq. (2.39) is always fulfilled without the need for a macroscopic ground state occupation. This statement also holds when interactions between bosons are considered according to the Mermin-Wagner-Hohenberg (MWH) theorem [76, 77]. Nevertheless, under realistic experimental conditions the assumption of an infinite system size is never fulfilled. To achieve condensation of ultracold atoms, for example, the atoms are typically stored in magneto-optical traps [58,59]. The inclusion of external confinement alters the expression for the critical temperature, which was calculated in detail for several different potentials in the three-dimensional case [78]. For the case of one- and two-dimensional systems, critical temperatures for the occurrence of a BEC have been calculated under the condition of a spatially varying potential exhibiting a power-law dependence [79]. Such spatially varying potentials are inherent in semiconductor microcavities mainly due to lattice mismatch between the different layers of the DBR structure, which are denoted as disorder effects [80]. Moreover, the spread of the condensate is affected by the sample size, the size of the pumped area and the lifetime of polaritons within the cavity, therefore the spatial extent of the condensate is in general limited. Consequently, the MWH theorem is commonly not considered as a principle obstacle for the realization of a localized BEC consisting of microcavity polaritons [24, 81].

Besides a phase transition to a localized BEC, the occurrence of a second phase transition, which is called Berezinskii-Kosterlitz-Thouless (BKT) transition, is predicted for a 2D Bose gas [82, 83]. Below a critical temperature T_{BKT}, the 2D Bose gas exhibits superfluid behavior, which vanishes for the case of $T > T_{\mathrm{BKT}}$. To elucidate the physical processes at a BKT transition, quantized vortices have to be considered (see Sec. 2.4.3). Below the critical temperature of T_{BKT}, vortices can only exist in a bound form of pairs of singly charged vortices exhibiting opposite circulation $\pm 2\pi$. For a closed contour larger than the vortex pair size, there is no distortion of the phase along this path, since the vortex pair does not possess a net circulation. For $T > T_{\mathrm{BKT}}$, the vortex pairs break up and form a disordered gas of phase defects [84]. In contrast to BEC, a BKT transition requires interaction between bosons and cannot occur in an ideal Bose gas. The critical temperature for a BKT transition is given by the relation

$$k_{\mathrm{b}} T_{\mathrm{BKT}} = n_{\mathrm{s}} \frac{\pi \hbar^2}{2m}, \tag{2.64}$$

where n_{s} denotes the density of the superfluid. Signatures of a BKT state are the sudden occurrence of free vortices above T_{BKT} and a power law decay of the first order spatial coherence below T_{BKT}, which has been observed for 2D trapped cold atoms [85]. However, due to the small system size investigated in typical experiments studying semiconductor microcavities, the occurrence of a localized BEC transition is expected before a BKT transition [81]. In addition, no unambiguous evidence of a BKT transition involving microcavity polaritons has been observed so far.

Moreover, there is still an ongoing debate if the terminology BEC is appropriate for the description of the condensation of microcavity polaritons [86, 87], as microcavity polaritons are bosonic particles out of equilibrium due to their short lifetime in contrast to BEC of ultracold atoms. Nevertheless, microcavity polaritons exhibit several features which are characteristic for a BEC, such as signatures of superfluidity, namely the occurrence of quantized [27], semiquantized vortices [28] and suppression of scattering from defects [30], a linear Bogoliubov dispersion [74, 75] or the existence of long range order spatial coherence [24, 88]. In addition, typical theoretical concepts used for the descriptions of BEC, such as GPE and Bogoliubov theory can be applied to microcavity polaritons.

To conclude, polariton condensates are conceptually different from BECs of ultracold atoms due to the lower dimensionality of the system and their out-of-equilibrium character. On the other hand, microcavity polaritons share many physical features with BEC of ultracold atoms, which encourages the terminology BEC for microcavity polaritons. However, within this thesis the terminology polariton condensate will be used.

Chapter 3

Coherent propagation of blue polaritons in Cu_2O

In this chapter a novel nonlinear spectroscopic approach using two single frequency lasers is presented. In this connection, the blue exciton series of bulk Cu_2O is investigated, which is difficult to access by linear spectroscopic techniques due to the large absorption coefficient of Cu_2O in this spectral range. The sum-frequency (SF) signal observed exhibits remarkable polaritonic features of the blue exciton. This chapter has been published in similar form in Ref. [89].

3.1 Introduction

Nonlinear spectroscopy of solids [90] is a mature field allowing insights into electronic properties not accessible by linear optical methods. Considering only two-photon processes there are additional degrees of freedom available, since polarization vectors $\vec{e_i}$ and wave vectors $\vec{k_i}$ (i = 1,2) of both photon beams can be set separately, allowing k-space spectroscopy [90, 91], which gives experimental access to the dispersion of polaritons in bulk material. Besides spectroscopic data, nonlinear observations linked to coherent propagation of the excitation can be investigated. The text book example are the so-called Maker fringes observed in second-harmonic generation [92–94]. Another example is the coherent propagation of polaritons, which is observed as a beat-like structure in time-resolved experiments [95].

So far, light generated by sum-frequency generation (SFG) could be extracted out of a non-linear material only for energies below or close to the band gap with high efficiency, otherwise strong absorption occurs. Further, the investigation of non-linear effects has required power levels in the kW to MW range, necessitating pulsed laser sources. By spectrally narrow excitation of two exciton-polariton resonances in Cu_2O, strong SF-signals far above the bandgap can be observed using continuous wave lasers in the mW to W power range (see Sec. 3.4).

The lowest excitons of the so-called yellow series in Cu_2O have been intensively studied because they are considered as candidates for BEC in a three dimensional system [96–99]. Excitation from the upmost valence band of Γ_7^+-symmetry to the lowest conduction band of Γ_6^+-symmetry leads to the formation of orthoexcitons (Γ_5^+-symmetry) and paraexcitons (Γ_2^+-symmetry), which are optically forbidden and split off by 12 meV to lower energy from the quadrupole allowed orthoexcitons.

Besides the yellow exciton series there are three other series, the states of which are named green, blue and violet excitons according to their spectral range of absorption. The green series arises due to excitation from a Γ_8^+-valence band (split off by 130 meV from the Γ_7^+-valence band of the yellow series) to the same Γ_6^+-conduction band. The blue and violet excitons stem from the same Γ_7^+- and Γ_8^+-valence bands, respectively, but from an odd parity conduction band of Γ_8^--symmetry. A schematic representation of the band structure of Cu_2O near the Γ-point is shown in the inset of Fig. 3-1. The S-excitons of these series are dipole allowed. In contrast to the yellow and green series there have not been many experiments reported on the blue and violet series. Reflectivity and transmission measurements of very thin films ($\propto$ 100 nm) were reported in the 1960s [100–102]. Later the optical properties were studied by spectroscopic ellipsometry [103]. Because of the large oscillator strength of the blue and violet excitons, one expects a pronounced polariton structure, which has not been investigated up to now.

In this chapter, a nonlinear spectroscopic approach to investigate 1s blue polaritons in natural Cu_2O crystals of several 10 µm thickness is presented. Making use of two narrow band CW-lasers (dye laser and infrared laser), blue polaritons are excited by SFG. A SF-signal is only seen if the dye laser is tuned to the resonance of the yellow 1s orthoexciton. It has been shown before that 1s yellow orthoexciton-polaritons propagate coherently through rather thick samples ($\propto$ 1 mm) [95] with group velocities as low as 40 km/s [104], whereas the off resonant polaritons in the infrared spectral range exhibit a group velocity of about 100.000 km/s. Thus, this experiment provides the unique opportunity to investigate the interaction of polaritons with a group velocity difference of three orders of magnitude. A possible consequence of this experimental situation is the observation of coherent propagation in a spectral range of high absorption: It is expected that because of the large damping of blue polaritons with energies 0.5 eV above the band gap (absorption length $\approx$ 100 nm) [100], the SF emission originates only from the last 100 nm of the crystal. Nevertheless, for the case of an antiparallel configuration of the two laser beams a pronounced beat-like structure is observed which can be understood if one assumes coherent propagation of blue polaritons through the rather thick crystal (about 600 times the absorption length).

3.2 Theory

Despite the fact that Cu_2O is a semiconductor with inversion symmetry (point group O_h), SFG can be observed, showing characteristic dependencies on crystal orientation and polarization. Here, a three-step process is considered: In a first step the 1s orthoexciton of the yellow series (Γ_5^+-symmetry) is excited by a quadrupole transition (even parity operator Γ_5^+), in a second step the Γ_5^+-orthoexciton is coupled to the 1s orthoexciton of the blue series (Γ_4^--symmetry) by a dipole transition (odd parity operator Γ_4^-). Finally, in a third step a photon is emitted by a dipole transition to the ground state.

Using the coupling coefficients of the Tables of Koster et al. [105] for the above three steps, one can derive detailed polarization selection rules for all crystal orientations. For the first step the amplitude QA for the quadrupole transition to the Γ_5^+-orthoexciton is

$\vec{e}_{dye}$	$\vec{e}_{ir}$	analyser	f_{tp}	f_{le}
$1\bar{1}0$	$1\bar{1}0$	$1\bar{1}0$	0	1/9
$1\bar{1}0$	$1\bar{1}0$	$11\bar{2}$	2/9	1/9
$1\bar{1}0$	$11\bar{2}$	$1\bar{1}0$	2/9	0
$1\bar{1}0$	$11\bar{2}$	$11\bar{2}$	0	0
$11\bar{2}$	$1\bar{1}0$	$1\bar{1}0$	2/9	0
$11\bar{2}$	$1\bar{1}0$	$11\bar{2}$	0	0
$11\bar{2}$	$11\bar{2}$	$1\bar{1}0$	0	1/9
$11\bar{2}$	$11\bar{2}$	$11\bar{2}$	2/9	1/9

Table 3-1: Relative oscillator strength for different polarizer and analyzer configurations and $\vec{k}_{dye} = [111]$. f_{tp} (f_{le}) denote the relative oscillator strength for TP (LE).

given by the symmetric vector product [106]

$$QA = \vec{e}_{dye} \otimes \vec{k}_{dye} \ , \tag{3.1}$$

where $\vec{e}_{dye}$ and $\vec{k}_{dye}$ refer to the polarization and k-vector of the dye laser, respectively. In the second step, coupling the Γ_5^+-orthoexciton to the blue Γ_4^--orthoexciton [the electron in the Γ_6^+-conduction band is lifted by the infrared laser into the Γ_8^--conduction band (Fig. 3-1 inset)] leads to the amplitude SFA of the Γ_4^--state:

$$SFA = [\vec{e}_{dye} \otimes \vec{k}_{dye}] \otimes \vec{e}_{ir} \ , \tag{3.2}$$

where $\vec{e}_{ir}$ refers to the polarization of the infrared laser. Finally one has to decompose this vector into its transverse and longitudinal components with respect to the wave vector $\vec{k}_{dye}$. Only the transverse components lead to SFG (transversal polaritons (TPs) in Fig. 3-1). As shown in Table 3-1, one can also excite longitudinal excitons (LEs, polarization parallel $\vec{k}_{dye} = [111]$). According to the selection rules derived [Eq. (3.2)], there is no SFG expected for $\vec{k}_{dye}$ = [100] and [110]. Therefore, crystals oriented for $\vec{k}_{dye} = [111]$ are studied here.

In order to elucidate the kinematics of the SFG processes, the polariton dispersion is modeled taking into account three resonances. The inclusion of the violet exciton resonance [0.13 eV above the blue exciton resonance (inset of Fig. 3-1)] is of great importance, since the upper polariton branch of the blue exciton resonance is strongly influenced (pushed down) by the violet polariton. For setting up the Hamiltonian, the rotating wave approximation of the original Hopfield-Hamiltonian is used [Eq. (2.9)], which is extended by inclusion of two additional resonances to a 4x4 matrix. Thereby, the photon dispersion $E_{ph}(k)$ is coupled to the three exciton resonances $E_y(k)$ (yellow 1s orthoexciton), $E_b(k)$ (blue 1s exciton) and $E_v(k)$ (violet 1s exciton).

$$H = \begin{pmatrix} E_{ph}(k) & \frac{\sqrt{f_y}E_{y,0}}{2} & \frac{\sqrt{f_b}E_{b,0}}{2} & \frac{\sqrt{f_v}E_{v,0}}{2} \\ \frac{\sqrt{f_y}E_{y,0}}{2} & E_y(k) & 0 & 0 \\ \frac{\sqrt{f_b}E_{b,0}}{2} & 0 & E_b(k) & 0 \\ \frac{\sqrt{f_v}E_{v,0}}{2} & 0 & 0 & E_v(k) \end{pmatrix} . \tag{3.3}$$

For the yellow $1s$ orthoexciton $f_y = 1.3 \cdot 10^{-9}$ and $E_{y,0} = 2.032775$ eV are taken from Ref. [107] (note that for $k = [111]$ the oscillator strength is reduced by a factor 3 as compared to $k = [001]$). $f_b = 1.2 \cdot 10^{-2}$, $f_v = 2.1 \cdot 10^{-2}$, $E_{b,0} = 2.576$ eV and $E_{v,0} = 2.703$ eV denote the oscillator strengths and resonance energies of the blue and the violet excitons taken from Ref. [100]. Spatial dispersion is taken into account, using the same mass $m = 3m_e$ for all three exciton resonances (m_e corresponds to the free electron mass) [108]. $E_y(k) = E_{y,0} + \frac{\hbar^2 k^2}{2m}$, $E_b(k) = E_{b,0} + \frac{\hbar^2 k^2}{2m}$ and $E_v(k) = E_{v,0} + \frac{\hbar^2 k^2}{2m}$. $\sqrt{f_y} E_{y,0}$, $\sqrt{f_b} E_{b,0}$ and $\sqrt{f_v} E_{v,0}$ denote the corresponding Rabi energies. The photon dispersion is given by $E_{ph}(k) = \hbar c k / n_b$, where $n_b = 3$ is assumed for the background refractive index in the visible spectral range.

In Fig. 3-1 the polariton diagram for the three oscillator model is shown, which is derived from the diagonalization of the Hamiltonian given by Eq. (3.3). The kinematics of the experimental setup lead to resonances on the middle polariton branch. As outlined above, the $1s$ orthoexciton polariton is pumped by the dye laser. Depending on the direction of the infrared laser (parallel or antiparallel to the dye laser), two different resonances on the middle polariton branch are excited, which lead to two different SF-signals.

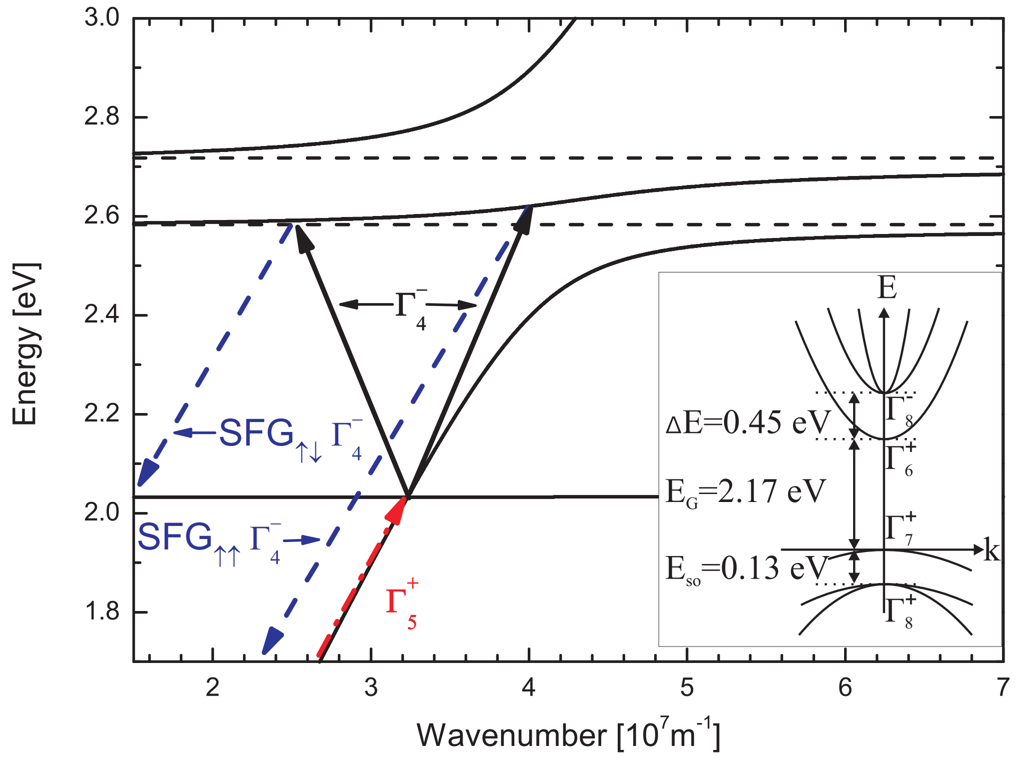

Figure 3-1: Polariton diagram of a three-oscillator model. Three-step process of the experimental approach is indicated by arrows. Black solid line, TP dispersion according to Eq. (3.3); dashed horizontal lines, resonances of blue and violet LEs; red dash-dotted arrow, quadrupole excitation (Γ_5^+-symmetry) of $1s$ yellow orthoexciton; black arrows, dipole transition (Γ_4^--symmetry) to the middle polariton branch from $1s$ yellow orthoexciton for parallel/antiparallel beam propagation; blue dashed arrows, SFG (Γ_4^--symmetry) for parallel/antiparallel beam propagation. Inset: Schematic band structure of Cu_2O close to the Γ-Point.

3.3 Experimental details

The high-resolution setup is shown schematically in Fig. 3-2. In the first step of SFG a single-frequency dye laser is used with line width < 5 neV and power < 100 mW (Coherent 899-29) for resonant excitation of the yellow 1*s* orthoexciton-polariton. For the excitation of the blue exciton-polariton in the second step a single-frequency optical-parametric-oscillator (OPO, Aculight Argos 2400 CW OPO, line width < 5 neV, power < 1 W) is used. The OPO covers an energy range of $0.496 - 0.568$ eV and $0.602 - 0.683$ eV for idler and signal output, respectively. Due to the degeneracy point of the OPO at 0.583 eV there is a gap in the tuning range between $0.568 - 0.602$ eV. The polarization and the power level of the dye laser and the OPO can be set by half-wave plates and Glan-Taylor prisms. The dye laser beam is focused by a lens of 200 mm focal length onto the sample via a silicon beam splitter (transparent for the IR beam from the OPO). For focusing the infrared beam a BaF_2 lens is used. With a flip mirror and an additional beam splitter one can switch between a parallel and an antiparallel beam configuration. For the adjustment of the overlap of the laser beams, a 100 μm pinhole is mounted on the sample holder. Measurements are performed at 1.5 K using a He-bath cryostat.

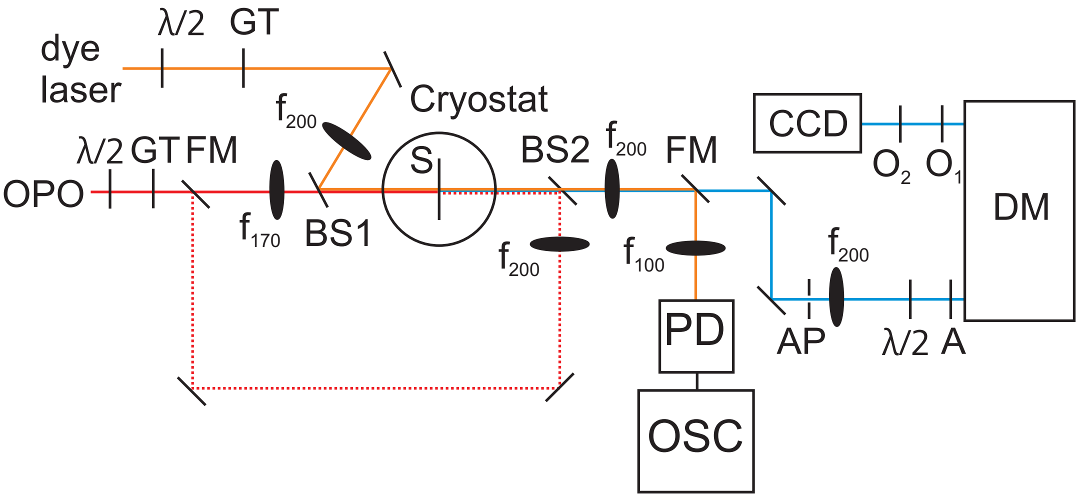

Figure 3-2: Schematic setup for SFG spectroscopy: A, analyzer; AP, aperture; BS1, silicon beam splitter; BS2, beam splitter; CCD, charge coupled device camera; DM, double monochromator; f_{xx}, lens with xx mm focal length; FM, flip mirror; GT, Glan-Taylor prism; $\lambda/2$, half-wave plate; O_1 and O_2, photo objectives; OPO, optical-parametric-oscillator; OSC, oscilloscope; PD, photo diode; S, sample.

The SF-signal in the blue spectral region is measured with a nitrogen-cooled CCD-camera behind a double monochromator (second order). The polarization anisotropy of the monochromator was taken into account by setting the analyzer to the preferred polarization of the monochromator. The polarization of the SF-signal is then measured by tuning the half-wave plate. Two high quality photo objectives provide a magnification by a factor of 4 on the CCD. The observed line width of the SF is limited to 10 μeV by the resolution of the monochromator.

A galvanometer mounted tilting Brewster plate inside of the dye laser cavity enables one to perform a continuous wavelength scanning in a spectral range of up to 30 GHz, which allows for a precise determination of the 1*s* orthoexciton resonance by means of transmission measurements. The transmitted laser beam is detected by a photodiode. The signal of the photodiode is read out by a digital oscilloscope triggered by the driving voltage of the Brewster plate.

As discussed in detail in Ref. [106], strain-free mounting of the sample is very important. Nevertheless, it was still necessary to select an appropriate spot on the sample in order to achieve a narrow resonance of about 2.5 µeV as seen in Fig. 3-3. The samples (thickness 30 µm and 60 µm) are cut from a high quality natural crystal and oriented along [111] (because of selection rules, as derived in Sec. 3.2).

3.4 Results and discussion

In this section, firstly evidence for the occurrence of resonant SFG as outlined in Sec. 3.2 is provided. In this connection, a power and a polarization dependence is presented, which confirms the selection rules (Table 3-1). Finally, the SF-spectra for the parallel and antiparallel beam configuration are shown. The most striking result is the occurrence of a pronounced beat-like structure in the spectra of the antiparallel configuration which gives evidence for a coherent propagation of blue polaritons. Here, the propagation length in the SFG experiments is at least a factor 600 larger than the absorption length of about 100 nm, as known from one-photon experiments [100].

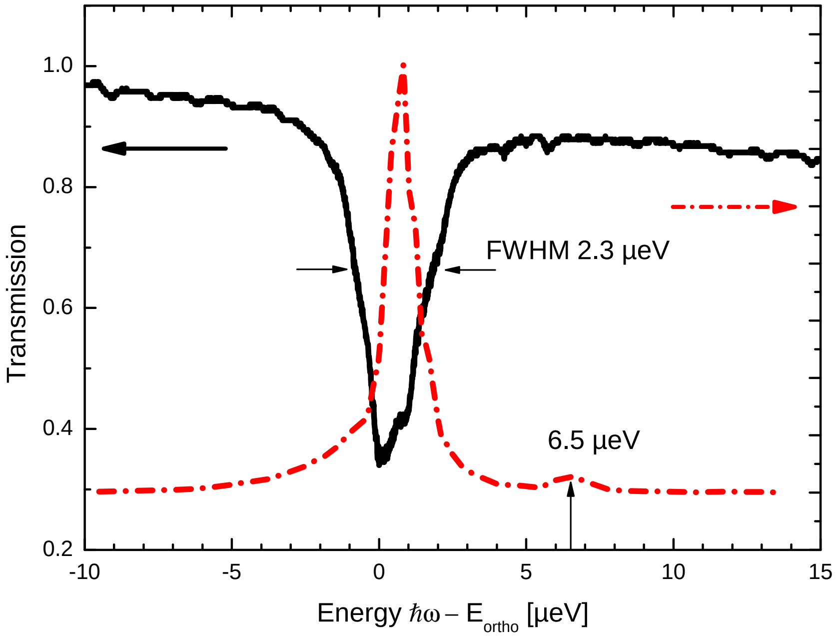

Figure 3-3: Black line, absorption spectrum of yellow 1*s* orthoexciton; red dash-dotted line, excitation spectrum of the SF-signal as function of dye laser-energy for fixed setting of the OPO. Maximum of absorption is at $E_{ortho} = 2.032788$ eV.

The dependence of the blue SF-signal on the energy of the dye laser is shown in Fig. 3-3. The narrow excitation spectrum clearly proves that a narrow band laser is a prerequisite for observing SFG in this study. The additional small resonance at about 6.5 µeV can be explained by a fine structure arising due to wave-vector-dependent exchange interaction as reported in Ref. [106]. For all other experiments performed, the

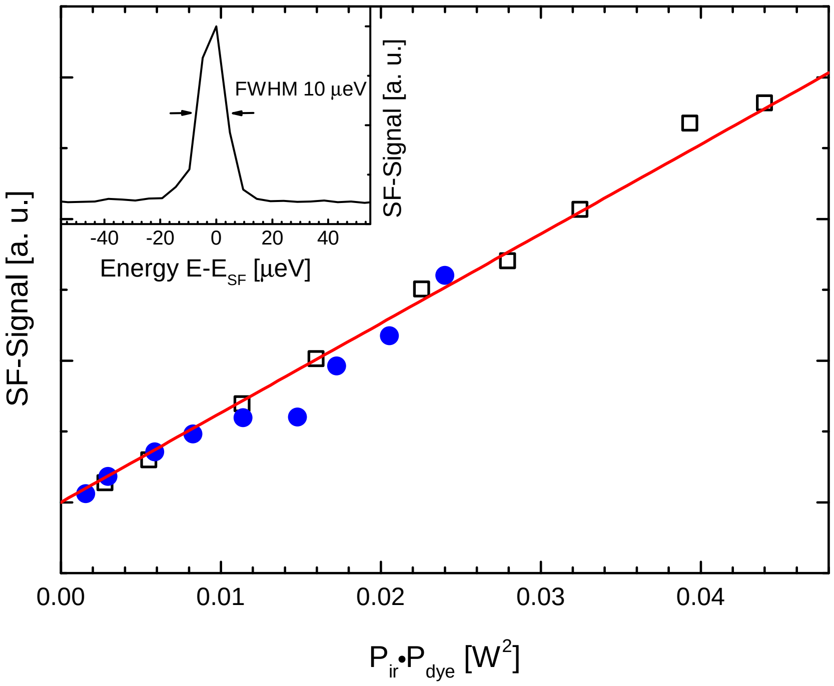

Figure 3-4: Dependence of the SF-signal on product of dye laser (P_{dye}) and OPO power (P_{ir}). Blue full circles, $P_{dye} = 30$ mW; black open squares, $P_{dye} = 55$ mW; red line, linear fit. Inset: Typical SF-spectrum.

dye laser energy has been kept constant at the transmission minimum of the yellow 1s orthoexciton.

In Fig. 3-4 the power dependence of the SF-signal is presented. As expected, the SF-signal depends linearly on the product of the power levels of both lasers. By placing an iris in the telescopic setup, it was confirmed that the SF-beam is collinear to the pump beams, as opposed to an isotropic signal distribution of incoherent photoluminescence. The inset of Fig. 3-4 shows a typical SF-signal. The full width at half maximum is about 10 µeV, which is limited by the spectral resolution of the monochromator.

In the inset of Fig. 3-5 a detailed polarization dependence of the SF-signal is shown for the incoming polarizations $\vec{e}_{dye} = [11\bar{2}]$ and $\vec{e}_{ir} = [1\bar{1}0]$. In accordance with the group theoretical considerations (Table 3-1), the SF-signal vanishes in $[11\bar{2}]$ and exhibits a maximum for $[1\bar{1}0]$. The other polarization dependences according to Table 3-1 are also confirmed. In addition, measurements of crystals oriented along $\vec{k}_{dye} = [100]$ and [110] have been performed. As expected from Eq. (3.2), no SFG has been observed.

In Fig. 3-5 (a)-(c) the SF-spectra for the parallel and antiparallel beam configuration are presented, respectively. In the parallel beam configuration [Fig 3-5 (a)] one can find a resonance centered at about 2.595 eV with a full width at half maximum (FWHM) of 10 meV, which is attributed to phase-matching (energy and momentum conservation) on the middle polariton branch as shown in Fig. 3-1.

In the antiparallel configuration [Fig. 3-5 (b) and (c)], however, oscillations of the SF-signal are clearly seen. At first sight, the most obvious interpretation of these oscillations seems to be the occurrence of a standing wave of the OPO beam in the sample. From the large absorption coefficient in the blue spectral range one expects that the emission of SF stems only from the last 100 nm of the crystal. In the case of a node at the sample boundaries one would expect a decrease of the SF-signal. However, using the Fresnel formula one can deduce a reflection coefficient of $R = \frac{(n_{ir}-1)^2}{(n_{ir}+1)^2} \approx 20\%$, where $n_{ir} = 2.55$ is the refractive index in the infrared spectral range as reported in Ref. [109]. This corresponds to a coefficient of the finesse of $F = \frac{4R}{(1-R)^2} \approx 1.25$ and a minimal transmission at the nodes of $T_{min} = \frac{1}{1+F} \approx 0.44$. Since it is shown in Fig. 3-4 that the intensity of the SF-signal scales linearly with the OPO laser power one would expect only a suppression by a factor of 2 and not by a factor of up to 50 as shown in the data [Fig. 3-5 (b) and (c)]. Besides, standing waves should also be observable in the parallel beam configuration.

An alternative explanation for the occurrence of these oscillations is a phase-matching effect. As discussed in Ref. [93], these so-called Maker fringes should be quenched if the nonlinear medium is absorbing. Here, the absorption length is even almost three orders of magnitude smaller than the thickness of the crystal [100–102]. Thus, the occurrence of oscillations which are related to a phase matching effect can only be explained if one assumes a coherent propagation of the blue polaritons through the crystal.

The condition for phase matching $\Delta k = 0$ is fulfilled on the middle polariton branch, where the polariton slopes of the OPO-beam starting from the $1s$ yellow orthoexciton-polariton resonance (Fig. 3-1) intersect. The SF-signal I_{SF} for a transparent medium is given by [93]:

$$I_{SF} \propto \frac{[\sin(\Delta k L/2)]^2}{(\Delta k L/2)^2} \ , \tag{3.4}$$

where L denotes the length of the crystal.

For the parallel (antiparallel) beam configuration the phase mismatch Δk is given by:

$$\Delta k = 2\pi \cdot \left[\frac{n_{sf_{\uparrow\uparrow(\uparrow\downarrow)}}}{\lambda_{sf}} - \frac{n_{ortho}}{\lambda_{ortho}} {}_{(}\mp{}_{)} \frac{n_{ir}}{\lambda_{ir}} \right] \ , \tag{3.5}$$

where $n_{sf_{\uparrow\uparrow(\uparrow\downarrow)}}$ is the refractive index for the SF-polariton in the parallel (antiparallel) configuration, n_{ortho} denotes the refractive index for the yellow $1s$ orthoexciton and n_{ir} for the infrared spectral range. λ_{sf}, λ_{ortho} and λ_{ir} are the corresponding wavelengths in vacuum.

A more rigorous analysis of the phase-matching spectrum would require the inclusion of damping processes in the polariton model. This might also explain that for the overall fit of the phase-matching analysis a rather high refractive index for the resonantly excited $1s$ orthoexciton-polariton ($n_{ortho} = 3.6$) was derived as compared to the previously reported background refractive index $n_{ortho} = 2.95$ [110]. With $n_{ir} = 2.55$ in the infrared spectral range and phase-matching $\Delta k = 0$ at an energy of 2.6062 eV one can fit the experimental data well for the antiparallel beam configuration for the 30 µm and the 60 µm thick sample [Fig. 3-5 (b) and (c)]. Unfortunately the spectral range between $2.600 - 2.630$ eV is not accessible to the OPO-system used due to the aforementioned gap in the tuning range. Therefore the phase matching condition could not be studied directly. The fact that no oscillations for the parallel configuration are observed, can be deduced from Eqs. (3.4) and (3.5). The corresponding phase matching spectrum is oscillating with a large period of about 50 meV, the resonance is thus not influenced by the phase matching effect.

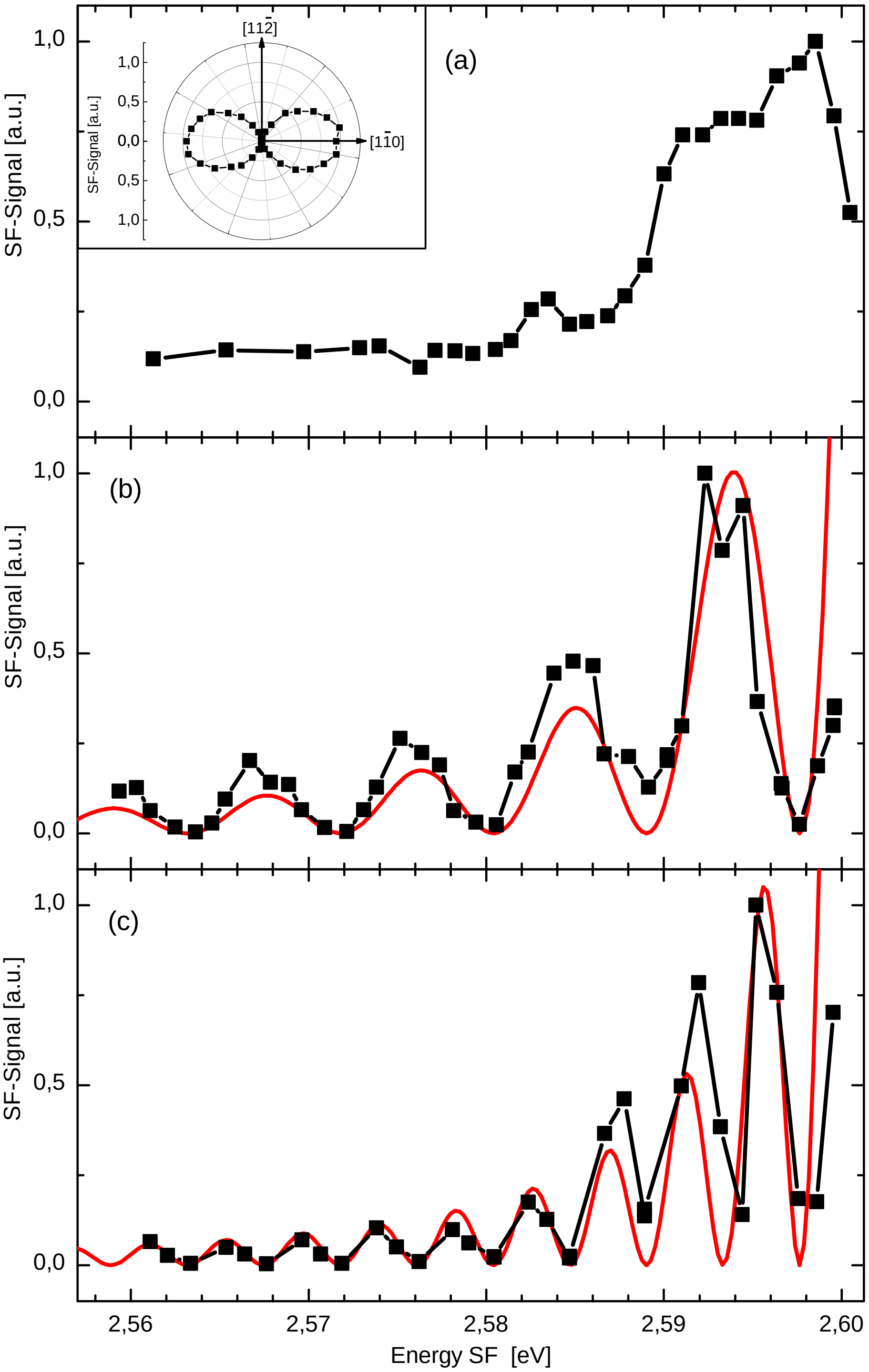

Figure 3-5: (a) Blue exciton-polariton resonance in the parallel beam configuration for the 30 µm sample. (b) and (c): Blue exciton-polariton resonance in the antiparallel beam configuration for the 30 µm and the 60 µm sample. Black squares, data; red line, calculated curve according to Eqs. (3.4) and (3.5). Power of the OPO and the dye laser as well as the dye laser energy has been kept constant. Inset: Polarization dependence of SF-signal with respect to the crystal axis [11$\bar{2}$] and [1$\bar{1}$0] ($\vec{k}_{dye}$ = [111]). Incoming polarizations are $\vec{e}_{dye}$ = [11$\bar{2}$] and $\vec{e}_{ir}$ = [1$\bar{1}$0]. Signal intensity is proportional to the radial distance from the center.

If there was an appreciable absorption of the coherently excited blue excitons due to relaxation processes to lower excitons (e.g. dipole-allowed P-excitons of the yellow series), one would expect an emission shifted to lower energy from the observed SF-emission. The spectral region down to the yellow series has been carefully scanned without observing any emission.

3.5 Summary

In conclusion, an efficient SFG in Cu_2O, a crystal with inversion symmetry, has been demonstrated using two continuous wave lasers of rather low power ($<$ 100 mW, $<$ 1 W). The selection rules for a quadrupole-dipole SFG process have been confirmed in detail. The most surprising observation is the occurrence of pronounced oscillations, which are observed only in the antiparallel beam configuration. A careful analysis of these oscillations reveals evidence for a coherent propagation of blue polaritons in crystals up to 600 times thicker than the absorption length, which is known from transmission measurements [100–102]. The reason for this unexpected observation might be the rather unique situation of the experimental approach: Firstly, two single frequency laser systems are used. Consequently, polaritons with very well defined energies and wavevectors are generated. Therefore, intercarrier scattering is expected to be significantly reduced due to a lack of available scattering channels which fulfill energy and momentum conservation according to Fermi's Golden Rule. Secondly, two coherently propagating polariton beams with a difference in group velocity by three orders of magnitude fuse to generate a SFG polariton beam.

Possible alternative interpretations of these results in terms of simple interference effects have been considered, which also lead to an oscillating pattern depending on the thickness of the crystal. This pattern would be expected for both configurations contrary to the experimental data. The missing beat-like pattern in the parallel configuration, however, is explained by an analysis assuming Maker-fringes. In addition, the large ratio of contrast (up to a factor of 50) as compared to a factor of 2 expected in an interference pattern, is a good argument for this interpretation.

Unfortunately, for experimental reasons, the resonance of the Maker fringes cannot be observed directly. As mentioned before, a weakness in the polariton analysis lies in the fact that damping is neglected. As a concept for a theoretical treatment of SFG it might be advantageous to start with polariton eigenstates as basis states and interpret SFG as a fusion of two incoming polaritons into an outgoing polariton as was first proposed in Ref. [111]. Due to the large difference in group velocity of the participating polariton beams in these experiments (see Sec. 3.1), the polariton fusion concept might be of even more relevance than in experiments discussed so far [112–114].

For future experiments it might be promising to look for an *interband* dynamic Stark effect using an infrared laser of higher power. An *intraband* dynamic Stark effect of yellow excitons has already been reported in Ref. [115].

Chapter 4

Feasibility study for polariton based lasing devices

In this chapter the physical constraints of two different lasing devices based on microcavity polaritons are investigated. Firstly, optimal operating parameters for a GaAs-based polariton laser emitting in the visible spectral range are studied by means of non-resonant optical pumping. In the second part of this chapter, a theoretical proposal for the emission of terahertz (THz) radiation making use of the transition between the $2p$ exciton state and the LP [31] is evaluated using nonlinear spectroscopic techniques. The first part of this chapter has been published in similar form in Ref. [116], the second part of this chapter has been published in a shorter version in Ref. [117].

4.1 Determination of operating parameters for a GaAs-based polariton laser

4.1.1 Introduction

Since the observation of the so-called strong coupling regime in semiconductor microcavities [17], the field of semiconductor based cavity quantum electrodynamics has been intensively studied due to many promising applications such as an inversionless polariton laser [21].

However, the term "polariton laser" is strictly speaking misleading, as the acronym laser is an abbreviation for "**L**ight **A**mplification by **S**timulated **E**mission of **R**adiation", whereas the operating principle of a polariton laser does not rely on the stimulated emission of photons. Nevertheless the term "polariton laser" is conveniently used in the literature, as a polariton laser shares the most characteristic property with a conventional laser, which is the emission of coherent monochromatic radiation. Fig. 4-1 schematically shows the operating principle of a conventional semiconductor laser [Fig. 4-1(a)] and a polariton laser [Fig. 4-1(b)], respectively, to elucidate the fundamental differences of these two devices. For convenience, non-resonant optical pumping is assumed here, as this pumping mechanism is solely applied for the experiments presented in this thesis.

Under this condition, the physical processes occurring in a conventional semiconductor laser can be described as follows: Firstly, an electron-hole (e-h) plasma is created

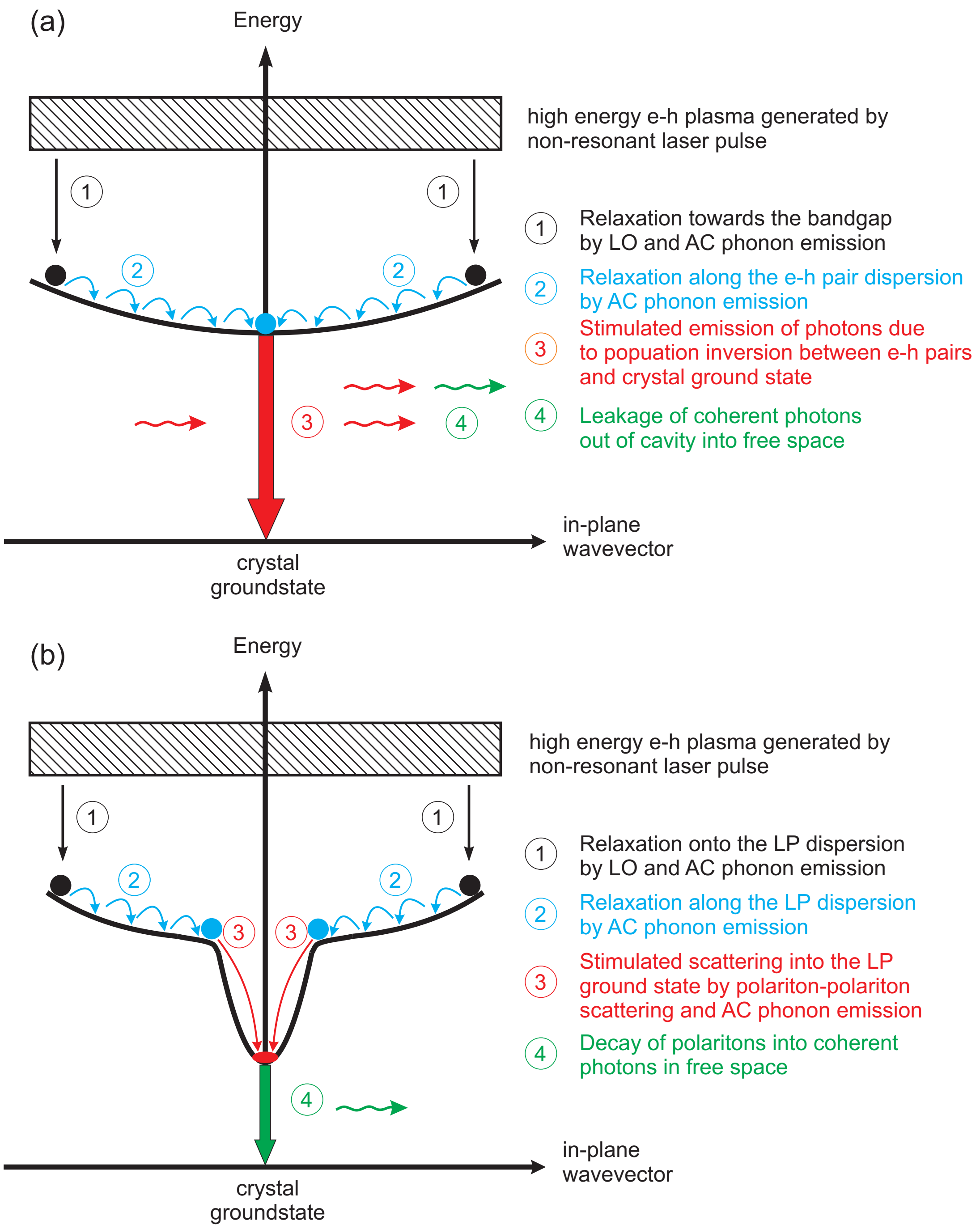

Figure 4-1: Principle of operation for a conventional semiconductor laser (a) and a polariton laser (b). The images are adapted from Refs. [49,118].

by non-resonant pumping, which loses energy by emission of longitudinal optical (LO) and acoustical (AC) phonons and occupies e-h pair states near the bandgap [Step 1 and 2 in Fig. 4-1(a)]. The e-h pair states are annihilated by a stimulated emission process mediated by a cavity photon, which amplifies the coherent EM field inside of the cavity (Step 3). Finally, EM field modes can escape from the cavity due to the finite reflectivity of the cavity mirrors (Step 4). Note, however, that a population inversion between the crystal ground state and the e-h pair states at the bandgap is required here, which is also known as Bernard-Duraffourg condition in this context [119], otherwise reabsorption of cavity photons suppresses the amplification of the EM field.

This is in contrast to the principle of operation of a polariton laser: An e-h plasma is created by non-resonant pumping, which loses energy by emission of longitudinal optical (LO) and acoustical (AC) phonons and finally forms excitons, which accumulate on the excitonic part of the LP dispersion at large in-plane wavevectors [Step 1 in Fig. 4-1(b)]. This is followed by a further relaxation process along the LP dispersion towards the so-called bottleneck region at the inflection point of the LP dispersion by emission of AC phonons (Step 2). The bottleneck area separates two regions of the LP dispersion: States with larger in-plane wavevector posses a negligible photonic component and can therefore be considered as pure excitons, whereas states with lower in-plane wavevectors exhibit a significant photonic Hopfield coefficient, which causes an increasing steepness of the LP dispersion, a decrease of the polariton lifetime and the density of states at low in-plane wavevectors. All these effects restrain a further effective relaxation down to the LP ground state mediated by AC phonons which is the reason for the nomenclature bottleneck region [49, 120]. For the further relaxation down to the LP ground state, especially under high power excitation conditions, polariton-polariton scattering becomes the dominant relaxation mechanism (Step 3) [121]. One polariton is scattered thereby to the LP ground state and a second one is scattered to a higher energy part of the LP dispersion under energy and wavevector conservation [122]. This scattering process is proportional to the number of occupied states in the bottleneck region as well as in the LP ground state, therefore a pronounced stimulated scattering process into the ground state sets in provided a certain population threshold is reached. In consequence, a macroscopic population of the ground state occurs, i.e. a polariton condensate. In the last step photons leak out of the cavity mediated by the photonic component of the LP states, which share the same properties such as energy and in-plane wavevector with the polaritons inside the cavity (Step 4). Therefore no population inversion between the crystal ground state and the LP ground state is needed for a lasing operation in this system, only a compensation of the losses due to the radiation out of the cavity by stimulated scattering is required. This gives rise to the hope of a more efficient lasing operation of polariton lasers with respect to energy consumption.

However, the stability of the light-matter coupled excitons (here the 1s heavy-hole (hh) excitons) is a prerequisite for the operation of a polariton laser, whereas no polariton lasing can occur, when the excitonic states are ionized, which is referred to as the weak coupling regime. The transition between the phase of stable excitons and dissociation of excitons is called Mott-transition, which describes in general a transition between an insulating and a conducting phase in condensed matter [123]. To warrant the stability of the coupled excitons the choice of two experimentally accessible parameters is crucial:

Firstly, there is an upper bound for the applied lattice temperature, as the excitons remain stable only as long as the thermal fluctuations, which are determined by the lattice temperature, are smaller than the exciton binding energy. For GaAs quantum wells typical exciton binding energies lie on the order of 10 meV, which corresponds to a lattice temperature of roughly 100 K. This is clearly a limitation concerning room temperature operation of a polariton laser in GaAs-based microcavities and indeed an upper bound of 70 K for polariton lasing operation has been observed so far for this system [124,125]. More promising in this respect are wide bandgap semiconductors such as ZnO and GaN, exhibiting exciton binding energies of 60 meV in ZnO bulk material [126] and up to 50 meV in GaN quantum wells [127], or organic semiconductors [128].

The other limitation for polariton laser operation arises from the fact that excitons become instable, provided a certain saturation density of carriers excited in a semiconductor is reached, which is also known as Mott-density. The reason for this bleaching of the exciton resonances is attributed to screening effects [129, 130] and phase space filling [129]. In simple words, screening can be understood as follows: The creation of an increasing number of e-h pairs leads to a renormalization of the bandgap, i.e. the width of the bandgap decreases, whereas the exciton resonances do not shift remarkably in energy due to the charge neutrality of the bound state. At large densities the excitonic resonances disappear and are replaced by the electronic continuum, which is shifted to lower energies. Typical carrier densities in this regime correspond to approximately one free carrier per exciton volume in the crystal, which can be descriptively interpreted as a screening effect of the hydrogen-like Coulomb interaction between the electron and hole in the undisturbed exciton [129]. Phase space filling is related to the fact that the creation of an exciton also implies the occupation of the single-particle phase space, as an exciton consists of a linear combination of electron and hole states, respectively. As electrons and holes are fermionic particles, they obey the Pauli exclusion principle. Hence, already occupied states in phase space cannot contribute to the formation of excitons, which leads in consequence to a decrease of the exciton oscillator strength.

The dependence of the exciton oscillator strength f on the carrier density can phenomenologically be described by the following function [131]:

$$f(n_{\mathrm{e-h}}) = \frac{f_0}{1 + n_{\mathrm{e-h}}/n_{\mathrm{sat}}}, \tag{4.1}$$

where f_0 denotes the oscillator strength for an e-h pair density of $n_{\mathrm{e-h}} = 0$ and n_{sat} the saturation carrier density. Typical values for n_{sat} are in the range of $10^{10} - 10^{11}$ cm^2 (Refs. [131,132] and references therein). The oscillator strength is linked with the Rabi splitting by the relation

$$\hbar\omega_{\mathrm{r}} = \sqrt{f(n_{\mathrm{e-h}})}\hbar\omega_{\mathrm{ex}}. \tag{4.2}$$

Consequently, with increasing e-h density the oscillator strength of the exciton decreases as well as the Rabi splitting. At high e-h densities the inequality (2.35) is no longer satisfied, the strong coupling regime breaks down and polaritons are not anymore eigenstates of the microcavity system.

Therefore, the maximum pump power for a polariton laser is limited, as a transition from the strong- to the weak coupling regime occurs, when the threshold carrier density is exceeded. Moreover, in the weak coupling regime the cavity emits coherent laser radiation due to population inversion between the conduction and the valence band, respectively, which is difficult to distinguish from polariton lasing, as both regimes share several features such as a nonlinear input-output curve and coherent emission of radiation.

In the last years condensation of polaritons, exhibiting similar features as compared to BEC (see Sec. 2.4.5), which is a prerequisite for a polariton laser device, was reported for different material systems such as CdTe [24], ZnO [126], GaN [60] and GaAs [133].

Furthermore, the operation of an electrically pumped polariton laser has already been demonstrated for a GaAs-based semiconductor compounds at cryogenic temperatures of 10 K [18, 19]. In addition, several groups succeeded in the performance of room temperature operation studying wide bandgap semiconductors [60, 61] and organic semiconductors [62, 63] under non-resonant optical pumping. Recently, an electrically pumped polariton laser operating at room temperature for a GaN-based microcavity has been reported [20].

Great progress has also been achieved concerning the requirement to distinguish polariton lasing operation from conventional cavity lasing (CL) operation in the weak coupling regime: The observation of a Zeemann-splitting, which occurs only under polariton condensation conditions due to the excitonic fraction of polaritons [18, 134], the occurrence of a two-threshold behavior of the input-output curve, the emission energy and the second order coherence function [124, 135] as well as temporally resolved measurements [136] allow for a precise distinction between these two regimes of lasing.

However, on the road towards a polariton laser, systematic studies need to be performed in order to determine the optimal operating parameters. Detailed investigations of the threshold power dependence on the lattice temperature and the exciton-cavity detuning for GaN- [137,138] and CdTe-based [139,140] microcavities were accomplished. In contrast, for GaAs-based microcavities there exist only studies for one single detuning [124] or for a limited range of temperatures and detunings [141].

In this section a systematic investigation of the phase transitions to polariton lasing and CL for a wide range of temperatures and detunings in a GaAs-based microcavity is presented. In this connection, an upper limit of temperature of 90 K and a lower limit of $\delta = E_c - E_x = -12$ meV of detuning for polariton lasing in the investigated sample is determined, where E_c (E_x) denotes the energy of the cavity (exciton). A clear distinction between the regime of CL and polariton lasing is also provided by means of spectrally and temporally resolved measurements.

4.1.2 Experimental details

The investigated sample is a GaAs-based $\lambda/2$-microcavity with a Q-factor of about 1800. The design of the sample is as follows: Three stacks of four GaAs quantum wells are placed in the three central antinodes of the electric field confined by two distributed Bragg reflector (DBR) structures in the microcavity. The upper (lower) DBR structure consists of 16 (20) alternating layers of $\mathrm{Al_{0.2}Ga_{0.8}As}$ and AlAs. The interaction of the cavity field with the exciton resonance of the 12 contained GaAs quantum wells leads to a Rabi splitting of about 14 meV. It should be noted that the microcavity exhibits a thickness gradient, i.e. the cavity resonance energy varies across the sample. In consequence, the exciton-cavity detuning depends on the position of the sample.[*]

Fig. 4-2 shows a schematic diagram of the experimental setup used for the experiments presented in this section. The sample is mounted in a helium-flow cryostat, measurements are performed in a temperature range of $10 - 110$ K. For optical excitation a picosecond-pulsed Titanium-Sapphire laser (repetition rate 75.39 MHz) is tuned to a wavelength of

---

[*] The sample has been manufactured in the institute of Technical Physics of Würzburg University. The identifier of the sample is C1059.

744 nm (1666 meV). The laser beam is focused under 45° of incidence onto the sample, the shape of the spot is Gaussian and about 30 µm in diameter. The excitation laser power can be varied by means of two grayscale filters mounted in reversed orientation, which minimizes the displacement and the inhomogeneity of the laser beam in contrast to using one grayscale filter only.

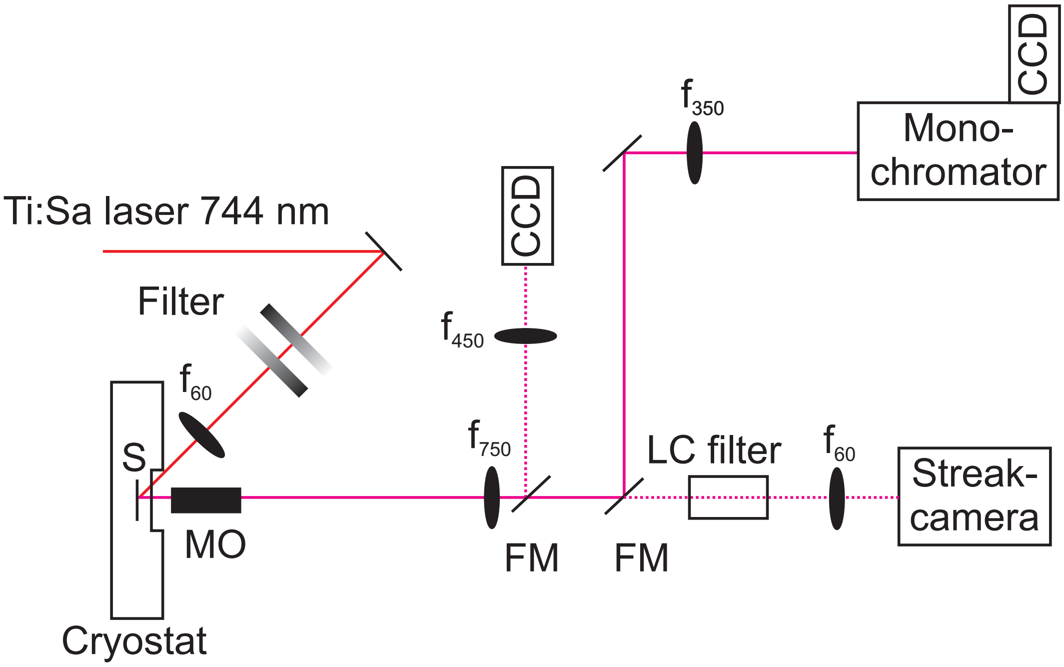

Figure 4-2: Schematic diagram of the experimental setup. CCD, charge coupled device camera; f_{xx}, lens with xx mm focal length; FM, flipmirror; LC filter, tunable liquid crystal filter; MO, microscope objective (numerical aperture 0.26); S, sample.

The emission from the sample is collected using a microscope objective (numerical aperture 0.26); the far field emission was studied by imaging the Fourier plane of the objective onto the entrance slit of a monochromator using two lenses (see e.g. Ref. [55,142] for details). For detection a liquid nitrogen-cooled CCD-camera was used. For a precise focusing and positioning of the excitation laser spot onto the sample, an intermediate image is captured using an additional CCD camera behind a focusing lens. Time-resolved measurements are accomplished with a streak camera (time resolution 2 ps). Here, spectral resolution is provided by a liquid crystal filter (full width at half maximum 0.7 nm) positioned in front of the streak camera.

4.1.3 Results and discussion

Fig. 4-3 and Fig. 4-4 show examples of far field emission images for different excitation power levels P for detunings of $\delta = -7.0$ meV and $\delta = 7.7$ meV at $T = 10$ K. For the negative detuning case one observes a blue shift of 1.9 meV with respect to the minimum of the lower polariton (LP) branch at the phase transition to polariton lasing [$P = P_{thr}$, Fig. 4-3(b)]. Note that a rather broad distribution of the polariton condensate with respect to the in-plane wavevector can be observed, which is caused by a broad distribution of background carriers injected by the comparably large excitation laser spot of 30 µm in diameter [143], whereas the in-plane wavevector distribution changes

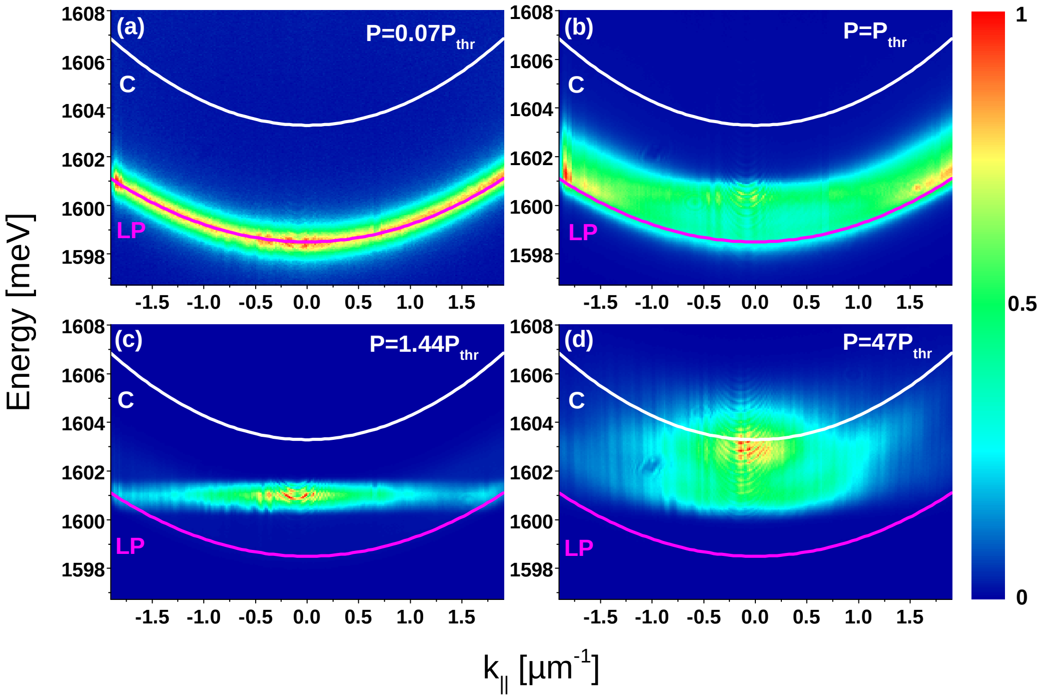

Figure 4-3: Far field emission for different excitation power levels at $\delta = -7.0$ meV. The solid lines are calculated dispersion curves. C, cavity dispersion; LP, lower polariton dispersion. (a) Below threshold power the main emission originates from the calculated LP dispersion. (b) and (c): Slightly above threshold power polariton lasing, blueshifted in energy by 1.9 meV with respect to the minimum of the LP branch, is observed. (d) For high excitation powers two different modes can be seen.

significantly when the diameter of the excitation laser spot is reduced by one order of magnitude (see chapter 5). The blueshift of the emission is due to repulsive polariton-polariton and polariton-background carrier interactions (see Sec. 5.2 for more details). At high excitation power two different modes occur [Fig. 4-3(d)]. The low energy mode is identified as polariton lasing and the high energy mode as bare CL, which is in good agreement with the calculated dispersion. The occurrence of the strong and the weak coupling regimes arises due to the carrier density changing during one excitation pulse (see also Fig. 4-5). In contrast, for the positive detuning case a rather large blue shift of 13.8 meV at the phase transition to polariton lasing is observed [Fig. 4-4(b)]. Surprisingly polariton lasing occurs at higher energies than the expected cavity mode. At slightly higher excitation power of $P = 1.56 P_{thr}$ one further mode appears at an energy even above the upper polariton branch [Fig. 4-4(c)].

For this experimental setting an additional streak camera measurement is performed [Fig. 4-5]. The high energy peak exhibits a pulse duration (FWHM) of about 6 ps. After the decay of the high energy peak, the low energy peak rises with a pulse duration of about 15 ps. This observation can be interpreted as follows: After decrease of the carrier density a transition back to the strong coupling regime takes place; the bare CL breaks down and polariton lasing arises. Thus, high and low energy peaks can be attributed to bare CL and to polariton lasing, respectively. A transition from the weak- to the strong coupling regime during one excitation pulse was also observed previously [136].

For high excitation power, only a single mode is observed [Fig. 4-4(d)], which can be

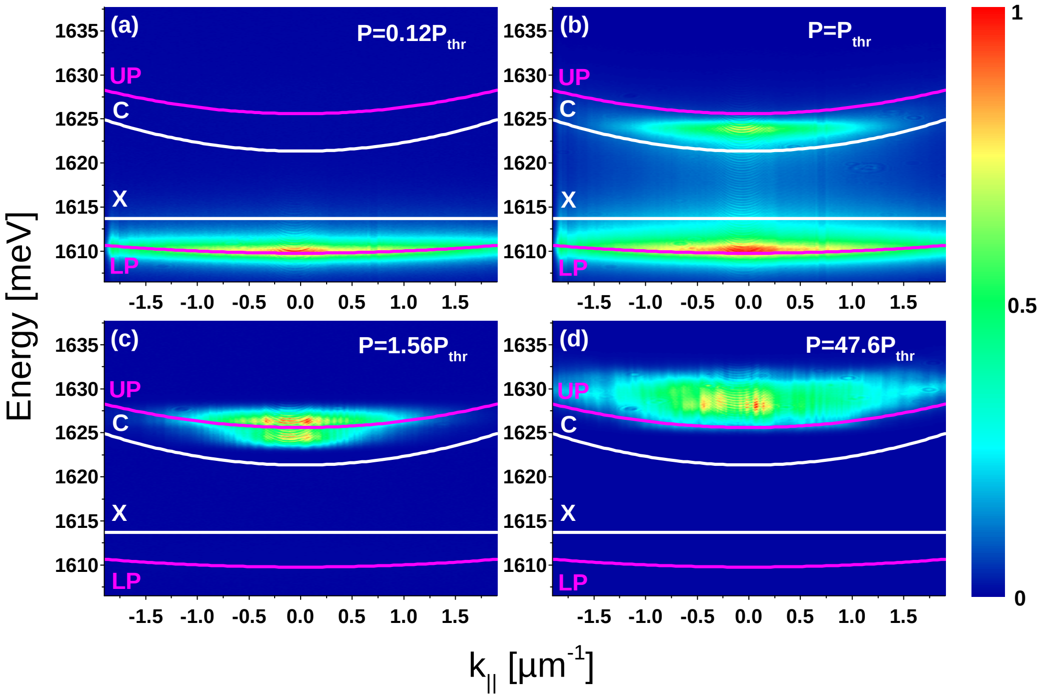

Figure 4-4: Far field emission for different excitation power levels at $\delta = 7.7$ meV. The solid lines are calculated dispersion curves. C, cavity dispersion; LP, lower polariton dispersion; UP, upper polariton dispersion; X, exciton dispersion. (a) Below threshold power the main emission originates from the calculated LP dispersion. (b) At threshold power polariton lasing, blueshifted in energy by 13.8 meV with respect to the minimum of the LP branch, is observed. (c) Slightly above threshold power two different modes can be identified. (d) For high excitation powers only one mode can be seen.

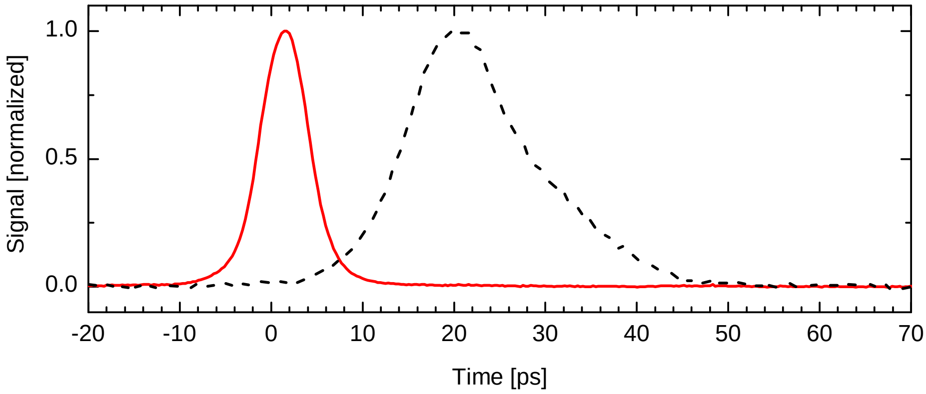

Figure 4-5: Time-resolved emission at $\delta = 7.7$ meV, $T = 10$ K and $P = 1.56P_{thr}$. Spectral sensitivity is provided by a tunable liquid crystal filter. Red line, $E = 1626.9$ meV; black dashed line, $E = 1624.0$ meV.

attributed to CL. Fig. 4-6 shows the detuning dependent emission energies (in-plane momentum $k_{||} = 0$) at different temperatures for low power excitation, excitation at threshold and $P > 10P_{thr}$. At threshold for $T = 10$ K, a significant blueshift varying from $1.5 - 13.8$ meV relative to the minimum of the LP branch occurs [Fig. 4-6(a)]. The largest blueshift is observed at $\delta = 7.7$ meV, the smallest at $\delta = -6.3$ meV. For $\delta > 5$ meV, the emission at threshold is even higher in energy than the expected cavity

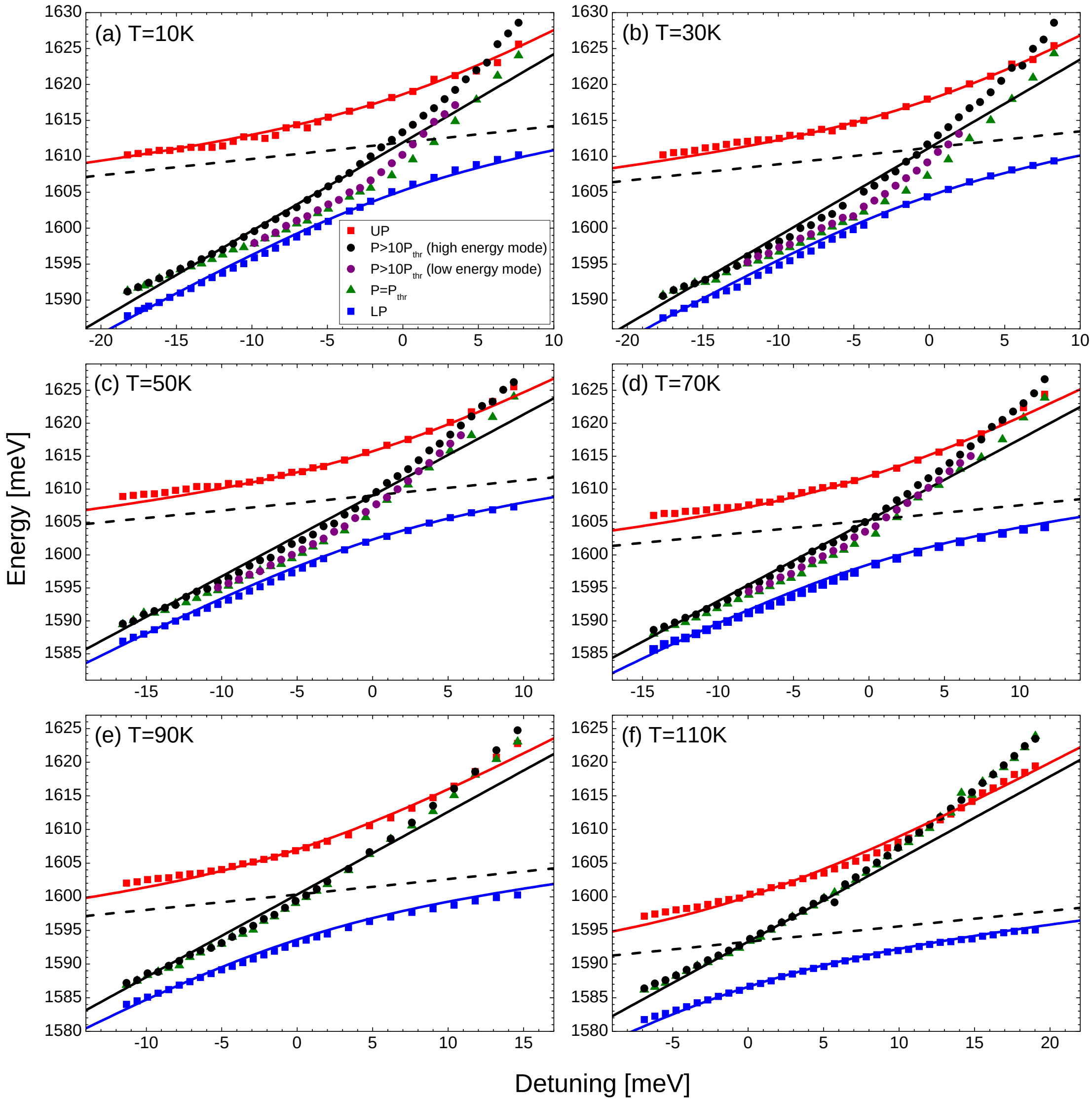

Figure 4-6: Detuning dependent emission ($k_{||} = 0$) at different temperatures. Solid blue (red) line, lower (upper) polariton branch fitted to the data; black solid line, expected cavity mode; black dotted line, expected exciton energy. Note that for $T = 10 - 70$ K two mode emission is not observed for several positive detunings at high power excitation $P > 10P_{thr}$, but for intermediate excitation power (typically $P < 3P_{thr}$).

mode. At large negative detuning $\delta < -12$ meV, the emission lies approximately at the expected cavity mode. In the case of high excitation power, two emission modes can be seen in a range of $\delta = [-10; 3]$ meV as discussed in detail above for the case of $\delta = -7.0$ meV [Fig. 4-3(d)]. Time-resolved measurements reveal the same results as shown in Fig. 4-5. The high energy peak has a pulse duration of about $6 - 7$ ps and is followed at later times by the low energy peak with a pulse duration of about $15 - 30$ ps. As mentioned before, the high (low) energy mode can be attributed to pure CL (polariton lasing). Also for $\delta > 3$ meV, two mode emission can be found, but only in the case of intermediate excitation power (typically $P < 10P_{thr}$, [Fig. 4-4(c)]). For $\delta < -13$ meV no significant shift in energy can be observed when increasing the excitation power from $P = P_{thr}$ to $P > 10P_{thr}$. This can be explained by a direct transition to CL without occurrence of polariton lasing.

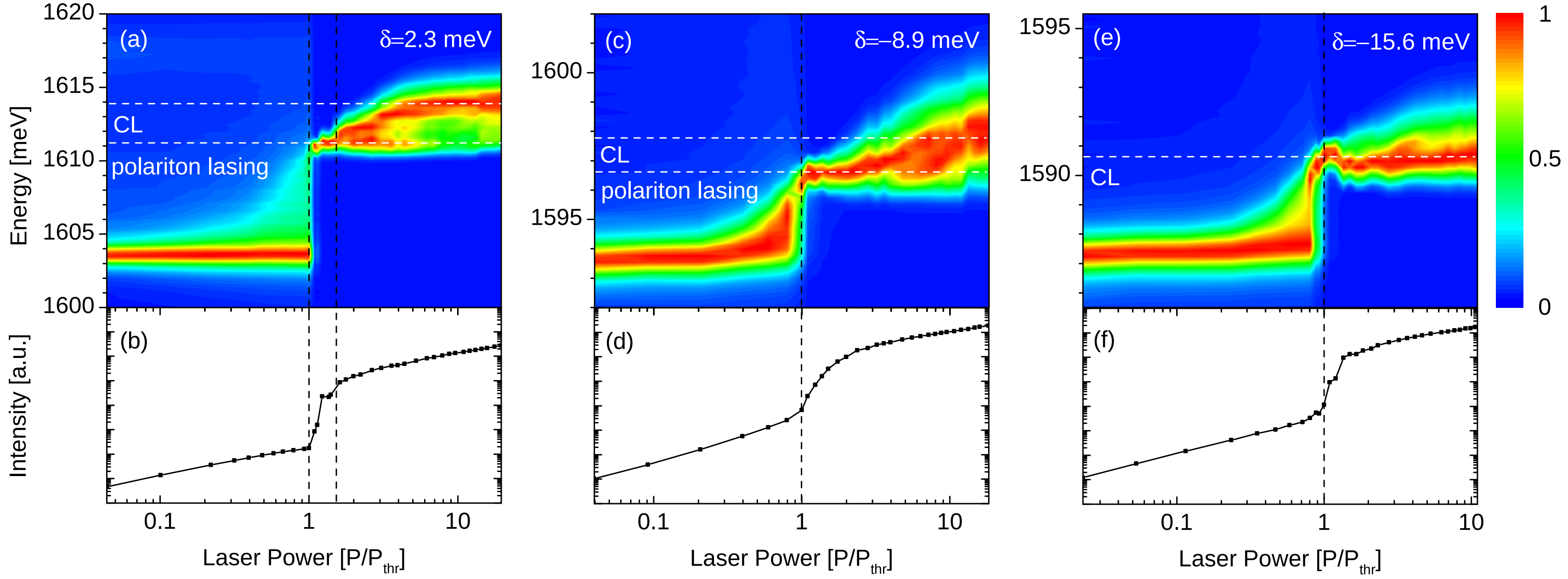

Figure 4-7: Power dependent spectra (in-plane momentum $|k_{||}| < 0.085\ \mu\text{m}^{-1}$) [(a), (c) and (e)] and corresponding I-O curves [(b), (d) and (f)] for three different detunings $\delta = 2.3$ meV, $\delta = -8.9$ meV and $\delta = -15.6$ meV at $T = 50$ K. Modes of emission are indicated by white dashed lines, thresholds in the I-O curves are indicated by black dashed lines. Laser power is normalized to the first threshold power P_{thr}. Note: Power dependent spectra are divided by the maximum signal intensity for each laser power separately.

From these findings, one can identify three criteria that need to be fulfilled to observe a phase transition to polariton lasing: (i) emission energy $E < E_c$ at threshold for negative detuning, (ii) occurrence of two modes for excitation power levels above threshold in pulsed regime and (iii) further blueshift of the emission when increasing the excitation power far above threshold. According to these criteria polariton lasing can be observed in a range of $\delta = [-9.8; 7.7]$ meV for $T = 10$ K [Fig. 4-6(a)], $\delta = [-12.0; 8.3]$ meV for $T = 30$ K [Fig. 4-6(b)], $\delta = [-10.3; 9.3]$ meV for $T = 50$ K [Fig. 4-6(c)] and $\delta = [-8.0; 11.6]$ meV for $T = 70$ K [Fig. 4-6(d)]. Note, however, that the upper δ-bound is determined by the sample edge that does not allow larger positive detunings. Moreover, the detuning at a given position on the sample depends on the temperature, as the exciton resonance is much more redshifted with increasing temperature compared to the cavity resonance. In consequence, the accessible detuning range is shifted to larger positive values for increased temperatures (see Fig. 4-7).

Apparently there exists a lower bound with respect to detuning for polariton lasing for the investigated structure, when reaching a negative detuning on the order of magnitude of the Rabi splitting. This finding coincides with earlier measurements on the same sample at quasi-resonant excitation in which a lower bound for polariton lasing was observed at $\delta = -10$ meV [75]. On the other hand, it is very well known that polariton condensation can be achieved in principle for even larger negative detunings for GaAs-based microcavities exhibiting larger Q-factors on the order of 10000 (see Ref. [144] and chapter 5 in this thesis). Therefore the observed lower bound of $\delta = -12$ meV, which corresponds to a photonic fraction of 83 % of the LP ground state, does not represent a fundamental barrier for polariton condensation, but can be attributed to the comparably low Q-factor of 1800 of the investigated sample, which corresponds to a rather short cavity lifetime of 2 ps. The larger the photonic fraction of the LP, the smaller is the density of states of the LP at small in-plane wavevectors. Therefore the number of scattering channels is significantly reduced for large negative detunings. In addition the LP lifetime decreases with decreasing detuning and is mainly given by the cavity lifetime for large negative detunings, which is rather short due to the comparable low Q-factor of the investigated microcavity. Consequently, the combination of a reduced scattering cross section and a short LP lifetime prevents polariton condensation in this sample for a photonic fraction of the LP ground state exceeding 83 %.

At temperatures above $T = 90$ K no phase transition to polariton lasing occurs since there is only one mode observable and no significant further blueshift can be seen when increasing the excitation power far above threshold [Fig. 4-6(e) and (f)]. This finding is in good agreement with earlier results at $\delta = 0$ meV [124].

For all temperatures a prominent blueshift of CL with respect to the expected cavity mode can be observed for positive detunings, whereas for negative detunings the CL energy coincides with the estimated cavity energy [Fig. 4-6]. This seems to contradict studies in which a redshift of the cavity mode was reported [145, 146]. However, in these studies continuous wave lasers were used which create a rather equilibrated background carrier distribution in contrast to the experimental situation here. On the other hand, a blueshift of the cavity mode with increasing carrier density was reported by another group at negative detuning [71].

In addition, the dependence of the emission intensity on the excitation power is investigated. Fig. 4-7 shows example input-output (I-O) curves and the corresponding power dependent spectra (in-plane momentum $|k_{||}| < 0.085\ \mu\mathrm{m}^{-1}$) at three different detunings. For detunings of $\delta = 2.3$ meV and $\delta = -8.9$ meV two modes of emission and an additional blueshift when increasing the laser power above threshold can clearly be seen [Fig. 4-7 (a) and (c)]. In contrast, for a large negative detuning of $\delta = -15.6$ meV only one mode of emission without additional blueshift is observed [Fig. 4-7 (e)]. Therefore one can conclude that for $\delta = 2.3$ meV and $\delta = -8.9$ meV polariton lasing can be achieved, whereas in the latter case only CL occurs. Earlier, it has been claimed that the observation of a two-threshold behavior in the I-O curve is a prerequisite for the occurrence of polariton lasing [145]. According to the presented data this is not necessarily the case: Whereas there is evidence for two thresholds in the I-O curve in the case of $\delta = 2.3$ meV [Fig. 4-7 (b)], only a single threshold occurs for $\delta = -8.9$ meV [Fig. 4-7 (d)]. From previous reports it is well known that a two-threshold behavior in the I-O curve can be very pronounced in structures exhibiting further confinement, such as nanowires [147] and micropillars [148]. However, there are only few publications in which such an effect was observed in planar microcavities [124, 125, 135]. Here, it should be emphasized that the two-threshold criterion with respect to the I-O curve might be sufficient, but it is not a prerequisite for the observation of polariton lasing.

Fig. 4-8 shows dependence of threshold power on detuning at different temperatures. The lowest threshold is observed for $T = 10$ K and $\delta \approx 6$ meV. When going to negative detuning the polariton lasing threshold power increases due to less efficient scattering into the $k_{||} = 0$-state and shortened LP lifetime. On the other hand, when going to positive detuning the effective mass rises due to higher exitonic fraction of the LP, which results in an increment of the critical density according to Eq. (2.43) and therefore the threshold might increase again for $\delta > 6$ meV. Note, however, that the carrier density injected into the sample may vary for different detunings as the corresponding reflection minima of the DBR structure are dependent on the detuning (see Sec. 4.2.3.2), whereas the excitation laser energy was kept constant at about 744 nm.

Interestingly there is no sharp increase of the threshold power observable, when going from the strong to the weak coupling regime around $\delta = [-12; -8]$ meV in the temperature range of $T = 10 - 70$ K. The inset of Fig. 4-8 shows the dependence of threshold power on lattice temperature for three different detunings ($\delta = -5$ meV, $\delta = 0$ meV and $\delta = 5$ meV), in which polariton lasing can be achieved up to $T = 70$ K. While there is a systematic rise of the threshold power with increasing temperature, there is no significant jump observable between the strong coupling regime at $T = 70$ K and the weak coupling regime at $T = 90$ K. A rather small increase of threshold, namely a doubling, was recently reported in a high-finesse GaAs-based microcavity for $\delta = -5$ meV when going from strong to weak coupling regime in a temperature range of $T = 25 - 70$ K [125]. For a similar configuration ($\delta = -5$ meV, $T = 30 - 90$ K) an increase by a factor of 4 is observed here.

4.1.4 Summary

In conclusion, far field measurements on a GaAs-based microcavity over a wide range of detunings and temperatures have been performed at different excitation powers. A clear boundary between the strong and the weak coupling regime at threshold power has been identified by far field and time-resolved spectroscopy. A lower limit of -12 meV

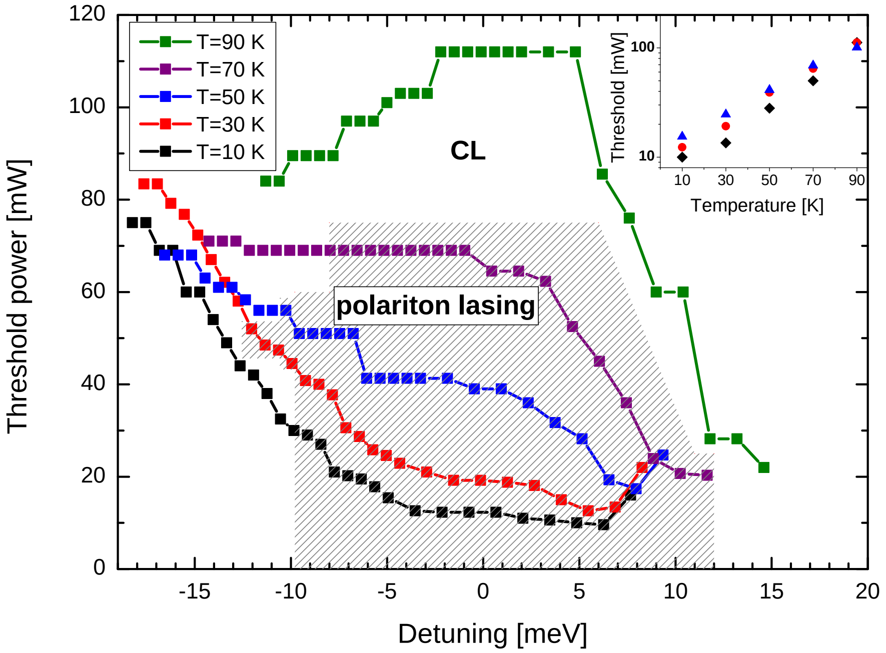

Figure 4-8: Dependence of threshold power on detuning for different lattice temperatures. Data points inside (outside) of the shaded area are attributed to polariton lasing (CL). Inset: Dependence of threshold power on lattice temperature for different detunings. Black diamonds, $\delta = 5$ meV; red circles, $\delta = 0$ meV; blue triangles, $\delta = -5$ meV.

for detuning and an upper temperature of 90 K was found for achieving polariton lasing in the investigated sample. While the lattice temperature of 90 K poses a fundamental barrier for polariton lasing, which is given by the exciton binding energy on the order of 10 meV, polariton lasing for even more negative detunings can be achieved provided a microcavity exhibiting a significantly larger Q-factor is studied. Moreover, the threshold power does not appear to be an appropriate criterion to identify the bounds for polariton lasing in the $\delta - T$ parameter space since there is no significant rise in threshold power observable when leaving the polariton lasing regime. Further, it has been shown that the observation of two thresholds in the I-O curve is not a prerequisite for the occurrence of polariton lasing in this study.

4.2 Nonlinear spectroscopy of exciton-polaritons in a GaAs-based microcavity

4.2.1 Introduction

While THz spectroscopy is an appealing tool for a wide range of applications such as investigation of biomolecules, material evaluation and security issues, e.g. tracing of illegal drugs (Ref. [149] and references therein), the number of available laser sources in this spectral region is rather limited. Furthermore, all coherent THz sources available so far suffer from certain drawbacks, as they are either bulky and expensive (e.g. free electron lasers), exhibit low efficiencies [e.g. THz radiation generated by optical mixing techniques and photocarrier acceleration in photoconducting antennas (Ref. [150] and references therein)], or can only be operated below room temperature and require a complicated design (quantum cascade lasers [151]). Therefore, the identification of new reliable THz sources is currently a dynamic field of research [152].

Recently, a design for a vertical cavity surface emitting THz laser based on the stimulated THz transition between a dipole-forbidden $2p$ exciton state and the lower exciton-polariton in a microcavity has been proposed [31]. Fig. 4-9 (a) shows a schematic illustration of the operating principle of the THz lasing device according to Ref. [31]. $2p$ exciton states are pumped by a two-photon excitation process, as they cannot be accessed by a one photon process due to the selection rules. The $2p$ state can decay into the LP ground state accompanied by the emission of a photon. As the energy difference between the LP ground state and the $2p$ exciton lies roughly in the range of $10-50$ meV for typical semiconductor microcavity systems, such as GaAs, GaN and ZnO, the emitted photons lie in the THz frequency range. The system can be understood in terms of a three-level system, therefore on first sight one might assume that a population inversion between the $2p$ exciton and the LP ground state is required here. This is, however, not the case as the considered structure [Fig. 4-9(b)] does not possess a resonator for THz radiation. Consequently, THz radiation is immediately released from the microcavity and is not reabsorbed. Hence, the THz generation rate T can simply be described by the following expression [31]:

$$T \propto N_{\mathrm{p}}(N_{\mathrm{s}}+1), \tag{4.3}$$

where N_{s} (N_{p}) denotes the occupation number of the LP ground state ($2p$ state). Therefore THz lasing sets in simultaneously with the occurrence of a macroscopic population of the LP ground state.

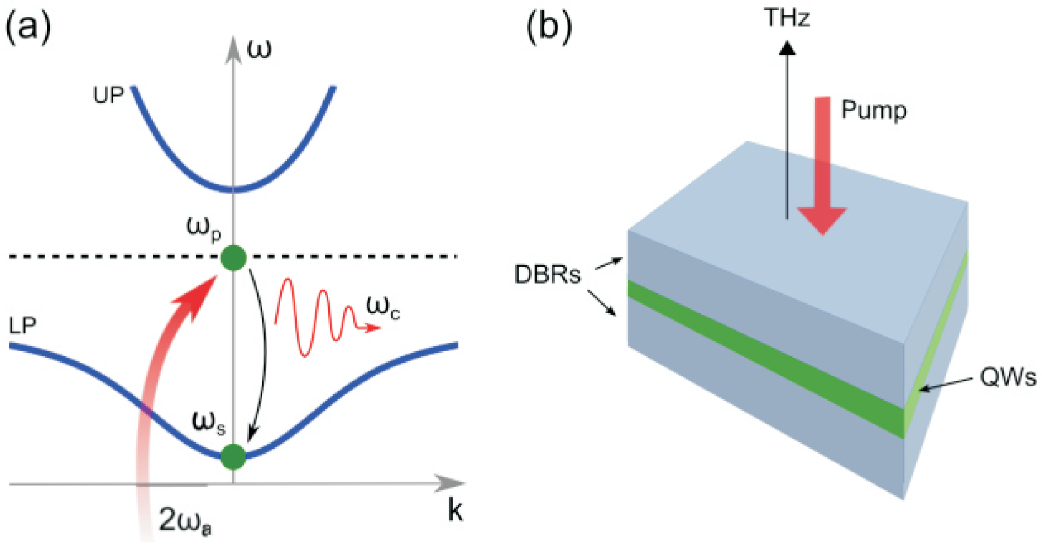

Figure 4-9: Principle of operation for a THz lasing device according to the proposal of Ref. [31]. (a) Schematic illustration of the dispersions of the involved states. The $2p$ exciton states (dashed line, frequency ω_{p}) are populated by a two-photon excitation process with a pump frequency of $\omega_{\mathrm{a}} = \omega_{\mathrm{p}}/2$. The $2p$ state can decay radiatively to the LP ground state (frequency ω_{s}) under emission of THz radiation with frequency $\omega_{\mathrm{c}} = \omega_{\mathrm{p}} - \omega_{\mathrm{s}}$. (b) Considered structure for a THz lasing device: A standard semiconductor microcavity consisting of an active layer containing quantum wells sandwiched between two DBRs. THz emission is expected to occur perpendicular to the microcavity plane. Image is taken from Ref. [31].

While there are encouraging proof of principle studies for the feasibility of a polariton laser device, as has been discussed in the previous section of this chapter, there is no unambiguous evidence for THz-lasing operation so far. For an evaluation of the feasibility of the proposal of Ref. [31], a careful investigation of the occurring two-photon processes in a semiconductor microcavity is necessary. Recently, two-photon excitation of polaritons in a GaAs-based microcavity system was reported [153]. In this study a femtosecond-pulsed laser with a spectral width of 13 meV, more than two times larger than the Rabi splitting in the investigated sample, was used, which did not allow for energy-resolved two-photon excitation spectroscopy (TPE spectroscopy). The strong emission of the UP and LP state at resonant excitation was interpreted in terms of $2p$ exciton injection followed by decay under stimulated THz-emission into polariton states. Unfortunately, the $2p$ exciton state could not be unambiguously identified in this study due to the limited spectral resolution of the laser system, which would have given even stronger evidence for the interpretation of the authors. Furthermore, a second harmonic generation (SHG) process at the LP and UP state energies might also explain the pronounced emission observed from these states for resonant pumping.

The focus of this section lies on a systematic investigation of the occurring two-photon excitation processes in a GaAs-based microcavity. Here, a tunable nanosecond-pulsed OPO with a spectral width of 0.3 meV is used, allowing for energy-resolved TPE and SHG spectroscopy. Therefore, a distinction between two-photon absorption (TPA) and SHG processes is rendered possible.

4.2.2 Experimental details

The investigated sample is the same as the one described in Sec. 4.1.2. Fig. 4-10 shows a schematic diagram of the experimental setup used for the study presented in this section. The sample is mounted in a helium-flow cryostat, measurements are performed at 10 K. For two-photon excitation a nanosecond-pulsed optical-parametric oscillator (OPO) pumped with a repetition rate of 10 Hz by the third harmonic of a Nd:YAG laser is used. The divergence of the OPO beam is compensated by a cylindrically shaped lens with a focal length of 300 mm. The excitation power of the OPO can be varied using a half-wave plate and a Glan-Taylor prism, the polarization of the OPO is adjusted by a further half-wave plate. A longpass filter suppresses the SHG generated from the half-wave plates.

For TPE spectroscopy the elliptically shaped laser beam is focused under 45° degrees of incidence onto the sample with main axes of 100 µm and 500 µm, respectively (dashed gray line in Fig. 4-10). For SHG spectroscopy, excitation under normal incidence using a beamsplitter and a microscope objective is chosen for the sake of wavevector conservation (solid gray line in Fig. 4-10). Here, the main axes of the elliptically shaped spot measure 20 µm and 100 µm, respectively. For a precise focusing and positioning of the excitation laser spot onto the sample, an intermediate image is captured using an additional CCD camera behind a focusing lens.

TPE spectroscopy is used to investigate non-resonant TPA processes. In this connection, the detection energy remains fixed in an energy range of 3.3 meV centered around the LP energy, while the wavelength of the OPO is tuned in a range of typically 1465 – 1565 nm (792 – 846 meV).

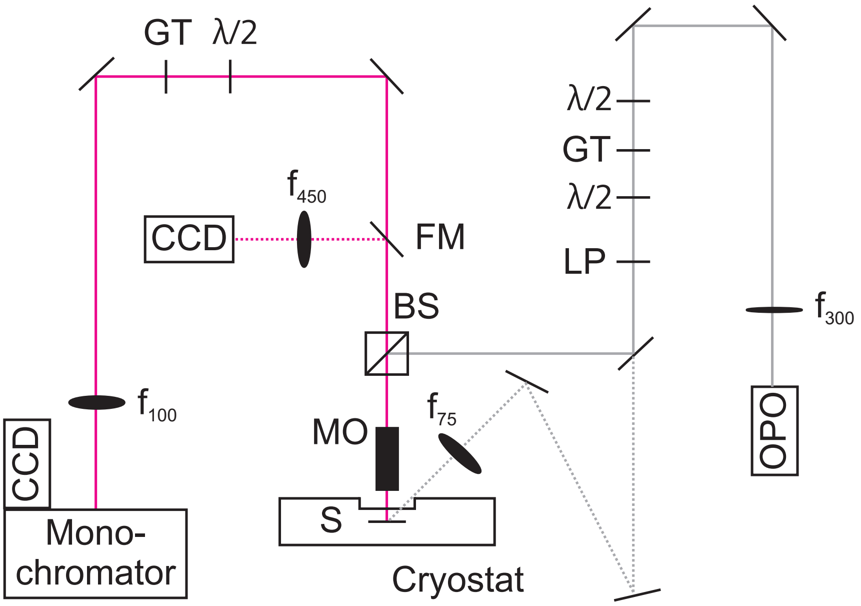

Figure 4-10: Schematic diagram of the experimental setup. BS, beam splitter; CCD, charge coupled device camera; f_{xx}, lens with xx mm focal length; FM, flipmirror; GT, Glan-Taylor prism; $\lambda/2$, half-wave plate; LP, longpass filter (cut-off wavelength 1400 nm); MO, microscope objective (numerical aperture 0.26); OPO, optical-parametric oscillator; S, sample.

Furthermore, SHG spectroscopy is utilized as a complementary experimental technique, in which only resonant two-photon processes are considered. In this connection, the detection wavelength is tuned in combination with the wavelength of the OPO and always corresponds to the two-photon energy of the OPO. The combination of both experimental techniques using a nanosecond-pulsed OPO system with a rather narrow linewidth of 0.3 meV compared to femtosecond-pulsed laser systems allows for a clear distinction between non-resonant TPA processes and coherent SHG.

The emission from the sample is collected using a microscope objective (numerical aperture 0.26). The polarization dependence of the emission is determined by rotation of a half-wave plate in front of a Glan-Taylor prism. For detection a thermoelectric-cooled CCD-camera behind a monochromator is used.

4.2.3 Results and discussion

This section is split into two parts. In Sec. 4.2.3.1 non-resonant TPA processes are studied and the feasibility of an efficient population of the $2p$ exciton is evaluated, whereas in Sec. 4.2.3.2 coherent SHG processes in GaAs-based microcavities are revealed.

4.2.3.1 TPE spectroscopy

Fig. 4-11 (a) shows a typical TPE spectrum. The strong rise in signal intensity above 1620 meV is attributed to the intersubband transition between the highest heavy hole subband and the lowest conduction subband. The oscillations superimposed on the increasing signal intensity above 1620 meV with a periodicity of roughly 12 meV [indicated by black dotted lines in Fig. 4-11 (a)] are caused by a modulation of the reflectivity in the infrared spectral range due to the DBR. A comparison with data presented in Sec. 4.1 (Fig. 4-12) allows to clearly identify the two resonances below 1620 meV in Fig. 4-11 (a) as 1*s* exciton and LP, respectively.

The LP energies observed here are slightly larger compared to the data presented

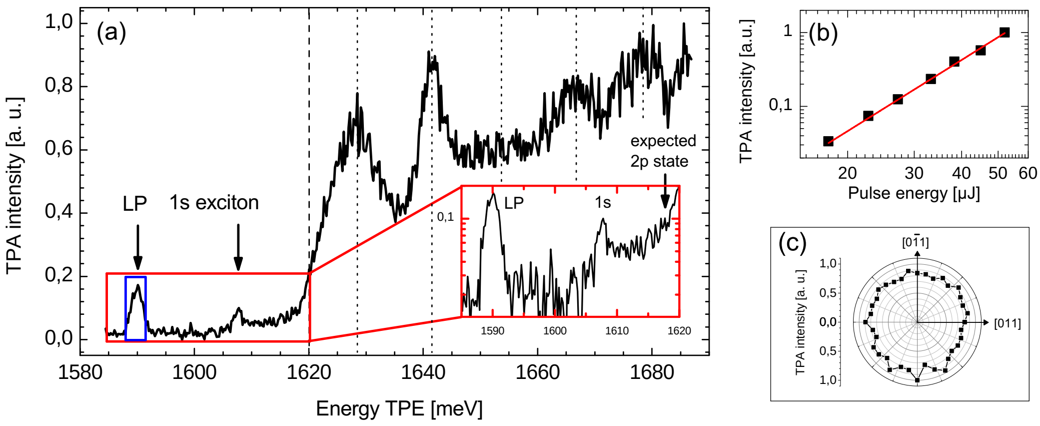

Figure 4-11: (a) TPE spectrum for a detuning $\delta = E_c - E_x = -16.8$ meV, where E_c (E_x) denotes the energy of the cavity (exciton). The pulse energy of the OPO is kept constant at about 50 µJ. The onset of the lowest intersubband transition is indicated by the black dashed line. The oscillations superimposed on the increasing signal intensity above 1620 meV due to the DBR are marked by black dotted lines. The detection energy range is indicated by the blue rectangle. Inset: Close-up of the TPE spectrum below the intersubband transition. Above 1605 meV an increase of the TPE signal can be observed. (b) Dependence of signal intensity of the LP on the pulse energy of the OPO for a two-photon energy of 1653 meV. Black squares, data; red line, power-law fit $y = a \cdot x^p$ with $p = 3.20 \pm 0.15$. (c) Polarization dependence of the TPA intensity for an incoming polarization of the OPO in [011] direction. Signal intensity is proportional to the radial distance from the center. The two-photon energy lies at 1653 meV, the pulse energy is 42 µJ.

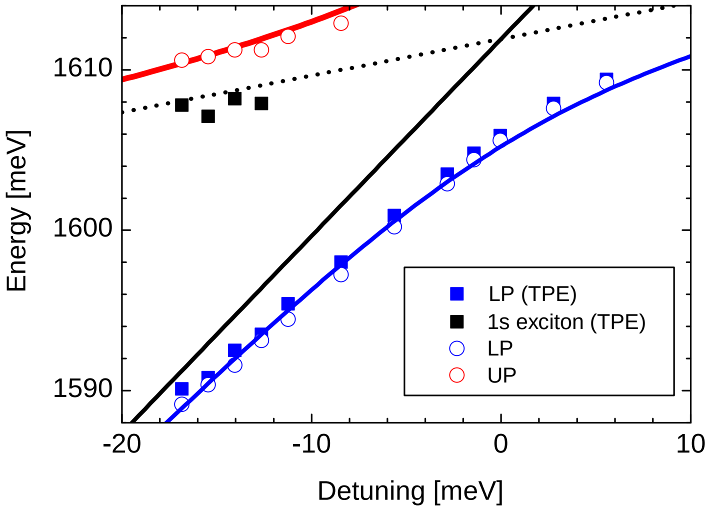

Figure 4-12: Dependence of the observed resonance energies below the subbandgap. Full squares are taken from TPE spectra. Open dots and solid lines are taken from Fig. 4-8 (a). Black solid line (dotted line) is the calculated cavity (1*s* exciton) energy.

in Sec. 4.1 due to integration over a broad distribution of LP states with different in-plane momenta, whereas the data of Sec. 4.1 are related to the LP state at $k_{||} = 0$ only. We do not observe any resonance corresponding to the UP energy in the TPE spectra [Figs. 4-11 (a) and 4-12]. Note that the radiative transition between the UP and LP state is forbidden due to parity conservation, which can only be overcome for the case of hybridization of the UP with an exciton exhibiting a different parity [154]. However, this requires a careful design of the sample and is not a generic effect. Further, for a phonon-assisted relaxation process, the emission of acoustic phonons is required, as the energy splitting between the UP and LP is roughly a factor of two smaller than the longitudinal optical phonon energy. Therefore, we believe that SHG is the dominating process compared to TPE of the LP via the UP, when the two-photon energy is resonant to the UP (see Sec. 4.2.3.2).

Scattering from the 1*s* exciton to LP states is only observed at large negative detunings, corresponding to a photonic fraction of the LP ground state larger than 80 % (Fig. 4-12). A close-up of the TPE spectrum [inset of Fig. 4-11 (a)] reveals an onset of the TPA process at roughly 1605 meV. Beside the 1*s* exciton, no further exciton resonances can be observed in the TPE spectrum. The 2*p* exciton is expected to lie roughly 10 meV higher in energy compared to the 1*s* exciton in GaAs quantum wells [155], which is only 2 meV below the intersubband transition. A clear identification of the 2*p* exciton is therefore challenging.

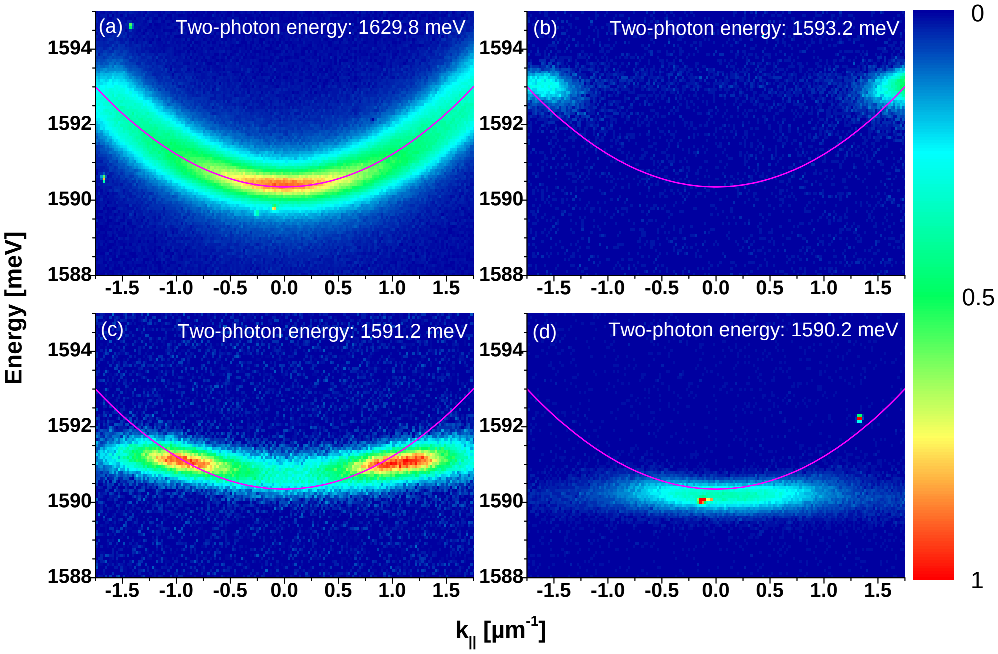

Figure 4-13: Far field emission for excitation with different two-photon energies at $\delta = -15.4$ meV. The excitation pulse energy is about 50 µJ. (a) Emission of polaritons exhibiting a broad distribution of in-plane momenta can be observed under non-resonant excitation. (b)-(d): For the case of resonant excitation only emission of polaritons corresponding to the two-photon energy of the OPO can be seen. The solid line corresponds to the calculated LP dispersion.

This finding agrees with previous studies: While clear evidence for P-states in TPE experiments [156, 157] between the $N = 2, 3, 4$ subbands of GaAs quantum wells was reported, only unpronounced steps in photoconductivity measurements [155] or even

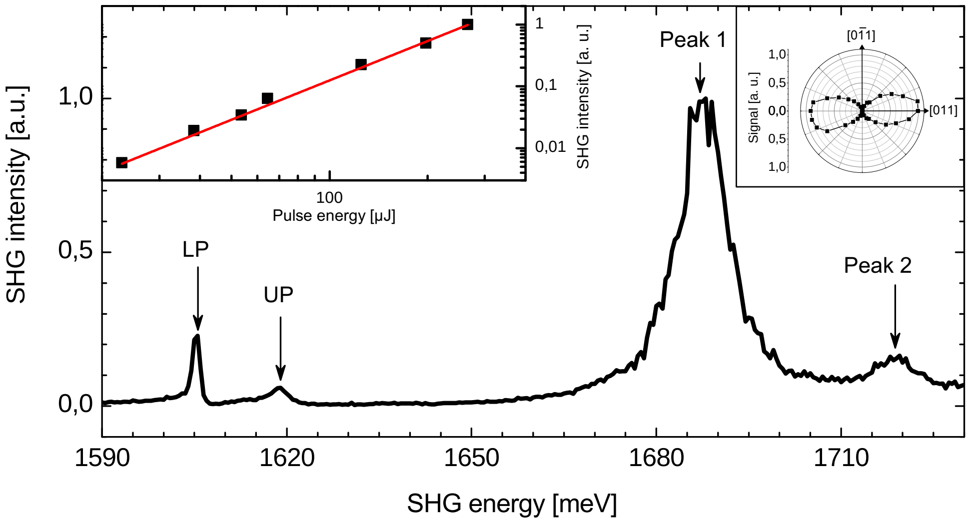

Figure 4-14: SHG spectrum for $\delta = -0.7$ meV. LP and UP resonances can be clearly identified. Left inset: Dependence of signal intensity of the LP resonance on the pulse energy of the OPO. Black squares, data; red line, power law fit $y = a \cdot x^p$ with $p = 2.11 \pm 0.09$. Right inset: Polarization dependence of the SHG emission at the LP energy for an incoming polarization of the OPO in [011] direction. Signal intensity is proportional to the radial distance from the center.

only a broad tail [158] in TPE signal intensity below the subbandgap have been observed as signatures of the $2p$ exciton of the lowest $N = 1$ intersubband transition in GaAs-based quantum wells. Note that a THz excitation of the $2p$ exciton from a polariton condensate was very recently reported, which allows for the differentiation between cavity and polariton lasing [159].

However, the absence of a pronounced $2p$ exciton resonance in TPE spectroscopy might indicate a low two-photon pumping efficiency of the LP via this channel. The detection of THz radiation is a challenging task, typically bolometers at cryogenic temperatures are used. Therefore a careful analysis of the transition energies and the THz wavelength to look for facilitates the actual detection. Most likely, materials with a higher exciton-binding energy such as ZnO or GaN are more promising for the realization of a THz laser device as proposed in Ref. [31], since the identification of $2p$ exciton states is expected to be more feasible in this materials.

In Fig. 4-11 (b) the dependence of the LP emission on the pulse energy of the OPO is shown for the case of non-resonant two-photon excitation. The data can be approximated well using a power-law function $y = a \cdot x^{3.2 \pm 0.15}$. On first sight this seems surprising since one expects a quadratic dependence for a TPA process. However, since the signal is detected at the LP, not only the creation of electron-hole pairs above the subbandgap contributes to the signal intensity, but also the relaxation mechanism into LP states is important. Relevant relaxation processes below the condensation threshold are spontaneous acoustic-phonon scattering for polaritons with large wavevectors and polariton-polariton scattering for LPs scattering into the groundstate at $k_{||} = 0$ [121]. The probability for the first process is independent of the reservoir density of polaritons with large in-plane momenta, the latter one exhibits a quadratic dependence. In combination with the quadratic TPA process this yields an overall quadratic dependence for the case of acoustic phonon scattering and a fourth degree polynomial dependence for the case of polariton-polariton scattering. The cubic behavior observed here demonstrates that both mechanisms are of relevance since the emission from a broad distribution of wavevectors is detected. Note, however, that the dynamic range for the choice of the pulse energy is limited to roughly 50 µJ due to reaching the destruction threshold of the sample in the case of non-resonant excitation. Fig. 4-11 (c) shows the polarization dependence of the TPA intensity under non-resonant two-photon excitation. Clearly, an isotropic emission can be observed as expected for a non-resonant excitation process.

Fig. 4-13 shows the far field emission for different excitation energies. In the case of non-resonant excitation, where the two photon-energy is larger than the subbandgap, a broad distribution of LPs with different wavevectors is populated [Fig. 4-13 (a)]. In contrast, only LPs with the corresponding two-photon energies can be observed for the case of resonant excitation [Fig. 4-13 (b)-(d)]. Further, there is no evidence for relaxation towards the LP ground state at $k_{||} = 0$ [Fig. 4-13 (b)], which indicates a SHG process.

4.2.3.2 SHG spectroscopy

To substantiate this interpretation, in addition, SHG spectroscopy is performed. In this connection, only resonant two-photon processes are considered, as outlined in Sec. 4.2.2.

Fig. 4-14 shows a typical SHG spectrum. LP and UP resonances can be clearly identified, and moreover, two further resonances at 1688 meV and 1720 meV can be observed, which will be discussed below. The dependence of the LP SHG intensity on the pulse energy of the OPO exhibits a quadratic behavior as expected for a SHG process (left inset of Fig. 4-14) in contrast to the observed cubic behavior for the TPA process as discussed before. Furthermore, a pronounced polarization anisotropy of the emission is observed, which gives additional evidence for SHG (right inset of Fig. 4-14), whereas the polarization of the LP emission is isotropic for a non-resonant TPA process [Fig. 4-11 (c)].

SHG spectroscopy has been performed for several different detunings δ (Fig. 4-15). For the LP and UP states the expected anticrossing can be seen, whereas the other two peaks exhibit a monotonous increase in energy with respect to the detuning. In addition, transfer matrix calculations have been performed in order to determine spectral positions of the reflection minima of the DBR structure from the growth parameters of the investigated sample.[†] As one can see in Fig. 4-15 the observed peaks are in good agreement with the expected energies of the reflection minima of the wedge shaped DBR. Therefore, these peaks can be attributed to the first and second reflection minima of the DBR, respectively.

Furthermore, the ratio of the intensity of the LP resonance and the UP resonance in the SHG spectra is analyzed (Fig. 4-16). Whereas SHG of the UP dominates for a photonic fraction of the LP of less than 50 %, which corresponds to a photonic fraction of the UP larger than 50 %, SHG of the LP is more than one order of magnitude stronger for the case of a photonic fraction of 90 % of the LP. This behavior reveals a strong

---

[†] Calculations have been performed by Thomas Czerniuk of Institute of Experimental Physics 2 of TU Dortmund University.

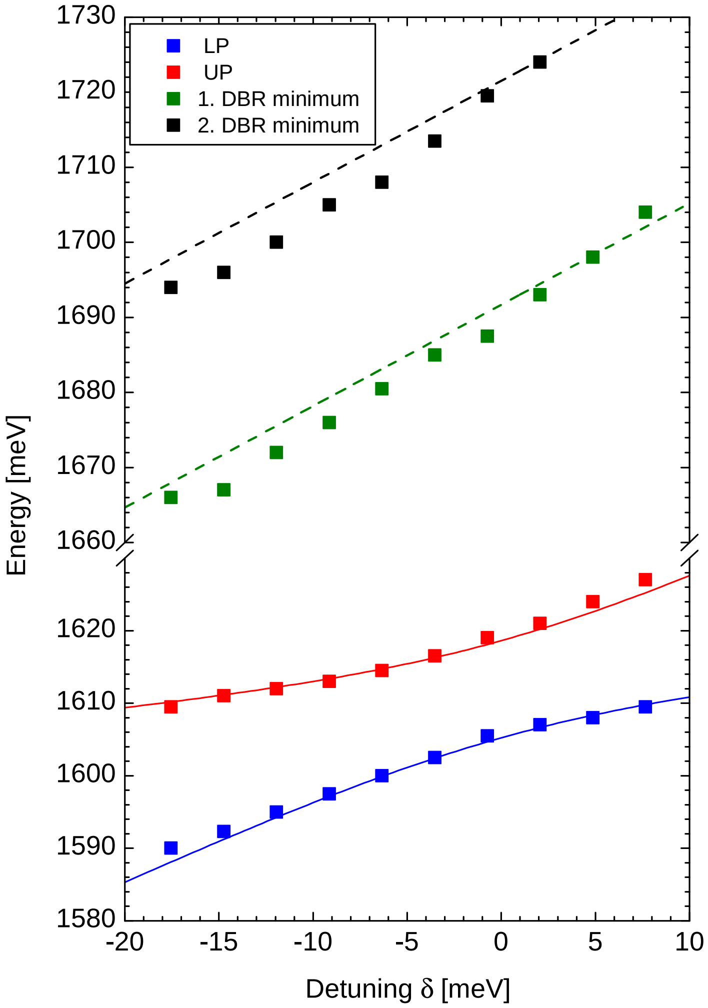

Figure 4-15: Dependence of the resonance energies in the SHG spectrum on detuning. Green and black dashed lines indicate the calculated energies of the first and second reflection minima of the DBR, respectively.

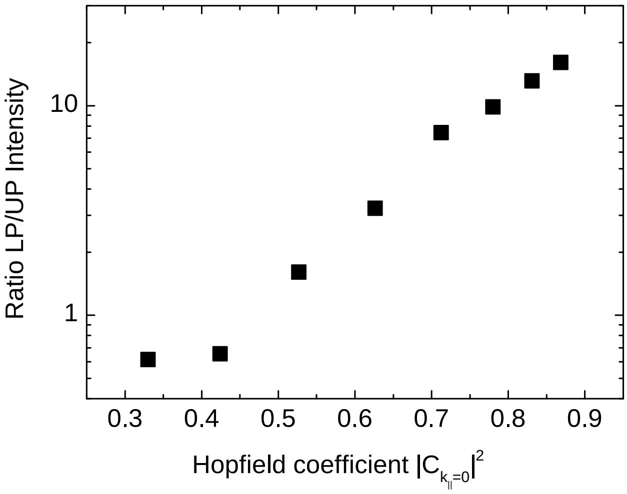

Figure 4-16: Ratio of the SHG intensity of LP and UP depending on the Hopfield coefficient $|C_{k_{||}=0}|^2$, which determines the photonic fraction of the LP.

dependence of the SHG efficiency on the photonic fraction of the polaritons.

4.2.4 Summary

In conclusion, a systematic study of the two-photon processes occurring in a GaAs-based microcavity in the strong coupling regime has been performed. Pronounced SHG from the LP, UP and reflectivity minima of the DBR have been observed, at which the photonic fraction of the polaritons is crucial for the SHG efficiency. However, clear evidence for an efficient population of the $2p$ exciton by a two-photon process, which is a requirement for a THz lasing device based on microcavity polaritons, has not been observed by TPE spectroscopy [31]. Wide bandgap semiconductors such as GaN and ZnO, exhibiting larger exciton binding energies, are more appealing for the realization of such a device, as they should allow for a more straightforward identification of the $2p$ excitons and therefore facilitated detection of THz radiation.

It has been clearly demonstrated that SHG is a pronounced mechanism occurring in GaAs-based microcavities. Further studies investigating two-photon pumping processes of polaritons in GaAs-based microcavities should always rule out SHG to get unambiguous evidence for a TPA process.

For further experiments, a detailed study of the polarization anisotropy of the SHG at high magnetic fields should reveal the selection rules for SHG in GaAs-based microcavities as was demonstrated before for GaAs bulk material [160].

Chapter 5

Coherence properties and flow control of propagating polariton condensates

In this chapter the propagation of polariton condensates in microcavities is studied. In the first part of this chapter the coherence properties of a propagating polariton condensate in a photonic wire are investigated. Here, two complementary experimental techniques, namely a second-order correlation measurement as well as a Young's double-slit experiment are used. In the second part, the creation and manipulation of a directed propagation of an polariton condensate by optically induced potentials is studied. By using a spatial light modulator (SLM), arbitrarily shaped potentials can be generated, which allow for an accurate control of the propagation of the polariton condensate injected by non-resonant optical pumping. For the experiments presented in this chapter microcavities exhibiting a large Q-factor on the order of 10000 are required to obtain a flow of polariton condensates propagating several 10 µm away from the excitation laser spot. The first part of this chapter has already been published in similar form in Ref. [161]. Some of the results of the first part of this chapter are also presented in the bachelor's thesis of Ö. Bayraktar [162], which was supervised by the author of this thesis.

5.1 Influence of interactions with non-condensed particles on the coherence of a 1D polariton condensate

5.1.1 Introduction

As already discussed in Sec. 4.1.1, a polariton laser promises low power consumption as it operates without the need for population inversion. For practical applications the carriers have to be injected non-resonantly with significant excess energy, e.g., by electrical currents, as demonstrated very recently [18–20]. Consequently, during relaxation a broad distribution of background carriers is generated. This might limit the performance of such a device in terms of coherence of the emission due to interaction between condensed polaritons and uncondensed particles. Comparative linewidth measurements on 2D polariton condensates indicated that the separation of reservoir carriers from the polariton condensate may improve the coherence properties of the latter [163].

Polariton condensates in 2D cavity structures [55, 164, 165] are not only affected by interaction with background carriers but also undergo considerable scattering among the polaritons themselves. Such scattering is elastic in that the energy in the polariton system is maintained. In 2D cavities the phase space of possible scattering events is rather large so that the bare effect of background carriers on the coherence of the polariton condensate is hard to assess. In particular this is the case when the coherence underneath the laser spot only is studied as in Refs. [55, 164, 165]. Promising in this respect are photonic wire structures, in which the polariton scattering is suppressed due to the reduced phase space accessible for quasi-elastic scattering in one dimension. Propagation of polariton condensates several 10 µm away from the excitation laser spot has been demonstrated in these structures [88].

In the first part of this chapter a spatially resolved study of the coherence properties of a laser-excited 1D polariton condensate is presented. In this connection, first and second-order correlation functions of the emission from polariton condensates are investigated. Both correlation functions demonstrate a reduced coherence of the polariton condensate when background carriers are present. This loss of coherence is attributed to interactions between background carriers and the polariton condensate. Two different effects contribute to the interaction: (i) The Coulomb-potential mediated by the background carriers and (ii) non-resonant scattering between background carriers and polaritons. However, a detailed evaluation of the exact contributions of these effects is beyond the scope of this work.

5.1.2 Coherence of a light source

As the coherence properties of a polariton laser are investigated in the first part of this chapter, the term coherence shall briefly be defined within this section.

5.1.2.1 Coherence in classical optics

In classical optics the term coherence is related to the observability of interference effects, which requires a fixed phase relation between two light waves. As an experimentally accessible quantity the term coherence is related to the first-order correlation function:

$$g_1(\mathbf{r_1}, t_1, \mathbf{r_2}, t_2) = \frac{\langle E^-(\mathbf{r_1}, t_1) E^+(\mathbf{r_2}, t_2)\rangle}{\sqrt{\langle |E(\mathbf{r_1}, t_1)|^2\rangle \langle |E(\mathbf{r_2}, t_2)|^2\rangle}}, \tag{5.1}$$

where E^+ (E^-) represent the positive (negative) frequency parts of the Fourier integral of the electrical field E [168]. Note that in quantum theory E^+ and E^- are identified as the photon annihilation and creation operators, respectively. Here, the first-order spatial correlation functions $g_1(\mathbf{r_1}, t, \mathbf{r_2}, t)$ and temporal correlation functions $g_1(\mathbf{r}, t_1, \mathbf{r}, t_2)$ are of particular interest as the measurement of these quantities allows for the determination of the coherence length l_c and coherence time τ_c. First-order spatial correlations can be experimentally accessed e.g. by Young's double-slit experiment (see Sec. 5.1.4.2) or Michelson interferometry at zero time-delay in a retroreflector configuration [24, 169]. First-order temporal correlations can be determined e.g. using a Michelson interferometer with varying temporal delay between both optical paths of the interferometer. In this connection, the visibility of the observable interference fringes is a direct measure of first-order temporal and spatial coherence, respectively (see Sec. 5.1.4.2). However, the definition of coherence in classical optics is not related to the inherent properties of a light source, as the first-order coherence of light can be manipulated during propagation, e.g. arbitrarily large first-order temporal and spatial coherence can be generated by spatial and spectral filtering of thermal light sources.

5.1.2.2 Quantum theory of optical coherence

The successful realization of the first laser by Theodore Maiman [170], however, raised questions concerning the fundamental distinction between a laser and a conventional thermal light source exhibiting first-order coherence, i.e. long coherence time and large coherence length. A useful quantity for differentiation between these two types of light sources is the second-order temporal correlation function, given by

$$g_2(t,\tau) = \frac{\langle \hat{a}^\dagger(t)\hat{a}^\dagger(t+\tau)\hat{a}(t)\hat{a}(t+\tau)\rangle}{\langle \hat{n}(t)\rangle \langle \hat{n}(t+\tau)\rangle}, \tag{5.2}$$

where $\hat{a}$, $\hat{a}^\dagger$ and $\hat{n}$ are the photon creation, annihilation and number operator of the mode of interest. For stationary light fields Eq. (5.2) is averaged in time, giving rise to the function $g_2(\tau)$. $g_2(\tau)$ can be regarded as a measure for the probability of detecting a second photon delayed by a time τ after the detection of the first photon and therefore elucidates the photon emission statistics of a light source. Independent of the particular light source, for large time delays with respect to the coherence time, the photon emission events are uncorrelated, i.e. $g_2(\tau >> \tau_c) = 1$. Second-order correlations were experimentally accessed for the first time by Hanbury Brown and Twiss in the 1950s [171], who observed correlated, i.e. increased, photon emission arising from a -according to the classic definition- coherent thermal emitter at time of coincidence $\tau = 0$. On the other hand, second-order correlation measurements performed on the first available laser in the 1960s revealed no correlated photon emission at small temporal delays [172].

The reason for this deviation in second-order correlation lies in the different emission statistics of a thermal emitter and a laser. Whereas the photon number distribution of a single mode of a thermal emitter obeys a Bose-Einstein distribution, a Poissonian distribution reflects an ideal laser. Inserting these photon number distributions into the temporal average of Eq. (5.2) reveals $g_2(0) = 1$ for a laser and $g_2(0) = 2$ for a thermal light source (see Ref. [173] for details).

A more stringent condition for optical coherence was formulated by Roy Glauber in 1963 [168]. According to his definition, nth-order coherence requires

$$g_j(t_1, ..., t_j) = 1,\ j \leq n. \tag{5.3}$$

Here,

$$g_j(t_1, ..., t_j) = \frac{\langle : \prod_{i=1}^{j} \hat{a}^\dagger(t_i)\hat{a}(t_i) : \rangle}{\prod_{i=1}^{j} \langle \hat{n}(t_i)\rangle} \tag{5.4}$$

denotes the jth order correlation function and the double stops indicate normal ordering of the photon creation and annihilation operators, respectively, which describes the probability of a joint j-photon detection event. A coherent state, which is an eigenstate of the photon annihilation operator [174], fulfills Eq. (5.3) for arbitrary n, which describes the light field of an ideal laser. On the other hand, a thermal emitter obeys the relation [175]

$$g_j(0) = j!, \tag{5.5}$$

which has been experimentally evidenced for polariton emission in the thermal regime up to third order [176]. Arbitrarily high order correlation functions are of course not accessible in a real experiment, but measurements of second-order correlations can provide a strong evidence for a Poissonian photon number distribution, which indicates a coherent state.

5.1.3 Experimental details

A GaAs-based $\lambda/2$-microcavity with an experimentally determined Q-factor of about 10000 is investigated. The design of the sample is as follows: Three stacks of four GaAs quantum wells are placed in the three central antinodes of the electric field confined by two distributed Bragg reflector (DBR) structures in a $\lambda/2$-cavity. The quantum wells are 13 nm in thickness and separated by 4 nm thick barrier layers of AlAs. The upper (lower) DBR structure consists of 23 (27) alternating layers of $\mathrm{Al_{0.2}Ga_{0.8}As}$ and AlAs. The interaction of the cavity field with the exciton resonance of the 12 contained GaAs quantum wells leads to a Rabi splitting of about 10.5 meV. Photonic wires are fabricated by lithography and etching. A wire with the following parameters is studied: The exciton-cavity detuning is $\delta = E_C - E_X = -15.1$ meV. The wire length is $L = 100$ µm and the wire width is $W = 5$ µm.*

Fig. 5-1 shows a schematic diagram of the experimental setup used for real-space imaging, Fourier-space spectroscopy and Young's double-slit experiment, respectively. The sample is mounted in a helium-flow cryostat. Measurements are performed at 10 K. For non-resonant optical excitation a femtosecond-pulsed Titanium-Sapphire laser (repetition rate 75.39 MHz) with central wavelength at 740 nm (1675 meV) is used. A polarizer and a Glan-Taylor prism allow for arbitrary attenuation of the laser beam. The laser beam is focused onto the sample under normal incidence. The shape of the spot is Gaussian and about 2 µm in diameter.

The emission from the sample is collected using a microscope objective (numerical aperture 0.42). The far field emission is studied by imaging the Fourier plane of the objective onto the entrance slit of a monochromator. For detection a liquid nitrogen-cooled CCD-camera is used. For real-space imaging the photonic wire is magnified by a factor of 87.5 and projected onto the entrance slit of a monochromator, using a lens with $f = 350$ mm (dashed ellipse in Fig. 5-1) instead of the lenses $f = 400$ mm and $f = 750$ mm (filled black ellipses in Fig. 5-1), respectively, used for far field imaging.

To study the spatial coherence of the polariton condensate along the wire, Young's double-slit experiment is performed. To this end, the emission from the sample is mag-

---

*The investigated sample has been manufactured in the institute of Technical Physics of Würzburg University. The identifier of the sample is M4159-7.1.

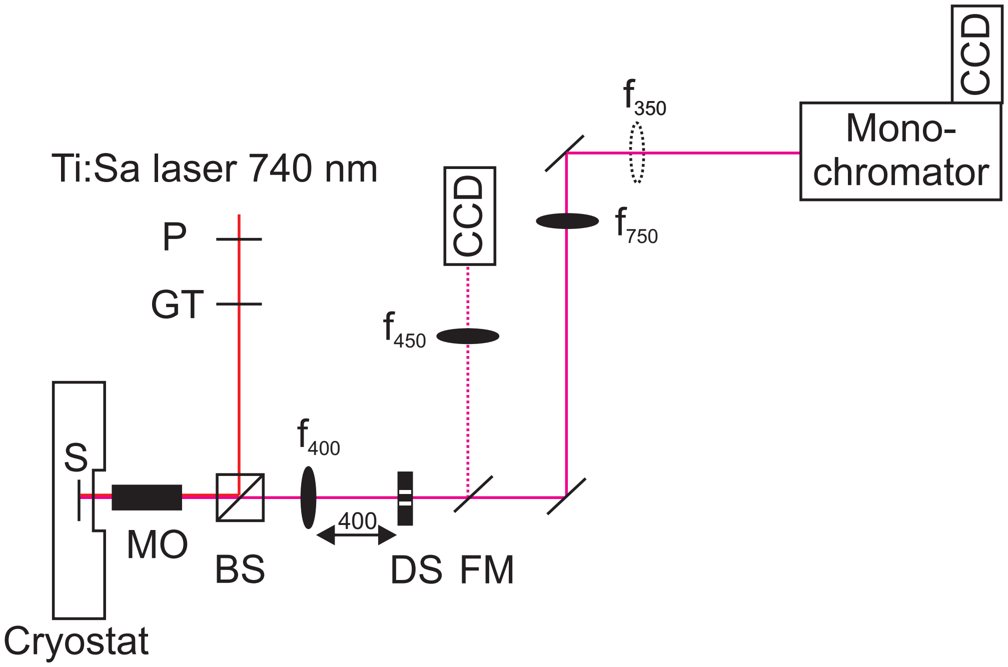

Figure 5-1: Schematic setup for real-space imaging, Fourier-space spectroscopy and Young's double-slit experiment: BS, beam splitter; CCD, charge coupled device camera; DS, doubleslit; f_{xx}, lens with xx mm focal length; FM, flip mirror; GT, Glan-Taylor prism; MO, microscope objective (focal length 4 mm, NA 0.42); P, polarizer; S, sample.

nified by a factor of 100 onto four different double slits. Thereby the spatial coherence between two small areas of diameter $b = 0.4$ µm with distances of $a = 1.25$ µm, 2.5 µm, 5 µm and 7.5 µm can be investigated. The interference fringes are recorded with the CCD camera behind the monochromator. Contrary to previous reports [55, 88, 164, 165], the location of the slit center d with respect to the excitation laser spot is chosen as an additional variable to investigate spatial coherence. $d = 0$ corresponds to placing the double slit symmetrically with respect to the excitation laser spot. From the observed interference fringes the visibility $V = \frac{I_{max}-I_{min}}{I_{max}+I_{min}}$ within a spectral range of 0.5 meV is calculated, which is used as measure for first-order spatial coherence.

For the measurement of $g_2(\tau)$, the streak camera setup described in Ref. [167] is slightly modified. A drawback of the experimental approach presented there lies in photon reconstruction errors of the built-in streak camera routine in the single photon counting mode especially for short time delays $\tau < 1 - 2$ ps. This prevents a direct determination of the g_2-function for $\tau = 0$, which can only be extrapolated from values of the g_2-function for larger τ. Due to these photon reconstruction errors one can speak of a dark time on the order of 2 ps. A similar problem occurs when measuring photon-statistics using avalanche photodiodes, which exhibit a dark time on the order of 100 ns. To circumvent this problem, in conventional Hanbury-Brown-Twiss (HBT) setups two avalanche photodiodes are used. Similar to a HBT setup, the streak-camera can be used as two effective detectors by means of the following approach:

The emission of the photonic wire is split into two different optical paths delayed by 72.5 ps in time, thereby giving access to $g_2(\tau' = 72.5 \text{ ps}) = g_2(\tau = 0)$, where τ reflects the real time delay between the detection of two photons and τ' the time delay due to the artificial time delay given by different optical path lengths. Therefore two

50:50 beamsplitters and a shortpass (SP) filter with cut-off wavelength at 800 nm are used (Fig. 5-2). The SP-filter provides transmission of the excitation laser as well as reflection of the investigated polariton-emission from the sample. Both emission patterns are magnified by a factor of 25 onto the entrance slit of a streak camera equipped with an additional horizontal deflection unit. The horizontal deflection speed is slow compared to the vertical deflection speed and allows for the recording of multiple streaks per screen. Horizontal time windows of 300 ns, 600 ns and 1200 ns, respectively, can be chosen. The temporal resolution of the setup is approximately 2 ps. Spectral sensitivity is provided by a bandpass filter with a Full Width at Half Maximum (FWHM) of 1 nm.

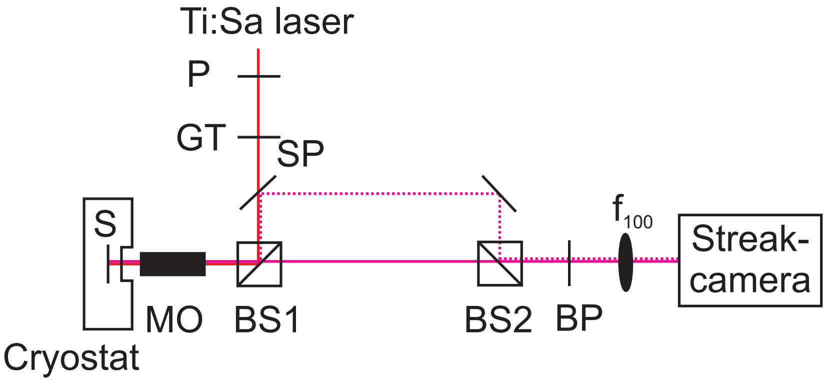

Figure 5-2: Schematic setup for the second-order correlation measurement: BP, bandpass filter (FWHM 1 nm); BS1, BS2, beam splitters; f_{100}, lens with 100 mm focal length; GT, Glan-Taylor prism; MO, microscope objective (focal length 4 mm); S, sample; SP, shortpass filter (cut-off wavelength 800 nm); P, polarizer. Note: Emission path indicated by the dashed line is delayed by 72.5 ps due to optical path length difference.

For the second-order correlation measurement, emission regions of 3 µm width along the wire are selected using a vertical slit, and a horizontal deflection time of 300 ns per screen is used. For a reliable signal to noise ratio 100 000 frames are recorded, Fig. 5-3 (a) shows a typical image integrated over 100 000 frames. Every frame consists of 22 streaks and each streak corresponds to one single excitation pulse. Every detected photon within one frame is assigned to a certain streak and second-order correlation functions are calculated as described in Ref. [167]. A typical example for such a g_2-function is shown by the red line in the inset of Fig. 5-3 (b). However, especially for short pulses the g_2-function can be distorted by jitter-effects as described in Ref. [167], which are indicated by g_2-values significantly below 1. To account for these effects, the g_2-functions between several combinations of different streaks are averaged, which is indicated by the black line in the inset of Fig. 5-3 (b). Since neighboring streaks are separated by 13.2 ns in time, the shape of this curve does not reflect second-order correlation of the emission from the sample, but jitter arising from the streak camera system. By dividing the g_2-function of photons within the same streak by the average of the g_2-functions of photons between different streaks, jitter is separated from second-order correlation of the emission from the sample. Fig. 5-3 (b) gives a typical example of such a normalized g_2-function. Here $g_2(\tau' = 72.5\text{ ps})$ corresponds to $g_2(\tau = 0)$ due to the time delay between the two emission profiles. The additional peak for $\tau' = 40$ ps is probably caused by the tail of the pulse as can be seen in Fig. 5-3 (a).

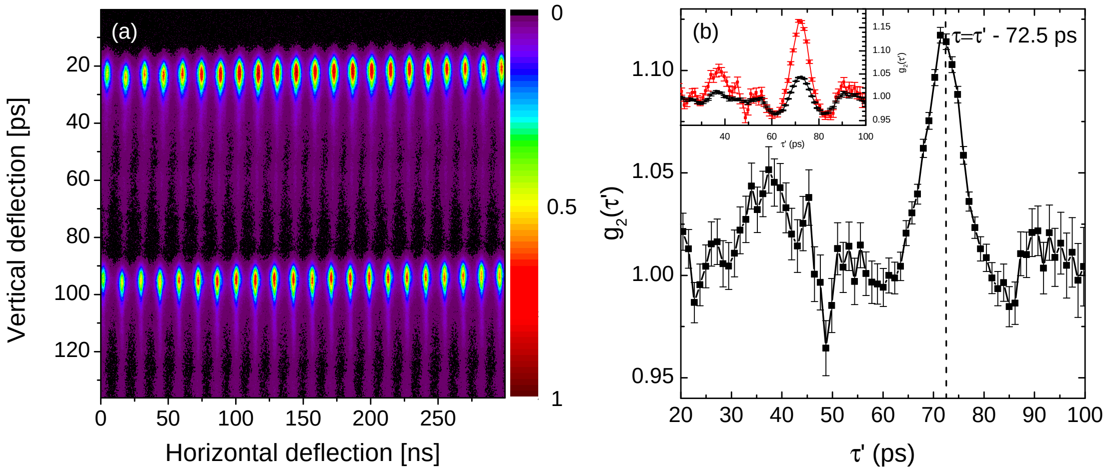

Figure 5-3: (a) Typical image integrated over 100 000 frames when probing a 3 µm section of the photonic wire using a horizontal deflection time of 300 ns. (b) Normalized $g_2(\tau')$-function. Due to the artificial time delay between both profiles, $\tau' = 72.5$ ps corresponds to $\tau = 0$ ps. Inset: Red line, calculated $g_2(\tau')$-function when correlating photons within the same streak; black line, average of the correlation functions when correlating photons between different streaks.

5.1.4 Results and discussion

5.1.4.1 Real-space and Fourier-space spectroscopy

In a photonic wire light is confined normal to the wire axis. In a simple model the confinement of the light can be treated in terms of standing waves, therefore the cavity dispersion is described as follows [177]:

$$E_i(k_x) = \sqrt{E_c^2 + \frac{\hbar^2 c_0^2}{n^2}\left(\frac{\pi^2}{W^2}(i+1)^2 + k_x^2\right)}\ , \tag{5.6}$$

where n is the index of refraction of the cavity material, W is the width of the wire and E_c is the cavity energy of the corresponding planar cavity. The lateral confinement gives rise to a multiplet of subbranches which are labeled $i = 0,1,2$ ... in the following. For convenience the exciton-cavity detuning is defined as the difference in energy between the lowest $i = 0$ cavity subbranch and the uncoupled quantum well exciton.

For identification of the different subbranches of the lower polariton [178] in the photonic wire and evaluation of the propagation of the polariton condensates, real-space and Fourier-space spectroscopy is performed at different excitation powers.

Figs. 5-4 (a) and (b) show the corresponding images for an excitation power below threshold. Here, the excitation laser spot is located at the center of the photonic wire. Several dispersion curves of LP subbranches can be distinguished in Fig. 5-4 (b) and allocated to different photonic wire subbranches. The most intensive mode corresponds to the $i = 0$-subbranch, also weak signatures of the $i = 2$-, $i = 3$- and $i = 4$-subbranches can be observed [Fig. 5-4 (b)]. The reason for the weak signal intensities from higher subbranches is the orientation of the photonic wire parallel to the entrance slit of the monochromator, leading to a small detection range in k_y-space ($|k_y| < 0.12$ µm^{-1}).

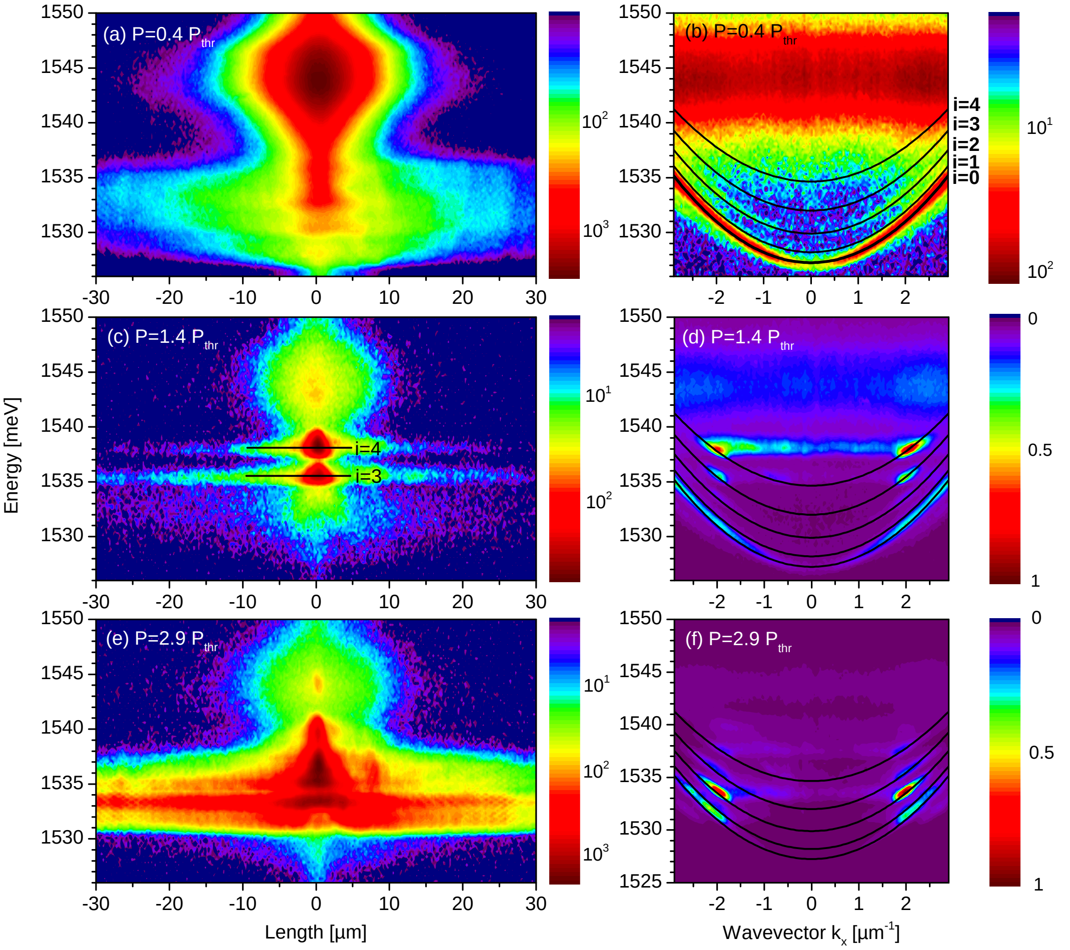

Figure 5-4: Real-space images [(a), (c) and (e)] and Fourier-space images [(b), (d) and (f)] of the photonic wire at different excitation power levels. (a) Even below threshold propagation effects of the LPs, located in the energy range between 1527 − 1537 meV, are observed. The strong emission centered at 1544 meV arises from the QWE. (b) Dispersions of several LP subbranches can be distinguished. Black lines correspond to calculated curves. (c) and (d): Slightly above threshold the main emission originates from the $i = 3$-, and $i = 4$-subbranches. (e) and (f): For further increased excitation power levels the main emission is shifted towards lower LP subbranches. The most intense emission arises at $|k_x| \approx 2\ \mu\mathrm{m}^{-1}$.

For this detection geometry the observed emission in Fourier-space is dominated by the ground mode, due to its symmetric, nodeless mode pattern perpendicular to the wire axis [178, 179]. The strong emission centered at 1544 meV is attributed to the bare uncoupled quantum well exciton (QWE). This QWE photoluminescence is emitted mostly through the edge of the wire. In real-space the confined LP modes show up as several emission peaks below the QWE in the energy range of 1527 − 1537 meV [Fig. 5-4 (a)]. Already below threshold, propagation of the LPs along the wire is observed, which is extended compared to the propagation of the exciton due to the light polariton mass [Fig. 5-4 (a)].

At the threshold power significant changes of the emission patterns occur both in real- [Fig. 5-4 (c)] and in Fourier-space [Fig. 5-4 (d)] because of polariton condensate formation. The polariton condensate emission is most pronounced from the $i = 3$- and

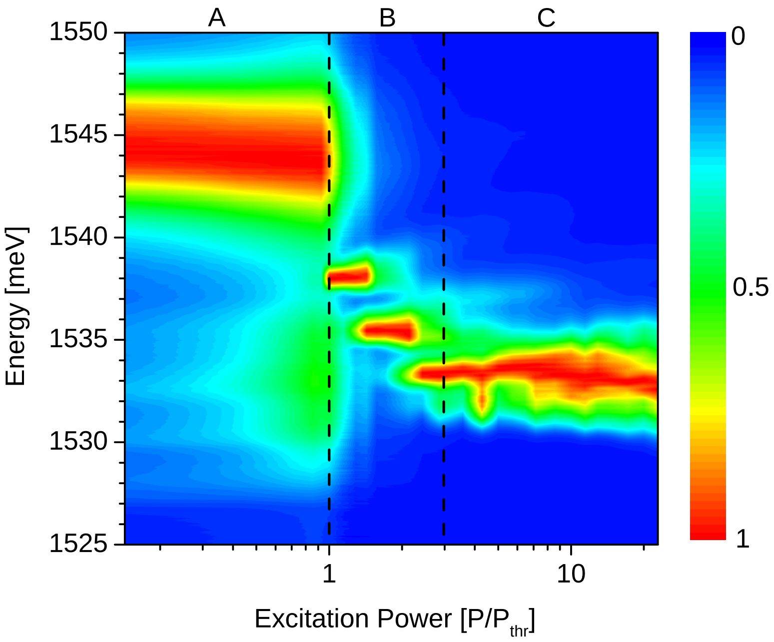

Figure 5-5: Power dependent spectra of the emission from the photonic wire. Three different excitation regimes are indicated by the labels A, B and C. Note: Emission was integrated over the full real-space image and divided by the maximum signal intensity for each excitation power separately.

i = 4-subbranches with the main emission at wavevectors of $|k_x| \approx 2\ \mu\text{m}^{-1}$. This can be attributed to conversion of potential energy mediated by Coulomb interaction with background carriers within the excitation laser spot into kinetic energy [88]. When the excitation power is further increased, the main emission shifts to lower subbranches [Fig. 5-4 (e) and (f)] and the propagation along the photonic wire becomes much more pronounced. As the emission in real-space broadens, a clear distinction especially between the $i = 0$-, $i = 1$- and $i = 2$-LP subbranches in real-space is hardly possible because of the small energy splitting between them.

Fig. 5-5 summarizes the power dependent spectra for increasing excitation power, divided into three different regimes. Below threshold (regime A) the strongest emission comes from the QWE, for intermediate excitation powers in regime B the main emission is shifted from the $i = 4$ LP subbranch to the LP $i = 0$-, $i = 1$- and $i = 2$-subbranches, whereas for high excitation powers clearly above threshold (regime C) the emission energy remains about constant.

As the streak-camera setup possesses a low duty cycle, when recording only single excitation pulses, which is limited to 130 frames per second by the CCD camera [167], a pronounced emission of the mode of interest is required for second-order correlation measurements. Otherwise a reasonable signal to noise ration cannot be provided. Unfortunately, the signal intensity within excitation regime B does not allow for correlation measurements using the streak camera setup. Therefore, a HBT setup is used to perform cross-correlation measurements between polariton condensates of different subbranches in excitation regime B. The temporal resolution of the HBT setup is on the order of 500 ps. Fig. 5-6 shows a typical cross-correlation measurement between two condensate modes at energies of 1532.6 meV and 1534.7 meV, respectively. Clearly, antibunching at

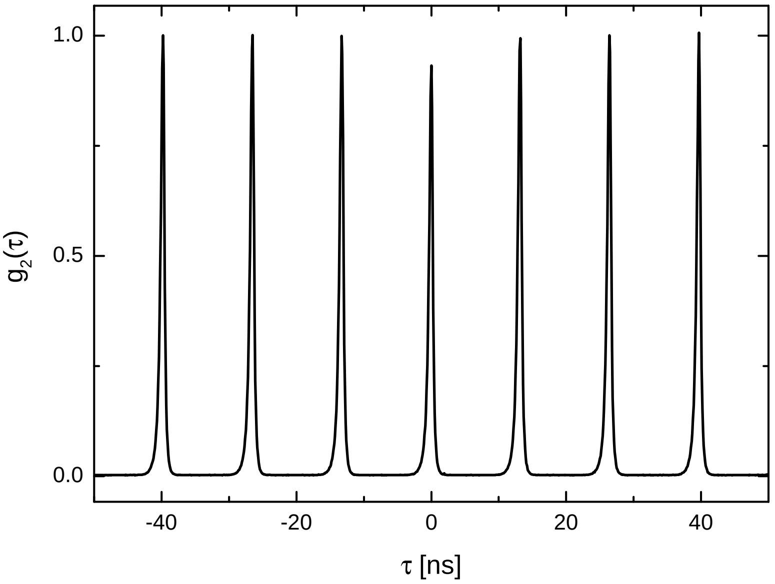

Figure 5-6: Second-order cross-correlation between two polariton condensate modes at energies of 1532.6 meV and 1534.7 meV. Excitation power amounts to $P = 1.8P_{thr}$.

$\tau = 0$ is observed. This indicates mode competition between polariton condensates in different subbranches. A similar antibunching effect was observed in Ref. [180] between two degenerate orbital states in a honeycomb lattice potential, which was attributed to stochastic formation of different polariton condensates.

5.1.4.2 First-order spatial coherence

For spatially resolved investigation of the polariton condensate coherence properties, high excitation power levels within regime C are chosen, where pronounced propagation effects along the wire are observed.

In Fig. 5-7 the dependence of the visibility of the interference pattern on the probed location of the photonic wire is presented for an emission energy of 1532 meV at an excitation power of $P = 14.3P_{thr}$. For $|d| > 10$ µm, far away from the center of the excitation laser spot, the visibility is almost constant and shows the expected monotonous behavior with respect to the slit separation as observed elsewhere [55, 88, 164]: The visibility increases from roughly 0.6 to 0.9 when decreasing the slit separation from $a = 7.5$ µm to $a = 1.25$ µm. However, in the vicinity of the laser spot around $d = 0$ a drastic decrease of the visibility becomes evident for slit separations of $a = 1.25$ µm and $a = 2.5$ µm. The FWHM in both cases is approximately $a = 3.5$ µm, which is on the order of the excitation laser spot size. For the cases of $a = 5$ µm and $a = 7.5$ µm, no pronounced minimum of the visibility at $d = 0$ is observed. Instead, two pronounced minima located symmetrically relative to $d = 0$ are seen. In addition, the distance between the minima matches the slit separation a. Therefore, the observation of the minima corresponds to the situation, where the spatial coherence between polariton condensates located at the excitation laser spot and condensates located at distances of $a = 5$ µm and $a = 7.5$ µm, respectively, away from the excitation spot is probed.

The reduced spatial coherence around the laser spot is tentatively assigned to inter-

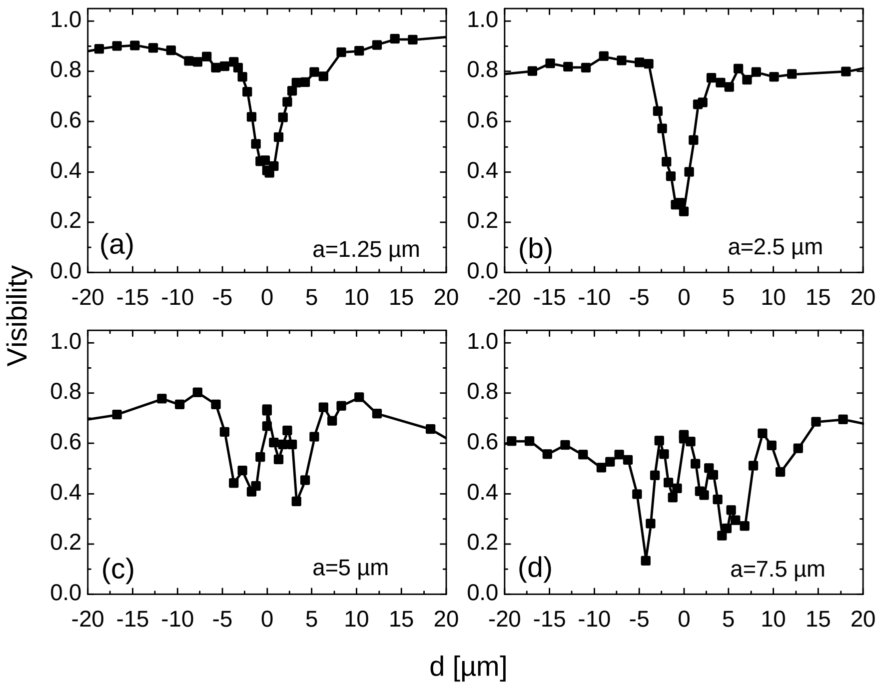

Figure 5-7: Visibility $V(d)$ of the measured interference pattern as function of the location d of the double slit center for different slit separations a. The energy of the emission is centered at 1532 meV, the excitation power is $P = 14.3P_{thr}$. $d = 0$ corresponds to the situation of the double slit placed symmetrically with respect to the excitation laser spot.

action between condensed polaritons and the thermalized reservoir of excitons localized around the excitation laser spot as suggested in Refs. [68, 69]. Recently, there was a claim for observation of the detrimental effect of uncondensed polaritons on the spatial coherence [181]. In this study a 2D polariton condensate was created under the optical parametric oscillation excitation scheme and the spatial coherence between a strictly maintained phase-matching condition and an excitation energy slightly shifted out of phase-matching was compared. In the latter case spatial coherence was found to be decreased, which was attributed to the detrimental effect of uncondensed polaritons on spatial coherence. However, the decrease of coherence in that report might also be explained as a consequence of a lower density of the polariton condensate [182] in the case of phase mismatch of the excitation laser. Here, that explanation can be ruled out, as similar polariton densities at the pump spot and 20 µm away in the real space spectra are observed, whereas the visibility is $V(0\ \mu\text{m}) = 0.4$ at the pump spot and $V(20\ \mu\text{m}) = 0.9$ [Fig. 5-7 (a)] far away from the pump spot.

5.1.4.3 Spatially resolved measurement of second-order temporal correlations

To substantiate the presented interpretation of the results of the double slit experiment, additionally the $g_2(\tau)$-function is measured spatially resolved using the correlation streak-camera technique. To that end, the excitation laser spot is placed at the edge of the photonic wire and the emission of the sample centered at 1530 meV is imaged onto the entrance slit of the streak camera. Under this condition condensate emission occurs at lower wavevectors compared to excitation at the wire center. Thus, the intensity of the

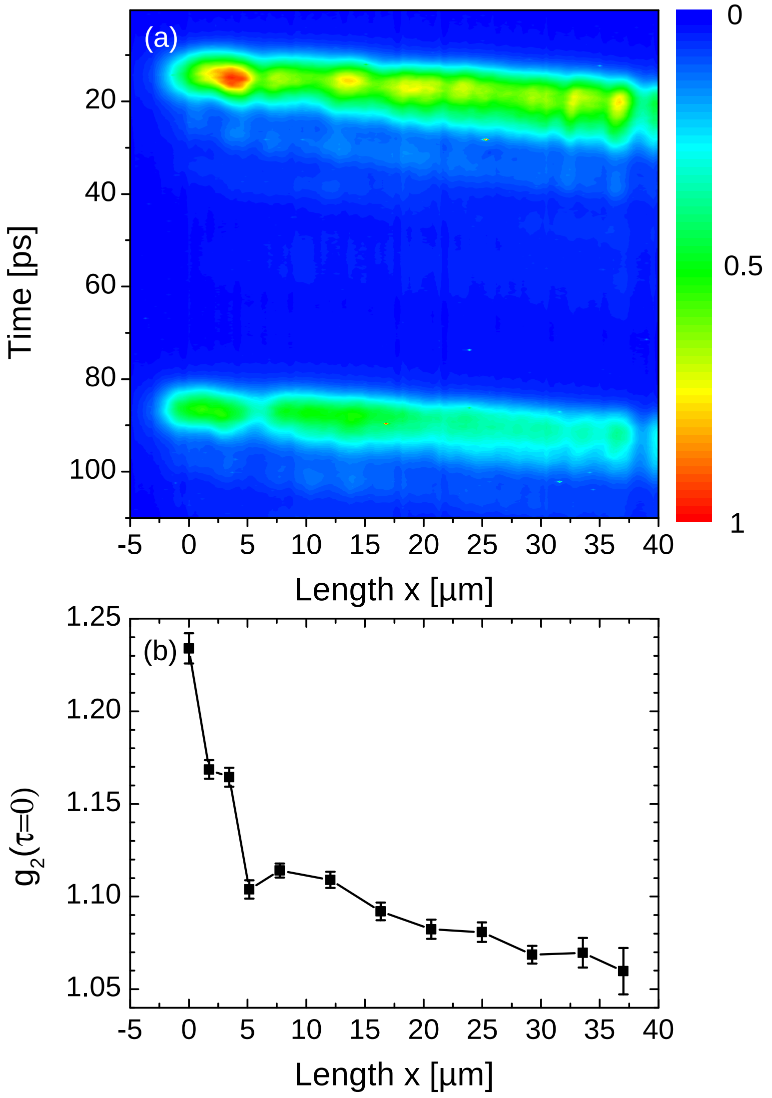

Figure 5-8: (a) Time-resolved spatial distribution of the emission of the condensate centered at 1530 meV. Both profiles arise from the same excitation pulse, but are delayed in time by 72.5 ps due to different optical path lengths (see Sec. 5.1.3 for explanation). The excitation power amounts to $P = 30.4P_{thr}$. (b) Measured $g_2(\tau = 0)$ with respect to the position on the photonic wire.

strongest emission feature is redshifted compared to the power-dependent spectra shown in Fig. 5-5.

In Fig. 5-8 (a) the time-resolved spatial distribution of the polariton condensate is shown. Here, 0 µm indicates the location of the excitation laser spot. Using a beamsplitter, the emission from the photonic wire is imaged onto the entrance slit of the streak camera twice with a relative time delay of 72.5 ps to avoid photon reconstruction errors for $\tau = 0$ as outlined in Sec. 5.1.3. From this image one can deduce a group velocity of 4.5 µm ps^{-1} in accordance with Ref. [69]. Second-order correlations are measured collecting signal from a photonic wire region with 3 µm spatial extent using a vertical slit. Subsequently this region is shifted along the wire. Fig. 5-8 (b) shows the result of these

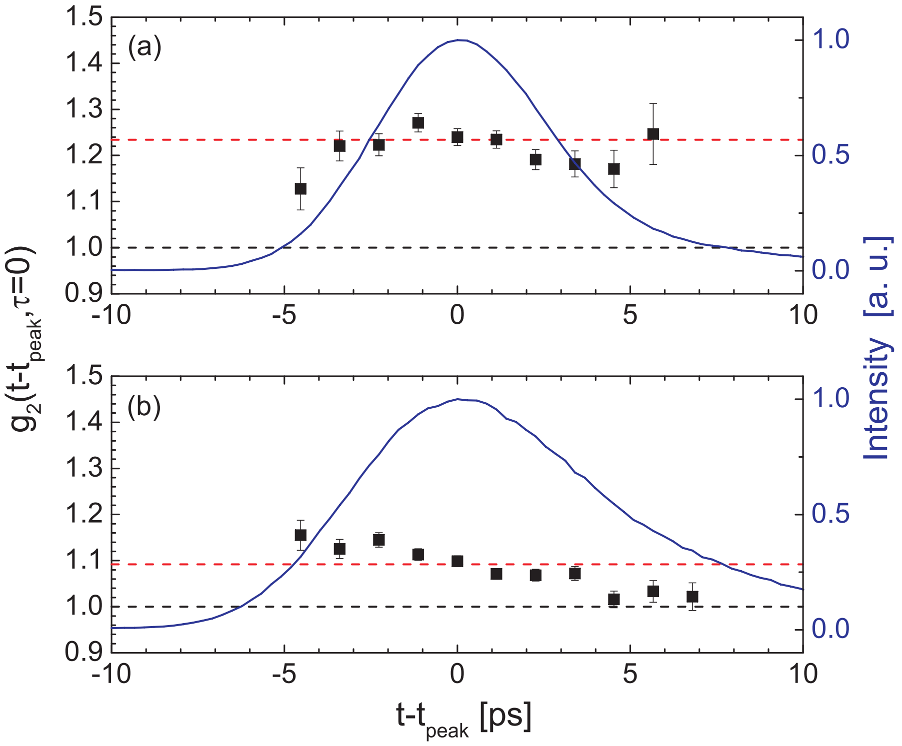

Figure 5-9: Time evolution of the second-order photon-correlation function $g_2(t, \tau = 0)$ (black squares) compared to the normalized output intensity (blue solid line) of the polariton condensate for $x = 0$ µm (a) and $x = 16.3$ µm (b). The red dashed line indicate the time averaged value $g_2(\tau = 0)$ presented in Fig. 5-8, the black dashed line the limiting case for coherent light. Note: Only times t with a sufficient signal-to-noise ratio have been considered for the evaluation of $g_2(t, \tau = 0)$.

spatially resolved measurements of $g_2(\tau = 0)$, the correlation function for simultaneous arrival of two photons.

A bunching of photons emitted from the center of the excitation laser spot can clearly be seen, reflected by values increased above unity, $g_2(\tau = 0) = 1.23$. $g_2(\tau = 0)$ decreases significantly within 5 µm down to $g_2(\tau = 0) = 1.10$. Further on, a slight decrease down to $g_2(\tau = 0) = 1.06$ for a distance of 37 µm from the excitation laser spot is observed. Whereas $g_2(\tau = 0) = 1$ reflects Poissonian distribution and therefore a coherent photon source, increased values of $g_2(\tau = 0)$ indicate a deviation from such a distribution and hence decreased coherence (see Sec. 5.1.2).

The time resolution on the ps timescale of the streak camera system also allows for an evaluation of the equal-time correlation function $g_2(t, \tau = 0)$ at different times within the emission pulse, which provides insights into the coherence dynamics of a non-stationary light field. The $g_2(t, \tau = 0)$-function is analyzed for different positions along the photonic wire (Fig. 5-9). At the location of the excitation laser spot, only small fluctuation around the mean value of $g_2(\tau = 0) = 1.23$ can be observed during the emission pulse of the polariton condensate [Fig. 5-9 (a)]. Interestingly, far away from the excitation laser the situation is different [Fig. 5-9 (b)]: A monotonous decrease of $g_2(\tau = 0)$ towards 1 within the pulse is observed, which demonstrates the recovery of a coherent light emission when no reservoir of background carriers is present. Therefore, this experiment additionally corroborates the interpretation of a decreased coherence of the polariton condensate when background carriers are present.

We also consider the possibility that the high g_2-values observed at the pump spot can be interpreted in terms of simultaneously detected thermal photons. However, an analysis of the input-output curve at the location of the excitation laser spot revealed a ratio of roughly 3 % thermal photons and 97 % photons from the polariton condensate within the duration of roughly 10 ps of the polariton condensate emission [Fig. 5-9 (a)]. Even for the very unlikely case that every detected pair consisting of a thermal/coherent photon would contribute with $g_2(\tau = 0) = 2$, the overall value for $g_2(\tau = 0)$ would be 1.06, which is significantly lower than the average value of $g_2(\tau = 0) = 1.23$ within the emission pulse from the polariton condensate at the position of the excitation laser spot [Fig. 5-9 (a)]. Therefore, one can exclude an explanation of the presented data in terms of thermal photons measured simultaneously.

A similar decrease of second-order coherence induced by interaction with a reservoir was recently observed for a photon BEC [183]. One of the key findings of that report is the observation of increased particle number fluctuations for decreasing condensate fraction with respect to the reservoir (excited dye-molecules in that study). This is identified by an increase of $g_2(\tau = 0)$ up to values of 1.7 for low condensate fractions. The high g_2-values observed are attributed to the grand-canonical ensemble conditions of the experiment at hand when the condensate fraction is low and the particle exchange between the reservoir and the condensate is very effective. A similar effect is seen in this experiment: As the reservoir is mainly located within the excitation laser spot, there is a gradient from low condensate fraction within the laser spot to high condensate fraction several 10 µm away from the excitation laser.

5.1.5 Summary

In conclusion, the detrimental effects of background carriers on the coherence properties of polariton condensates due to interaction between the reservoir and the polariton condensate has been demonstrated using Young's double slit experiment and a second-order correlation measurement. Moreover, a technique to determine spatially resolved second-order correlations has been presented, which should also allow one to measure second-order cross-correlations of polariton condensates at different spatial positions. Furthermore, the operation of the streak-camera as two effective detectors should also enable measurements of correlations between condensates exhibiting different polarizations or energies.

5.2 All-optical flow control of a polariton condensate using non-resonant excitation

5.2.1 Introduction

As has already been outlined in chapter 1, all-optical logic circuits might be promising alternatives to standard CMOS technology regarding heat dissipation and operation speed [8,12]. Furthermore, in principle they allow for the dynamic design of logic circuits by alteration of the applied light fields [184].

An appealing system for the realization of all-optical logic circuits is given by exciton-polaritons in semiconductor microcavities. Especially dissipationless coherent propagation of polariton condensates over hundreds of microns [185], frictionless flow [30] and a propagation speed on the order of 1 % of the speed of light [69] highlight promising features of polariton condensates concerning logic gate operations. Recently, several groups succeeded in establishing a proof of principle polariton-based transistor operation [22,186,187] and in Ref. [22] even more sophisticated features such as cascadability of two transistors and logic gate operation were demonstrated. However, the approaches presented in Refs. [186, 187] require lithographic patterning and are therefore strictly speaking not all-optical circuits. In Ref. [22] a resonant excitation scheme is used, which demands a careful choice of the energy and angle of the excitation laser due to the strict requirements for phase-matching. Beyond that, the number of laser beams impinging on the sample scales with the number of transistors cascaded, which might be a serious drawback for large scale applications.

As an alternative one might consider non-resonant laser excitation for the realization of logic gates based on microcavity polaritons. Here, one has a large degree of freedom regarding the choice of excitation angle and energy. On the other hand, in this case one needs to control the polariton flow direction by means of optically created potentials, in contrast to resonant laser excitation. These potentials are realized under non-resonant pumping by the simultaneous creation of background carriers, from which condensates are repelled. While these potentials were exploited to a large extent for the realization of trapping geometries [25,163,188], only a discretization of the momentum distribution was shown so far for the case of non-trapping geometries [184].

In this section, a directed condensate flow over macroscopic distances on the order of 20 μm using optically generated potentials is demonstrated. Furthermore, by a reconfiguration of the optical potential, the condensate flow can be recaptured as well as steered in arbitrary directions. In addition, the experimental results are confirmed by numerical simulations using a generalized Gross-Pitaevskii equation (GPE).[†] Control over the condensate flow is an important milestone on the way towards a functional circuit architecture based on microcavity polaritons [23,189,190].

5.2.2 Experimental details

A planar GaAs-based microcavity with a Q-factor of about 20000 and a Rabi splitting of 9.5 meV is investigated. Four GaAs quantum wells are placed in the central antinode of the electric field confined by two distributed Bragg reflector (DBR) structures in a $\lambda/2$-cavity. The upper (lower) DBR structure consists of 32 (36) alternating layers of $Al_{0.2}Ga_{0.8}As$ and AlAs. [‡]

Fig. 5-10 schematically shows the experimental setup used for the experiments presented within this section. The sample is mounted in a helium-flow cryostat. Measure-

---

[†] Numerical simulations have been performed by Przemyslaw Lewandowski under supervision of Jun.-Prof. Dr. Stefan Schumacher of the Department of Physics of Paderborn University.

[‡] The investigated sample has been manufactured in the institute of Technical Physics of Würzburg University. The identifier of the sample is M3396-9.2.

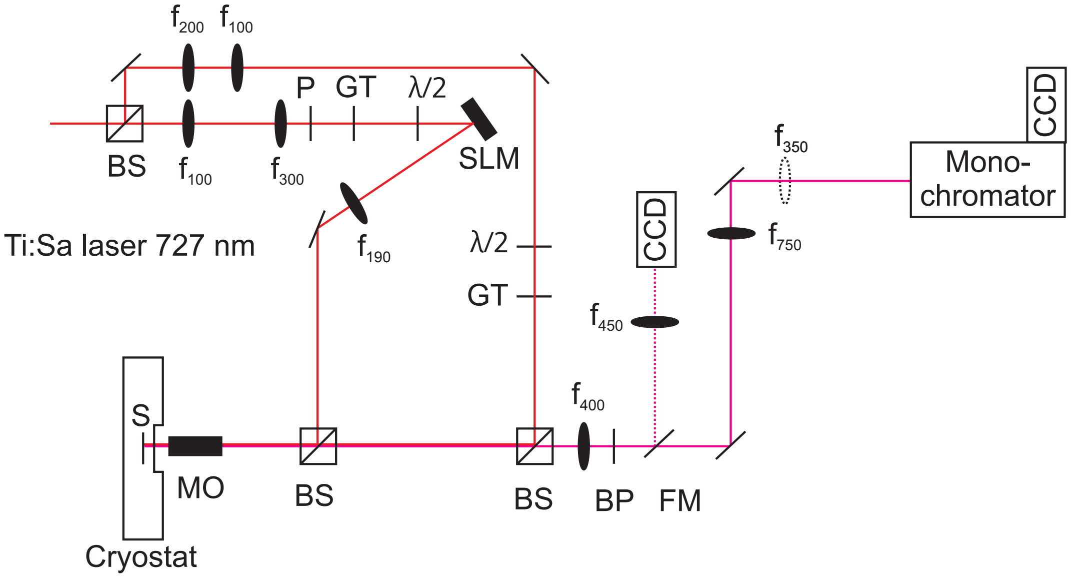

Figure 5-10: Schematic setup for real-space and Fourier-space spectroscopy under excitation with two laser beams: BP, bandpass filter (FWHM 1 nm); BS, beam splitter; CCD, charge coupled device camera; f_{xx}, lens with xx mm focal length; FM, flip mirror; GT, Glan-Taylor prism; $\lambda/2$, half-wave plate; MO, microscope objective (focal length 4 mm, NA 0.42); P, polarizer; S, sample; SLM, spatial light modulator.

ments are performed at 10 K. For non-resonant optical excitation a femtosecond-pulsed Titanium-Sapphire laser (repetition rate 75.39 MHz) with central wavelength at 727 nm (1705 meV) is used. For generation of the optical potentials, the laser beam is divided using a beamsplitter. The first laser beam is collimated using two lenses of 200 mm and 100 mm focal length and the excitation power is varied by rotating a half-wave plate in front of a Glan-Taylor prism. The shape of the first beam is Gaussian with a full width at half maximum (FWHM) of 2 µm on the sample. The diameter of the second beam is expanded by two lenses of 100 mm and 300 mm focal length in order to achieve a complete illumination of the liquid crystal display of a phase-only spatial light modulator (SLM). A polarizer and Glan-Taylor prism allow for a regulation of the excitation power. A half-wave plate placed behind the Glan-Taylor prism sets the polarization of the excitation laser such that the contrast of the modulated shape of the laser beam is maximized. The Fourier-transform of the desired real space shape of the laser spot at the sample, e.g. a circle or a semicircle, is imposed on the liquid crystal display of the SLM. Superimposing the Fourier-transform of the phase function of a collecting lens on the SLM in combination with an additional lens (focal length $f = 190$ mm) allows for the downscaling of the beam diameter in order to match the diameter of the laser beam with the size of the entrance pupil of the microscope objective (numerical aperture 0.42). The time delay between the beams is less than 2 ps. For detection a liquid nitrogen-cooled CCD-camera placed behind a monochromator is used. For two-dimensional imaging in real space and Fourier-space, respectively, the monochromator is operated in zeroth order. In that case, the spectral resolution is provided by a bandpass filter with a FWHM of 1 nm. All experiments are performed at an exciton-cavity detuning of -21.7 meV, which corresponds to a photonic fraction of 96 % of the lower polariton (LP) at zero in-plane wavevector.

5.2.3 Results and discussion

Fig. 5-11 (a) shows a typical dispersion for an excitation power level P several times higher than the threshold power P_{thr} for polariton condensation, when only the Gaussian laser spot is used. Clearly, the main emission at wavevectors of $|k_y| \approx 1.8\ \mu\mathrm{m}^{-1}$ occurs blueshifted by 3 meV with respect to the lowest energy state of the LP at zero in-plane wavevector. The observed blueshift arises from repulsive interactions between the condensed polaritons and background carriers created by non-resonant pumping and from polariton-polariton interactions. These mechanisms generate an antitrapping potential and cause ballistic acceleration of the condensed polaritons away from the background carrier reservoir [143]. This finding is further elucidated by the corresponding real space spectrum, where a pronounced ballistic propagation over a distance of several 10 μm can be seen [Fig. 5-11 (b)]. However, as a two-dimensional polariton system is investigated here, this propagation occurs omnidirectional, radially symmetric with respect to the Gaussian excitation laser spot.

As a first step towards controlling the spread of the condensate, the condensate can be trapped by applying a ring shaped laser spot, approximately 10 μm in diameter, centrosymmetric around the Gaussian spot using the second laser beam modulated by the SLM. A typical excitation profile for this situation is depicted in Fig. 5-12 (a). The condensate excited by this laser pattern is trapped due to the repulsive interaction with background carriers located at the position of the laser pattern. Fig. 5-11 (c) shows a spectrally resolved cross-section in L_y direction, where $L_y = 0$ μm indicates the position of the Gaussian laser spot. In this case the main emission is centered at 1602 meV, 3 meV lower in energy compared to the case of excitation with the Gaussian laser spot only. For the further experiments a spectral region of 1 meV width is selected using an interference filter, covering wavevectors $|k_{||}| < 1.3\ \mu\mathrm{m}^{-1}$ only, which is indicated by the red rectangle in Fig. 5-11 (a). In Fig. 5-12 (b) the trapped condensate can be seen, which builds up in a donut shape due to the centrosymmetric shape of the applied optical potential [Fig. 5-12 (a)]. Furthermore, the wavevector distribution is centered around zero momentum, as expected for a trapped condensate [Fig. 5-12 (c)].

In order to understand the interaction between the optically created potentials and the condensates better, numerical simulations have been performed. To this end, a mean-field description of the coherent polariton field coupled to two incoherent background carrier/exciton reservoirs, which consist of an active and an inactive reservoir, is used [72, 191]. The addition of an inactive reservoir reflects the relaxation process from a hot electron-hole plasma created by the non-resonant pumping process towards an active exciton reservoir as described in Sec. 4.1.1, which feeds the coherent polariton field through stimulated scattering. Consequently, the theoretical description is based on the coupled spatio-temporal dynamics of (a) the coherent polariton field/condensate Ψ, (b) an active exciton reservoir n_A feeding the condensate through a stimulated scattering process, and (c) an inactive reservoir n_I created in the optical pumping process and feeding the active reservoir. The equations of motion read as follows:

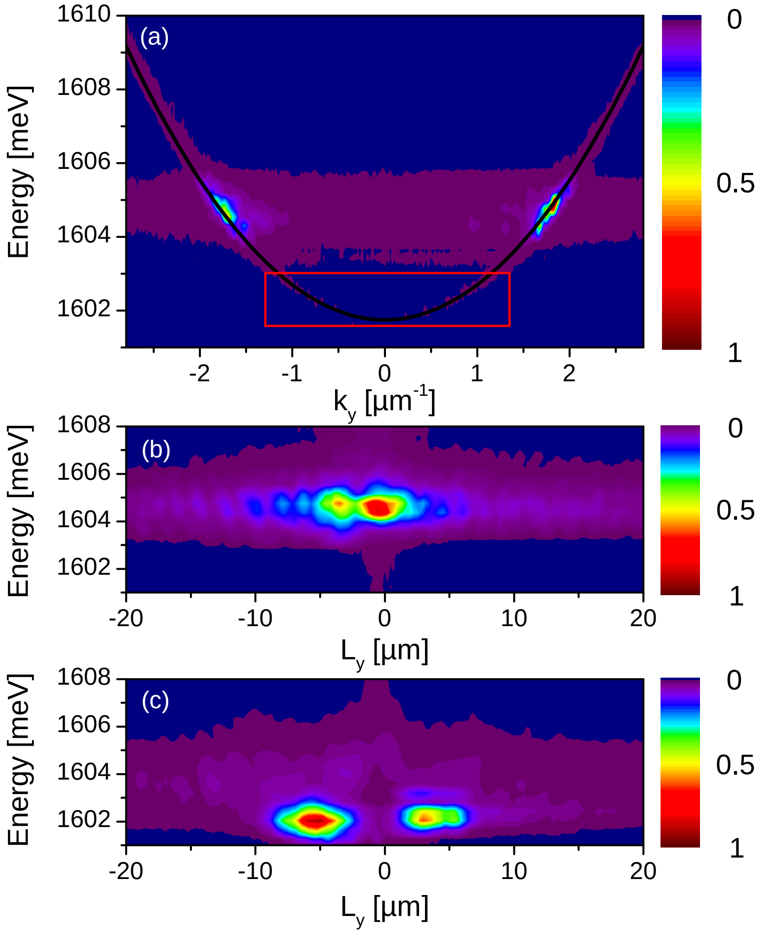

Figure 5-11: (a) Fourier-space image for an excitation power level $P = 8P_{\mathrm{thr}}$ under excitation with the Gaussian laser spot only. The red rectangle indicates the selected spectral region for the experiments operating the monochromator in zeroth order. (b) Corresponding real-space image for $P = 8P_{\mathrm{thr}}$. (c) Real-space image of the condensate emission for the excitation profile presented in Fig. 5-12 (a). The excitation power levels for the Gaussian spot and for the circle shaped pattern are $P = 18P_{\mathrm{thr}}$ and $P = 6.5P_{\mathrm{thr}}$, respectively. Threshold power levels are determined by exciting either with the Gaussian spot or the circle shaped pattern only.

$$i\hbar\dot{\Psi} = \left(\mathbb{H} - \mathrm{i}(\gamma_p - \frac{\gamma}{2}n_A) + V_d\right)\Psi \tag{5.7}$$

$$+ \left(\alpha_1 \mid \Psi \mid^2 + \alpha_2 n_A + \alpha_3 n_I\right)\Psi - i\Lambda(n_A + n_I)\mathbb{H}\Psi,$$

$$\dot{n}_A = \frac{1}{\hbar}\left(\tau n_I - \gamma_A n_A - \gamma \mid \Psi \mid^2 n_A\right), \tag{5.8}$$

$$\dot{n}_I = \frac{1}{\hbar}\left(-\tau n_I - \gamma_I n_I\right). \tag{5.9}$$

Ψ, n_A and n_I are defined in the two-dimensional x, y-plane. Eq. (5.7) captures the dynamics of the coherent polariton field and is based on the GPE (2.53), which is derived in Sec. 2.4.3. Here, $\mathbb{H} = -\frac{\hbar^2}{2m_p}\Delta$ accounts for the free propagation of polaritons with effective mass $m_p = 0.35 \cdot 10^{-4}\, m_e$. The polariton field Ψ is replenished by the active reservoir with $\gamma = 0.004$ meV µm^2. Disorder effects (see Sec. 2.4.5) are considered by implementation of a disorder potential V_d with a spatial correlation length of 1 µm and

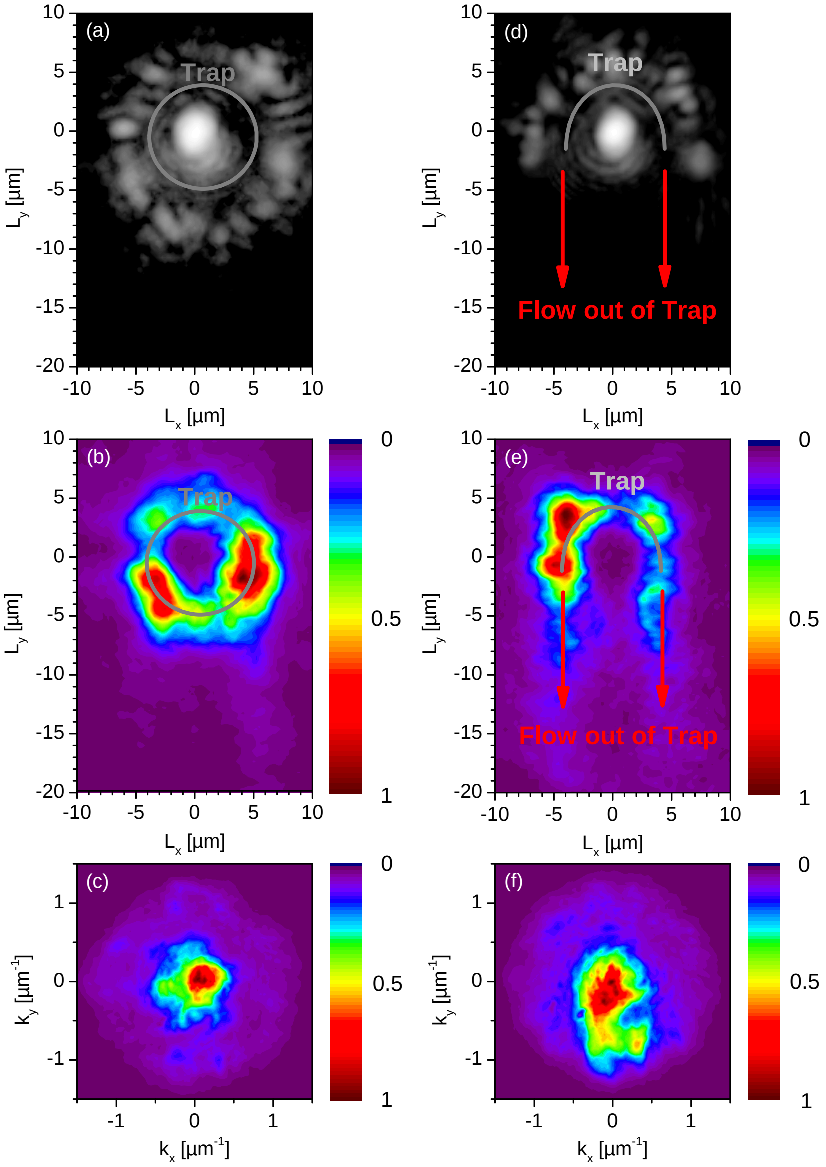

Figure 5-12: (a) Laser excitation pattern for the trapping geometry. The excitation power levels are $P = 18P_{\mathrm{thr}}$ for the Gaussian spot and $P = 6.5P_{\mathrm{thr}}$ for the circle shaped pattern. (b) Two-dimensional real-space image of the trapped condensate. (c) Corresponding Fourier-space image of the trapped condensate. (d) Laser excitation pattern for the source of directed condensate flow. The excitation power levels are $P = 18P_{\mathrm{thr}}$ for the Gaussian spot and $P = 11.3P_{\mathrm{thr}}$ for the semicircle shaped pattern. (e) Two-dimensional real-space image of the trapped condensate and the directed condensate flow escaping from the trap. (f) Corresponding Fourier-space image for the situation of panel (e).

a root mean square (rms) amplitude of 0.2 meV. A repulsive Coulomb interaction is given by $\alpha_1 = 0.0024$ meVµm^2 (Refs. [70,72,192]) for interaction between polaritons and by $\alpha_2 = \alpha_3 = 0.008$ meVµm^2 for the polariton-reservoir interaction. The last term in Eq. (5.7) with $\Lambda = 0.00025$ µm^{-2} mimics a relaxation term as it drives the polariton system to on average lower kinetic energies in spatial regions where interaction with the reservoir densities n_A and n_I occurs [69]. Spin degrees of freedom [193] are not considered here. Eqs. (5.8)-(5.9) describe the dynamics of the active and inactive reservoir,

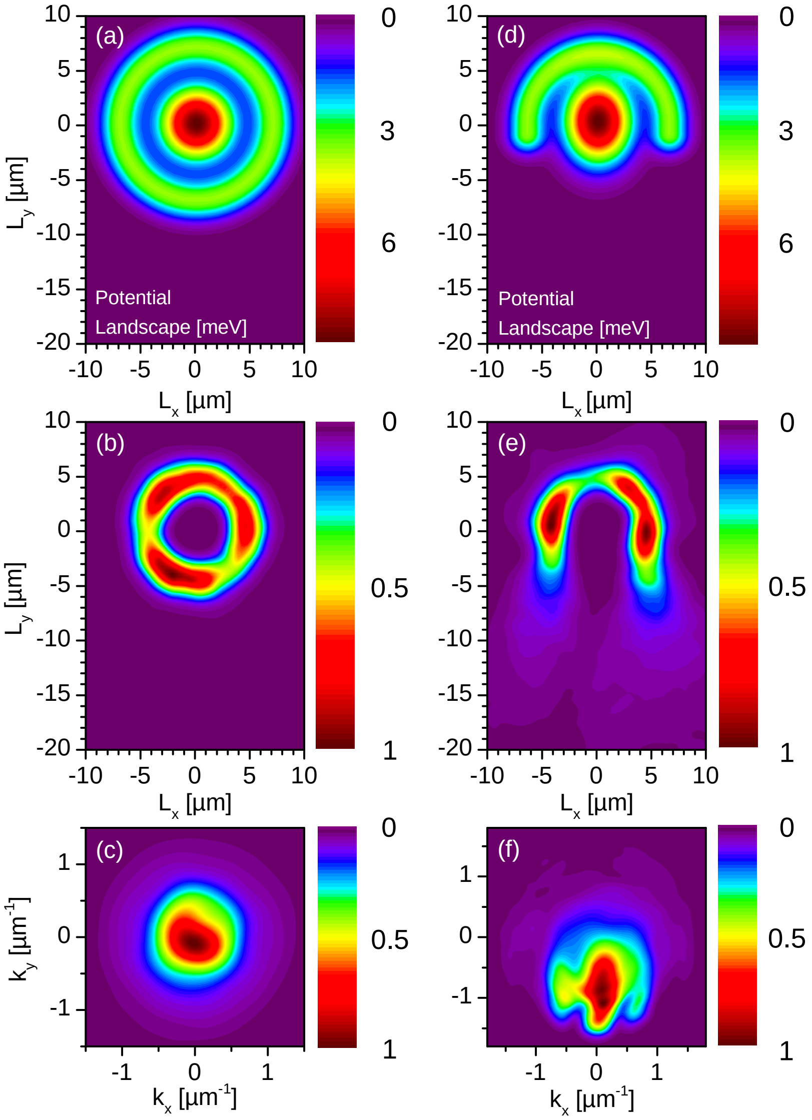

Figure 5-13: Applied potential landscape for the simulation of the trapping geometry (a) and of the source of the directed condensate flow (d). Corresponding time-integrated calculated condensate distribution in real-space [(b) and (e)] and in k-space [(c) and (f)]. Numerical data have been provided by Przemyslaw Lewandowski.

respectively. In Eqs. (5.8)-(5.9), the active reservoir is fed by the inactive reservoir with $\tau = 0.1$ meV. Radiative losses are $\gamma_p = 0.1$ meV, $\gamma_A = 0.01$ meV (Ref. [194]) and $\gamma_I = 0.0013$ meV (Ref. [72]) for Ψ, n_A and n_I, respectively.

In the simulations, Eqs. (5.7)-(5.9) are solved on a two-dimensional grid in real space. Initially, the active reservoir density n_A is set to zero. A small complex-valued random field is assumed for the coherent polariton field Ψ to trigger the stimulated feeding after optical excitation. This initial random field has a spatial correlation length of 1 μm and a rms amplitude of 10^7 cm^{-2} and differs for each of the 30 runs performed for the simulations. The optical excitation profile is included in the initial condition for the inactive reservoir density n_I (experimentally, excitation is far above the gap on a fast 100 fs timescale). The maximum initial reservoir density is $\max(n_I) = 1.1 \cdot 10^{11}$ cm^{-2}.

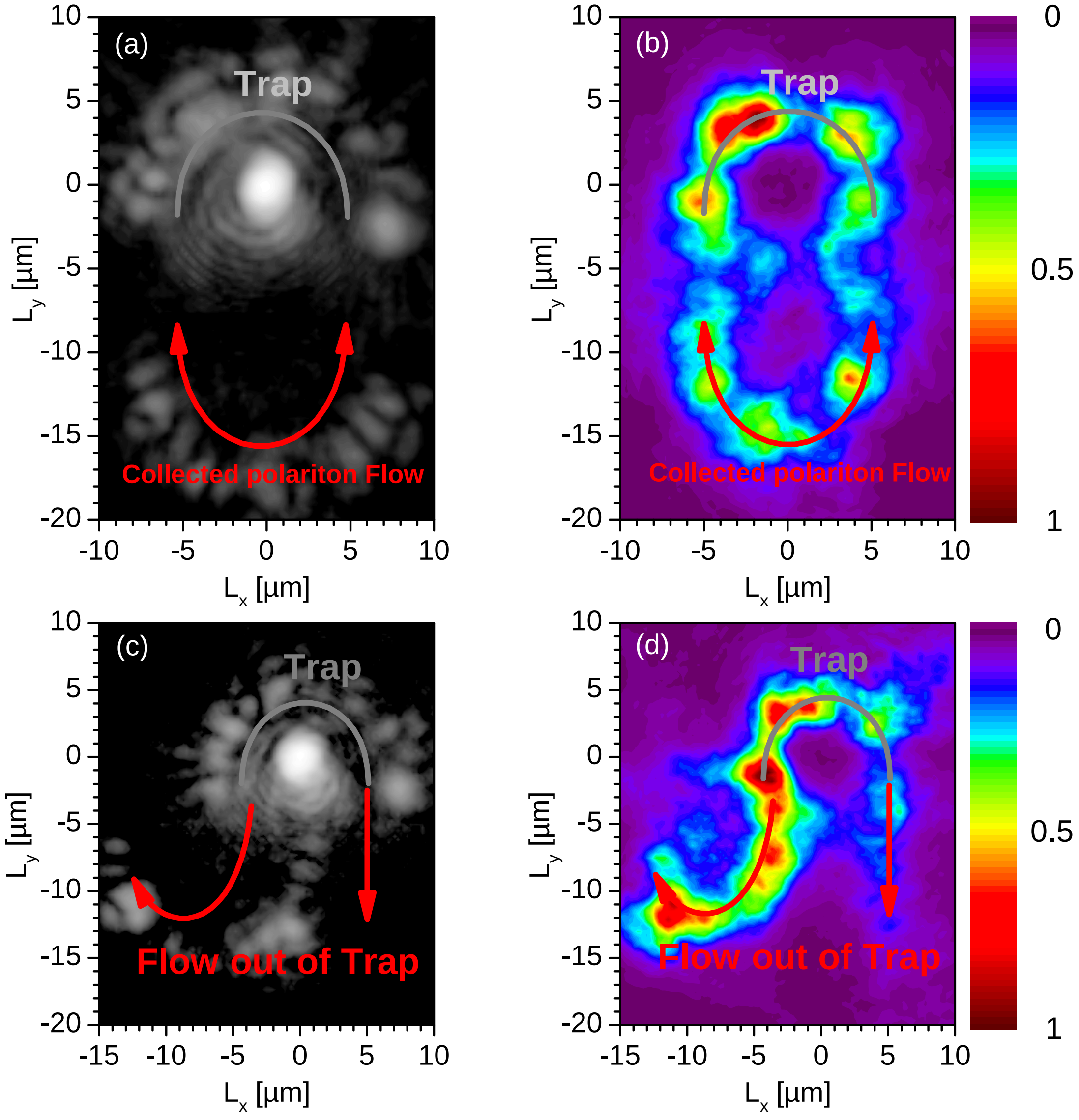

Figure 5-14: (a) Laser excitation pattern for the collector geometry. The excitation power levels are $P = 18P_{\text{thr}}$ for the Gaussian spot and $P = 5.9P_{\text{thr}}$ for the SLM generated pattern. (b) Two-dimensional real-space image of the recollected condensate. (c) Laser excitation pattern for bending the condensate flow. The excitation power levels are $P = 18P_{\text{thr}}$ for the Gaussian spot and $P = 6.2P_{\text{thr}}$ for the SLM generated pattern. (d) Two-dimensional real-space image of the curve-shaped condensate.

Using a centrosymmetric shaped potential landscape [Fig. 5-13 (a)], the condensate is trapped with $\mathbf{k} \approx 0$ [Fig. 5-13 (b) and (c)], in accordance with the experimental observations [Fig. 5-12 (b) and (c)]. To exploit this trapping geometry for the generation of a directed condensate flow, the trap is opened by applying a semicircle shaped potential instead of a full circle [Fig. 5-12 (d)], the corresponding potential landscape used for the simulations is presented in [Fig. 5-13 (d)]. Once a condensate builds up inside the cavity, the polariton condensate can leave the trap by flowing through the aperture at the bottom in L_y direction [Fig. 5-12 (e)]. Due to the repulsive interaction with the reservoir

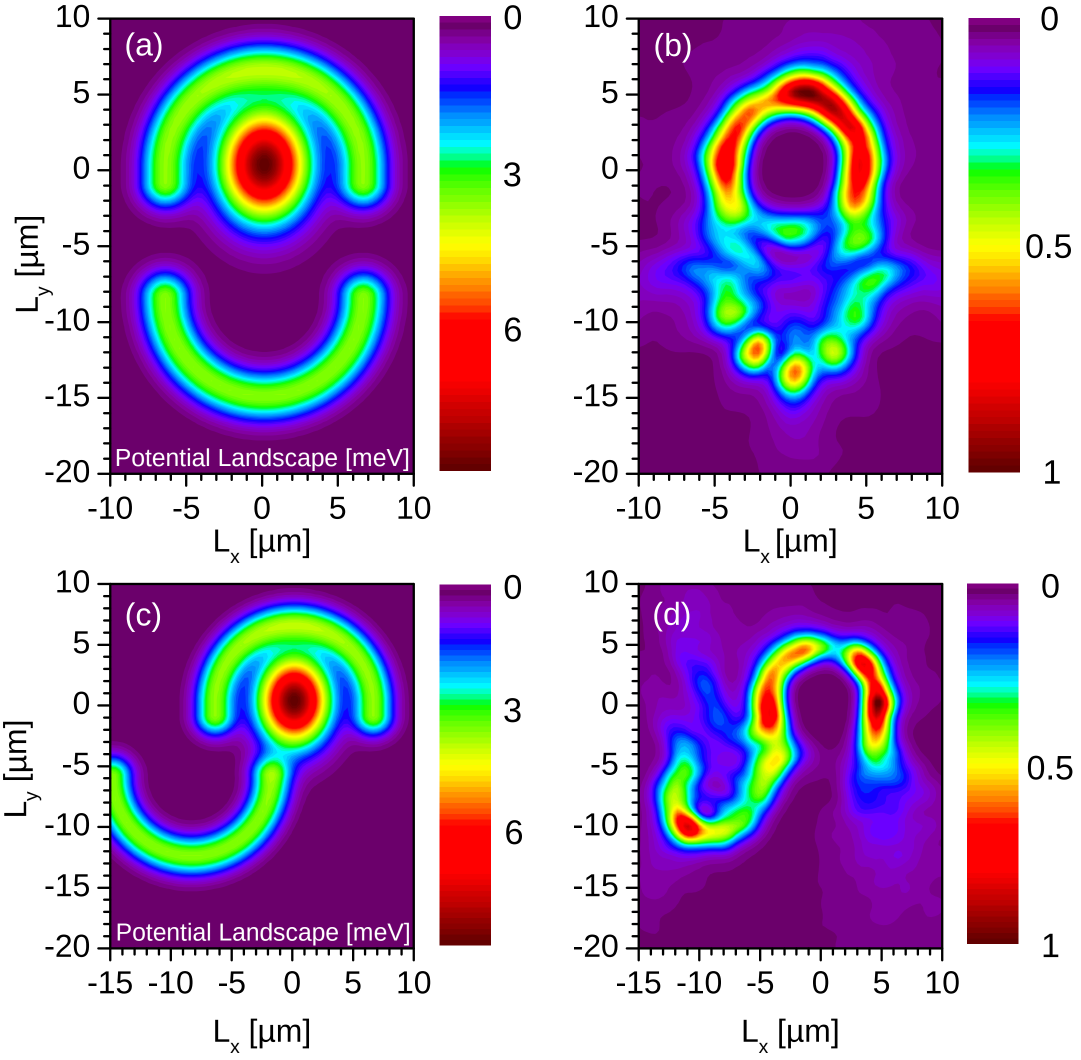

Figure 5-15: Applied potential landscape for the simulation of the collector geometry (a) and of the bending of the condensate flow (c). Corresponding time-integrated calculated condensate distribution in real-space [(c) and (d)]. Numerical data have been provided by Przemyslaw Lewandowski.

excitons, polaritons are accelerated away from the excitation point such that a directed polariton flow from the trap is clearly visible in the experiment [Fig. 5-12 (e)] as well as in the numerical simulations [Fig. 5-13 (e)]. This pronounced directed propagation is also evident in Fourier-space, where the wavevector distribution is significantly relocated towards negative values of k_y [Fig. 5-12 (f) and Fig. 5-13 (f)] in contrast to the situation of the closed trap [Fig. 5-12 (c) and Fig. 5-13 (c)]. Therefore this geometry acts as a source for a directed condensate flow. Once a directed flow is realized, one can further steer and manipulate this directed condensate arbitrarily by modifying the potential landscape. In the following, two scenarios are exemplarily demonstrated. By applying an additional semicircle shaped laser pattern in roughly 10 µm distance from the source [Fig. 5-14 (a)], the condensate flow is recollected and transferred to an oval shaped standing wave pattern [Fig. 5-14 (b)] as a consequence of reflection, amplification and interference, which is reproduced well by the simulations [Fig. 5-15 (a) and (b)]. Furthermore, if an opposing semicircle shaped potential with respect to the source is applied [Fig. 5-14 (c)], one can generate a curve shaped condensate flow [Fig. 5-14 (d)], which is consistent with calculations [Fig. 5-15 (c) and Fig. 5-15 (d)]. In both scenarios the optically created potential interacts twofold with the incoming condensate: Firstly the incoming flow is redirected due to repulsive Coulomb interaction with the background carriers, and secondly the potential barrier operates also as a gain medium, which gives rise to strong condensate emission in up to 15 µm distance from the source of the directed condensate flow. Nevertheless, the barrier remains separated in space from the condensate flow, which might be beneficial concerning the loss of coherence of a condensate mediated by the local presence of background carriers (see Sec. 5.1).

5.2.4 Summary

In conclusion of this section, the control of the polariton flow using reconfigurable optically induced potentials has been demonstrated. Firstly, a feasible approach for the generation of directed condensate propagation has been presented. Furthermore, a manipulation of this flow, e.g. a recollection of the condensate and a guiding on a curve shaped trajectory, has been demonstrated. In addition, the experimental results have been reproduced in terms of a generalized GPE. The control of the condensate flow is a prerequisite for further, more sophisticated investigations, e.g. scattering experiments of polariton condensates, and might pave the way towards all-optical logic circuits using microcavity polaritons.

Chapter 6

Conclusions and outlook

In conclusion, this thesis provides new insights into the optical properties of bulk polaritons as well as polaritons in microcavities. The results of the experiments performed presented in chapters 3-5 give a contribution to the fundamental understanding of polaritons, but are also of relevance to evaluate the potential of applications, such as different types of GaAs-based polariton lasing devices, and might be pertinent for a possible realization of all-optical logic circuits based on polaritons.

From a fundamental research point of view, the results presented in chapter 3 offer interesting findings concerning the polariton propagation in bulk material. By a new nonlinear spectroscopic approach using two single-frequency lasers, the hardly investigated blue exciton-polariton in Cu_2O was accessed by sum-frequency generation. Most notably, the experiment showed signatures of coherent propagation without damping in a spectral region of high absorption. The experimental observations can be interpreted in terms of a fusion process of two beams of coherent polaritons exhibiting a large difference in group velocity. However, a full theoretical understanding of the coherent propagation of polaritons in a highly absorbing material is still lacking. Nevertheless the presented results should stimulate theoretical work on nonlinear excitation of polaritons.

The investigations presented in chapter 4 aimed at the identification of a suitable parameter space for operation of a GaAs-based polariton laser and the evaluation of a concept for THz-lasing operation based on polaritons in microcavities, which was suggested recently [31]. In the first part of this chapter an upper limit of the lattice temperature of 90 K for polariton lasing operation was identified and the requirement for a large Q factor of the microcavity to achieve polariton lasing operation in the negative detuning range was determined. Therefore, polariton lasing operation in GaAs-based microcavities at liquid nitrogen temperatures might be in reach. However, the adequacy for applications beyond fundamental research is currently hard to estimate. Nevertheless, the excellent crystal quality of available GaAs-based microcavity samples provides ideal circumstances for investigations on polariton condensates. Subsequently, the knowledge of GaAs-based materials can be transfered to material systems with larger exciton binding energies, such as GaN, ZnO and organic semiconductors allowing for room temperature operation of polariton lasers. Concerning THz lasing operation based on a two-photon pumping process of the $2p$ exciton, the results of two-photon excitation (TPE) spectroscopy indicated that a realization of such a device will probably be very challenging in GaAs-based microcavities. In detail, no significant resonance of the $2p$ exciton could be identified in the

TPE spectra, which suggests an inefficient two-photon pumping process. Nevertheless, the performed nonlinear spectroscopic study of a GaAs-based microcavity revealed other interesting two-photon processes such as second-harmonic generation arising from the LP and UP polaritons as well as from the DBR reflection minima, which might stimulate further nonlinear spectroscopic investigations of microcavity systems.

High Q factors larger than 10000 in GaAs-based microcavities allowed for the observation of polariton condensates propagating over macroscopic distances of several 10 µm. The evaluation of the coherence properties of the propagating condensates as well as the steering of the condensate flow was in the focus of chapter 5. In this connection, an increase of first-order as well as second-order coherence was observed, when the condensate propagated out of the excitation laser spot. This was attributed to the presence of background carriers under non-resonant excitation, which interact with the polariton condensate. Moreover, the measurement scheme using the streak camera in a Hanbury-Brown-Twiss-like configuration, which was demonstrated in this thesis, offers the possibility to determine second-order cross-correlation functions between condensates of different polarizations as well as energetically different polariton condensates on a picosecond timescale in future experiments. Finally, it was shown that the flow of the condensate can be steered and manipulated at will by means of optically generated potentials without the need for a resonant excitation scheme. This finding might be appealing for the realization of all-optical logic circuits, and moreover it enables scattering experiments in the solid state with a well-defined observable trajectory of particles.

Natural constants and abbreviations

acronym	**meaning**
AC	acoustical
BEC	Bose-Einstein condensate
BKT	Berezinskii-Kosterlitz-Thouless
c	speed of light (299792458 m/s)
CCD	charge-coupled device
CL	cavity lasing
CMOS	complementary metal-oxide-semiconductor
CW	continuous wave
DBR	distributed Bragg reflector
e-h	electron-hole
EM	electro-magnetic
eV	electron volt (1.602176 $\cdot 10^{-19}$ J)
FWHM	full width at half maximum
GMR	giant magnetoresistance
GPE	Gross-Pitaevskii equation
$\hbar$	$h/2\pi$= 1.054571$\cdot$ 10^{-34} J s= 6.582118$\cdot$ 10^{-16} eV s
HBT	Hanbury-Brown-Twiss
hh	heavy-hole
I-O	input-output
k_B	Boltzmann constant ($1.38065\cdot10^{-23} JK^{-1}$)
LO	longitudinal optical
LP	lower polariton
m_e	free electron mass ($9.109383 \cdot 10^{-31}$ kg)
meV	milli-electron volt

µm	micrometer
mW	milliwatt
MWH	Mermin-Wagner-Hohenberg
NA	numerical aperture
Nd:YAG	yttrium aluminum garnet doped with neodymium
nm	nanometer
OPO	optical-parametric-oscillator
PL	photoluminescence
ps	picosecond
Q	quality factor
QWE	quantum well exciton
rhs	right hand side
rms	root mean square
SF	sum-frequency
SFG	sum-frequency generation
SHG	second harmonic generation
SLM	spatial light modulator
THz	terahertz
Ti:Sa	Titanium-Sapphire
TPA	two-photon absorption
TPE	two-photon excitation
UP	upper polariton
W	Watt

Bibliography

[1] M. N. Baibich, J. M. Broto, A. Fert, F. Nguyen Van Dau, F. Petroff, P. Etienne, G. Creuzet, A. Friederich, J. Chazelas, Phys. Rev. Lett. **61**, 2472 (1988).

[2] G. Binasch, P. Grünberg, F. Saurenbach, W. Zinn, Phys. Rev. B **39**, 4828 (1989).

[3] G. A. Prinz, Science **282**, 1660 (1998).

[4] International technology roadmap for semiconductors (2012).

[5] D. H. Kim, K. Athikulwongse, M. Healy, M. Hossain, M. Jung, I. Khorosh, G. Kumar, L. Young-Joon, D. Lewis, T.-W. Lin, Ch. Liu, S. Panth, M. Pathak, M. Ren, G. Shen, T. Song, D. H. Woo, X. Zhao, J. Kim, H. Choi, G. Loh, H.-H. Lee, S. K. Lim, in *Solid-State Circuits Conference Digest of Technical Papers (ISSCC), 2012 IEEE International*, 188–190 (2012).

[6] S. Datta, B. Das, Applied Physics Letters **56**, 665 (1990).

[7] M. I. Dyakonov in *Future Trends in Microelectronics. Frontiers and Innovations*, A. Zaslavsky, S. Luryi, J. Xu, (eds.), 266–285 (Wiley, 2013).

[8] H. J. Caulfield, S. Dolev, Nat. Photon. **4**, 261 (2010).

[9] D. A. B. Miller, Nat. Photon. **4**, 3 (2010).

[10] D. A. B. Miller, Nat. Photon. **4**, 406 (2010).

[11] R. S. Tucker, Nat. Photon. **4**, 405 (2010).

[12] D. Snoke, Nat. Nano. **8**, 393 (2013).

[13] K. Huang, Proc. Roy. Soc. A **208**, 352 (1951).

[14] U. Fano, Phys. Rev. **103**, 1202 (1956).

[15] J. J. Hopfield, Phys. Rev. **112**, 1555 (1958).

[16] V. M. Agranovich, Sov. Phys. JETP **37**, 307 (1960).

[17] C. Weisbuch, M. Nishioka, A. Ishikawa, Y. Arakawa, Phys. Rev. Lett. **69**, 3314 (1992).

[18] Ch. Schneider, A. Rahimi-Iman, N. Y. Kim, J. Fischer, I. G. Savenko, M. Amthor, M. Lermer, A. Wolf, L. Worschech, V. D. Kulakovskii, I. A. Shelykh, M. Kamp, S. Reitzenstein, A. Forchel, Y. Yamamoto, S. Höfling, Nature **497**, 348 (2013).

[19] P. Bhattacharya, B. Xiao, A. Das, S. Bhowmick, J. Heo, Phys. Rev. Lett. **110**, 206403 (2013).

[20] P. Bhattacharya, T. Frost, S. Deshpande, M. Z. Baten, A. Hazari, A. Das, Phys. Rev. Lett. **112**, 236802 (2014).

[21] A. Imamoglu, R. J. Ram, S. Pau, Y. Yamamoto, Phys. Rev. A **53**, 4250 (1996).

[22] D. Ballarini, M. De Giorgi, E. Cancellieri, R. Houdrë, E. Giacobino, R. Cingolani, A. Bramati, G. Gigli, D. Sanvitto, Nat. Commun. **4**, 1778 (2013).

[23] R. W. Keyes, Science **230**, 138 (1985).

[24] J. Kasprzak, M. Richard, S. Kundermann, A. Baas, P. Jeambrun, J. M. J. Keeling, F. M. Marchetti, M. H. Szymanska, R. Andre, J. L. Staehli, V. Savona, P. B. Littlewood, B. Deveaud, Le Si Dang, Nature **443**, 409 (2006).

[25] G. Tosi, G. Christmann, N. G. Berloff, P. Tsotsis, T. Gao, Z. Hatzopoulos, P. G. Savvidis, J. J. Baumberg, Nat. Phys. **8**, 190 (2012).

[26] M. Abbarchi, A. Amo, V. G. Sala, D. D. Solnyshkov, H. Flayac, L. Ferrier, I. Sagnes, E. Galopin, A. Lemaître, G. Malpuech, J. Bloch, Nat. Phys. **9**, 275 (2013).

[27] K. G. Lagoudakis, M. Wouters, M. Richard, A. Baas, I. Carusotto, R. Andre, Le Si. Dang, B. Deveaud-Plédran, Nat. Phys. **4**, 706 (2008).

[28] K. G. Lagoudakis, T. Ostatnický, A. V. Kavokin, Y. G. Rubo, R. André, B. Deveaud-Plédran, Science **326**, 974 (2009).

[29] A. Amo, D. Sanvitto, F. P. Laussy, D. Ballarini, E. del Valle, M. D. Martin, A. Lemaître, J. Bloch, D. N. Krizhanovskii, M. S. Skolnick, C. Tejedor, L. Viña, Nature **457**, 291 (2009).

[30] A. Amo, J. Lefrere, S. Pigeon, C. Adrados, C. Ciuti, I. Carusotto, R. Houdré, E. Giacobino, A. Bramati, Nat. Phys. **5**, 805 (2009).

[31] A. V. Kavokin, I. A. Shelykh, T. Taylor, M. M. Glazov, Phys. Rev. Lett. **108**, 197401 (2012).

[32] E. T. Jaynes, F. W. Cummings, Proceedings of the IEEE **51**, 89 (1963).

[33] D. D. Sell, Phys. Rev. B **6**, 3750 (1972).

[34] H. Matsumoto, K. Saito, M. Hasuo, S. Kono, N. Nagasawa, Solid State Communications **97**, 125 (1996).

[35] G. M. Kavoulakis, Y.-Ch. Chang, G. Baym, Phys. Rev. B **55**, 7593 (1997)

[36] A. Quattropani, L.C. Andreani, F. Bassani, Il Nuovo Cimento D **7**, 55 (1986).

[37] L. C. Andreani in *Strong Light-Matter Coupling: From Atoms to Solid-State Systems*, A. Auffèves, D. Gerace, M. Richard, M. França Santos, S. Portolan, L. Ch. Kwek, Ch. Miniatura, (eds.), 37–82 (World Scientific, 2014).

[38] G. Günter, A. A. Anappara, J. Hees, A. Sell, G. Biasiol, L. Sorba, S. De Liberato, C. Ciuti, A. Tredicucci, A. Leitenstorfer, R. Huber, Nature **458**, 178 (2009).

[39] G. Scalari, C. Maissen, D. Turčinková, D. Hagenmüller, S. De Liberato, C. Ciuti, C. Reichl, D. Schuh, W. Wegscheider, M. Beck, J. Faist, Science **335**, 1323 (2012).

[40] C. Ciuti, G. Bastard, I. Carusotto, Phys. Rev. B **72**, 115303 (2005).

[41] D. Hagenmüller, S. De Liberato, C. Ciuti, Phys. Rev. B **81**, 235303 (2010).

[42] W. C. Tait, Phys. Rev. B **5**, 648 (1972).

[43] L. Schultheis, J. Kuhl, A. Honold, C. W. Tu, Phys. Rev. Lett. **57**, 1635 (1986).

[44] V. A. Kiselev, B. S. Razbirin, I. N. Uraltsev, physica status solidi (b) **72**, 161 (1975).

[45] D. D. Sell, S. E. Stokowski, R. Dingle, J. V. DiLorenzo, Phys. Rev. B **7**, 4568 (1973).

[46] D. Fröhlich, in *Nonlinear spectroscopy of solids*, B. Di Bartolo, (ed.), 289–326 (Plenum Press, 1994).

[47] V. Savona, L. C. Andreani, P. Schwendimann, A. Quattropani, Solid State Communications **93**, 733 (1995).

[48] A. V. Kavokin, J. J. Baumberg, G. Malpuech, F. P. Laussy, *Microcavities* (Oxford University Press, 2007).

[49] H. Deng, H. Haug, Y. Yamamoto, Rev. Mod. Phys. **82**, 1489 (2010).

[50] S. Gehrsitz, F. K. Reinhart, C. Gourgon, N. Herres, A. Vonlanthen, H. Sigg, Journal of Applied Physics **87**, 7825 (2000).

[51] G. Panzarini, L. C. Andreani, A. Armitage, D. Baxter, M. S. Skolnick, V. N. Astratov, J. S. Roberts, A. V. Kavokin, M. R. Vladimirova, M. A. Kaliteevski, Phys. Rev. B **59**, 5082 (1999).

[52] C. Klingshirn, *Semiconductor Optics* (Springer, 2005).

[53] B. Deveaud, F. Clérot, N. Roy, K. Satzke, B. Sermage, D. S. Katzer, Phys. Rev. Lett. **67**, 2355 (1991).

[54] Y. Chen, R. Cingolani, L.C. Andreani, F. Bassani, J. Massies, Il Nuovo Cimento D **10**, 847 (1988).

[55] C. W. Lai, N. Y. Kim, S. Utsunomiya, G. Roumpos, H. Deng, M. D. Fraser, T. Byrnes, P. Recher, N. Kumada, T. Fujisawa, Y. Yamamoto, Nature **450**, 529 (2007).

[56] T. B. Norris, J.-K. Rhee, C.-Y. Sung, Y. Arakawa, M. Nishioka, C. Weisbuch, Phys. Rev. B **50**, 14663 (1994).

[57] T. Fließbach, *Statistische Physik: Lehrbuch zur theoretischen Physik IV* (Spektrum, Akad. Verl., 2007).

[58] M. H. Anderson, J. R. Ensher, M. R. Matthews, C. E. Wieman, E. A. Cornell, Science **269**, 198 (1995).

[59] K. B. Davis, M. O. Mewes, M. R. Andrews, N. J. van Druten, D. S. Durfee, D. M. Kurn, W. Ketterle, Phys. Rev. Lett. **75**, 3969 (1995).

[60] S. Christopoulos, G. Baldassarri Höger von Högersthal, A. J. D. Grundy, P. G. Lagoudakis, A. V. Kavokin, J. J. Baumberg, G. Christmann, R. Butté, E. Feltin, J.-F. Carlin, N. Grandjean, Phys. Rev. Lett. **98**, 126405 (2007).

[61] F. Li, L. Orosz, O. Kamoun, S. Bouchoule, C. Brimont, P. Disseix, T. Guillet, X. Lafosse, M. Leroux, J. Leymarie, M. Mexis, M. Mihailovic, G. Patriarche, F. Réveret, D. Solnyshkov, J. Zuniga-Perez, G. Malpuech, Phys. Rev. Lett. **110**, 196406 (2013).

[62] J. D. Plumhof, Th. Stöferle, L. Mai, U. Scherf, R. F. Mahrt, Nat. Mat. **13**, 247 (2014).

[63] K. S. Daskalakis, S. A. Maier, R. Murray, S. Këna-Cohen, Nat. Mat. **13**, 271 (2014).

[64] F. Schwabl, *Quantenmechanik für Fortgeschrittene* (Springer, 1997).

[65] Lev Pitaevskii, Sandro Stringari, *Bose-Einstein Condensation* (Oxford Science Publications, 2003).

[66] F. Schwabl, *Quantenmechanik* (Springer, 1997).

[67] M. Wouters, I. Carusotto, Phys. Rev. Lett. **99**, 140402 (2007).

[68] M. Wouters, T. C. H. Liew, V. Savona, Phys. Rev. B **82**, 245315 (2010).

[69] E. Wertz, A. Amo, D. D. Solnyshkov, L. Ferrier, T. C. H. Liew, D. Sanvitto, P. Senellart, I. Sagnes, A. Lemaître, A. V. Kavokin, G. Malpuech, J. Bloch, Phys. Rev. Lett. **109**, 216404 (2012).

[70] F. Manni, K. G. Lagoudakis, T. C. H. Liew, R. André, B. Deveaud-Plédran, Phys. Rev. Lett. **107**, 106401 (2011).

[71] G. Christmann, G. Tosi, N. G. Berloff, P. Tsotsis, P. S. Eldridge, Z. Hatzopoulos, P. G. Savvidis, J. J. Baumberg, Phys. Rev. B **85**, 235303 (2012).

[72] K. G. Lagoudakis, F. Manni, B. Pietka, M. Wouters, T. C. H. Liew, V. Savona, A. V. Kavokin, R. André, B. Deveaud-Plédran, Phys. Rev. Lett. **106**, 115301 (2011).

[73] E. Kammann, T. C. H. Liew, H. Ohadi, P. Cilibrizzi, P. Tsotsis, Z. Hatzopoulos, P. G. Savvidis, A. V. Kavokin, P. G. Lagoudakis, Phys. Rev. Lett. **109**, 036404 (2012).

[74] S. Utsunomiya, L. Tian, G. Roumpos, C. W. Lai, N. Kumada, T. Fujisawa, M. Kuwata-Gonokami, A. Löffler, S. Höfling, A. Forchel, Y. Yamamoto, Nat. Phys. **4**, 700 (2008).

[75] M. Aßmann, J.-S. Tempel, F. Veit, M. Bayer, A. Rahimi-Iman, A. Löffler, S. Höfling, S. Reitzenstein, L. Worschech, A. Forchel, Proceedings of the National Academy of Sciences **108**, 1804 (2011).

[76] N. D. Mermin, H. Wagner, Phys. Rev. Lett. **17**, 1133 (1966).

[77] P. C. Hohenberg, Phys. Rev. **158**, 383 (1967).

[78] V. Bagnato, D. E. Pritchard, D. Kleppner, Phys. Rev. A **35**, 4354 (1987).

[79] V. Bagnato, D. Kleppner, Phys. Rev. A **44**, 7439 (1991).

[80] M. Gurioli, F. Bogani, D. S. Wiersma, Ph. Roussignol, G. Cassabois, G. Khitrova, H. Gibbs, Phys. Rev. B **64**, 165309 (2001).

[81] A. Kavokin, G. Malpuech, F. P. Laussy, Physics Letters A **306**, 187 (2003).

[82] V. L. Berezinskii, Sov. Phys. JETP **34**, 610 (1972).

[83] J. M. Kosterlitz, D. J. Thouless, Journal of Physics C: Solid State Physics **6**, 1181 (1973).

[84] Z. Hadzibabic, J. Dalibard, Rivista del Nuovo Cimento **34**, 389 (2011).

[85] Z. Hadzibabic, P. Krüger, M. Cheneau, B. Battelier, J. Dalibard, Nature **441**, 1118 (2006).

[86] L. V. Butov, A. V. Kavokin, Nat. Photon. **6**, 2 (2012).

[87] B. Deveaud-Plédran, Nat. Photon. **6**, 205 (2012).

[88] E. Wertz, L. Ferrier, D. D. Solnyshkov, R. Johne, D. Sanvitto, A. Lemaître, I. Sagnes, R. Grousson, A. V. Kavokin, P. Senellart, G. Malpuech, J. Bloch, Nat. Phys. **6**, 860 (2010).

[89] J. Schmutzler, D. Fröhlich, M. Bayer, Phys. Rev. B **87**, 245202 (2013).

[90] B. Di Bartolo, (ed.), *Nonlinear spectroscopy of solids* (Plenum Press, 1994).

[91] D. Fröhlich, E. Mohler, P. Wiesner, Phys. Rev. Lett. **26**, 554 (1971).

[92] P. D. Maker, R. W. Terhune, M. Nisenoff, C. M. Savage, Phys. Rev. Lett. **8**, 21 (1962).

[93] Y. R. Shen, *The principles of nonlinear optics* (John Wiley & Sons, 1984).

[94] R. W. Boyd, *Nonlinear Optics* (Academic Press, 1992).

[95] D. Fröhlich, A. Kulik, B. Uebbing, A. Mysyrowicz, V. Langer, H. Stolz, W. von der Osten, Phys. Rev. Lett. **67**, 2343 (1991).

[96] S. Denev, D. W. Snoke, Phys. Rev. B **65**, 085211 (2002).

[97] Ch. Sandfort, J. Brandt, Ch. Finke, D. Fröhlich, M. Bayer, H. Stolz, N. Naka, Phys. Rev. B **84**, 165215 (2011).

[98] R. Schwartz, N. Naka, F. Kieseling, H. Stolz, New Journal of Physics **14**, 023054 (2012).

[99] K. Yoshioka, E. Chae, M. Kuwata-Gonokami, Nat. Commun. **2**, 328 (2011).

[100] A. Daunois, J. L. Deiss, B. Meyer, J. Phys. France **27**, 142 (1966).

[101] S. Brahms, S. Nikitine, Solid State Communications **3**, 209 (1965).

[102] S. Brahms, S. Nikitine, J.P. Dahl, Physics Letters **22**, 31 (1966).

[103] T. Ito, T. Kawashima, H. Yamaguchi, T. Masumi, S. Adachi, Journal of the Physical Society of Japan **67**, 2125 (1998).

[104] D. Fröhlich, G. Dasbach, G. Baldassarri Höger von Högersthal, M. Bayer, R. Klieber, D. Suter, H. Stolz, Solid State Communications **134**, 139 (2005).

[105] F. K. Koster, J. O. Dimmock, R. G. Wheeler, H. Statz, *Properties of the thirty-two point groups* (M.I.T. Press, 1963).

[106] G. Dasbach, D. Fröhlich, R. Klieber, D. Suter, M. Bayer, H. Stolz, Phys. Rev. B **70**, 045206 (2004).

[107] D. Fröhlich, J. Brandt, C. Sandfort, M. Bayer, H. Stolz, physica status solidi (b) **243**, 2367 (2006).

[108] D. Fröhlich, J. Brandt, Ch. Sandfort, M. Bayer, H. Stolz, Phys. Rev. B **84**, 193205 (2011).

[109] M. O'Keeffe, The Journal of Chemical Physics **39**, 1789 (1963).

[110] J. Brandt, D. Fröhlich, Ch. Sandfort, M. Bayer, H. Stolz, N. Naka, Phys. Rev. Lett. **99**, 217403 (2007).

[111] L. N. Ovander, Soviet Physics Uspekhi **8**, 337 (1965).

[112] D. Fröhlich, E. Mohler, Ch. Uihlein, physica status solidi (b) **55**, 175 (1973).

[113] E. Burstein, F. De Martini, (eds.), *Polaritons* (Pergamon Press, 1974).

[114] R. Girlanda, S. Savasta, Solid State Communications **91**, 157 (1994).

[115] D. Fröhlich, A. Nöthe, K. Reimann, Phys. Rev. Lett. **55**, 1335 (1985).

[116] J. Schmutzler, F. Veit, M. Aßmann, J.-S. Tempel, S. Höfling, M. Kamp, A. Forchel, M. Bayer, Applied Physics Letters **102**, 081115 (2013).

[117] J. Schmutzler, M. Aßmann, Th. Czerniuk, M. Kamp, Ch. Schneider, S. Höfling, M. Bayer, Phys. Rev. B **90**, 075103 (2014).

[118] F. Tassone, C. Piermarocchi, V. Savona, A. Quattropani, P. Schwendimann, Phys. Rev. B **56**, 7554 (1997).

[119] M. G. A. Bernard, G. Duraffourg, physica status solidi (b) **1**, 699 (1961).

[120] D. Bajoni, Journal of Physics D: Applied Physics **45**, 313001 (2012).

[121] J. Bloch, B. Sermage, M. Perrin, P. Senellart, R. André, Le Si Dang, Phys. Rev. B **71**, 155311 (2005).

[122] G. Roumpos, C.-W. Lai, T. C. H. Liew, Y. G. Rubo, A. V. Kavokin, Y. Yamamoto, Phys. Rev. B **79**, 195310 (2009).

[123] N. F. Mott, Rev. Mod. Phys. **40**, 677 (1968).

[124] J.-S. Tempel, F. Veit, M. Aßmann, L. E. Kreilkamp, S. Höfling, M. Kamp, A. Forchel, M. Bayer, New Journal of Physics **14**, 083014 (2012).

[125] P. Tsotsis, P. S. Eldridge, T. Gao, S. I. Tsintzos, Z. Hatzopoulos, P. G. Savvidis, New Journal of Physics **14**, 023060 (2012).

[126] H. Franke, Ch. Sturm, R. Schmidt-Grund, G. Wagner, M. Grundmann, New Journal of Physics **14**, 013037 (2012).

[127] G. Christmann, R. Butté, E. Feltin, A. Mouti, P. A. Stadelmann, A. Castiglia, J.-F. Carlin, N. Grandjean, Phys. Rev. B **77**, 085310 (2008).

[128] P. Lagoudakis, Nat. Mat. **13**, 227 (2014).

[129] S. Schmitt-Rink, D. S. Chemla, D. A. B. Miller, Phys. Rev. B **32**, 6601 (1985).

[130] S. Schmitt-Rink, C. Ell, Journal of Luminescence **30**, 585 (1985).

[131] R. Houdré, J. L. Gibernon, P. Pellandini, R. P. Stanley, U. Oesterle, C. Weisbuch, J. O'Gorman, B. Roycroft, M. Ilegems, Phys. Rev. B **52**, 7810 (1995).

[132] L. Kappei, J. Szczytko, F. Morier-Genoud, B. Deveaud, Phys. Rev. Lett. **94**, 147403 (2005).

[133] R. Balili, V. Hartwell, D. Snoke, L. Pfeiffer, K. West, Science **316**, 1007 (2007).

[134] J. Fischer, S. Brodbeck, A. V. Chernenko, I. Lederer, A. Rahimi-Iman, M. Amthor, V. D. Kulakovskii, L. Worschech, M. Kamp, M. Durnev, Ch. Schneider, A. V. Kavokin, S. Höfling, Phys. Rev. Lett. **112**, 093902 (2014).

[135] J.-S. Tempel, F. Veit, M. Aßmann, L. E. Kreilkamp, A. Rahimi-Iman, A. Löffler, S. Höfling, S. Reitzenstein, L. Worschech, A. Forchel, M. Bayer, Phys. Rev. B **85**, 075318 (2012).

[136] E. Kammann, H. Ohadi, M. Maragkou, A. V. Kavokin, P. G. Lagoudakis, New Journal of Physics **14**, 105003 (2012).

[137] R. Butté, J. Levrat, G. Christmann, E. Feltin, J. F. Carlin, N. Grandjean, Phys. Rev. B **80**, 233301 (2009).

[138] J. Levrat, R. Butté, E. Feltin, J. F. Carlin, N. Grandjean, D. Solnyshkov, G. Malpuech, Phys. Rev. B **81**, 125305 (2010).

[139] J. Kasprzak, D. D. Solnyshkov, R. André, Le Si Dang, G. Malpuech, Phys. Rev. Lett. **101**, 146404 (2008).

[140] F. M. Marchetti, M. H. Szymańska, J. M. J. Keeling, J. Kasprzak, R. André, P. B. Littlewood, Le Si Dang, Phys. Rev. B **77**, 235313 (2008).

[141] E. Wertz, L. Ferrier, D. D. Solnyshkov, P. Senellart, D. Bajoni, A. Miard, A. Lemaître, G. Malpuech, J. Bloch, Applied Physics Letters **95**, 051108 (2009).

[142] J. S. Tempel, *Nonlinearities in Semiconductor Microcavities: A Correlation Spectroscopy Study*, Ph.D. thesis, TU Dortmund University (2013).

[143] M. Wouters, I. Carusotto, C. Ciuti, Phys. Rev. B **77**, 115340 (2008).

[144] V. D. Kulakovskii, A. V. Larionov, S. I. Novikov, Ch. Schneider, S. Höfling, A. Forchel, JEPT Letters **92**, 595 (2010).

[145] D. Bajoni, P. Senellart, A. Lemâitre, J. Bloch, Phys. Rev. B **76**, 201305 (2007).

[146] R. Balili, B. Nelsen, D. W. Snoke, L. Pfeiffer, K. West, Phys. Rev. B **79**, 075319 (2009).

[147] A. Das, J. Heo, M. Jankowski, W. Guo, L. Zhang, H. Deng, P. Bhattacharya, Phys. Rev. Lett. **107**, 066405 (2011).

[148] D. Bajoni, P. Senellart, E. Wertz, I. Sagnes, A. Miard, A. Lemaître, J. Bloch, Phys. Rev. Lett. **100**, 047401 (2008).

[149] M. Tonouchi, Nat. Photon. **1**, 97 (2007).

[150] B. Ferguson, X.-Ch. Zhang, Nat. Mater. **1**, 26 (2002).

[151] B. S. Williams, Nat. Photon. **1**, 517 (2007).

[152] Daniel M. Mittleman, Nat. Photon. **7**, 666 (2013).

[153] G. Leménager, F. Pisanello, J. Bloch, A. Kavokin, A. Amo, A. Lemaître, E. Galopin, I. Sagnes, M. De Vittorio, E. Giacobino, A. Bramati, Opt. Lett. **39**, 307 (2014).

[154] K. V. Kavokin, M. A. Kaliteevski, R. A. Abram, A. V. Kavokin, S. Sharkova, I. A. Shelykh, Applied Physics Letters **97**, 201111 (2010).

[155] M. Nithisoontorn, K. Unterrainer, S. Michaelis, N. Sawaki, E. Gornik, H. Kano, Phys. Rev. Lett. **62**, 3078 (1989).

[156] I. M. Catalano, A. Cingolani, R. Cingolani, M. Lepore, K. Ploog, Phys. Rev. B **40**, 1312 (1989).

[157] I. M. Catalano, A. Cingolani, M. Lepore, R. Cingolani, K. Ploog, Phys. Rev. B **41**, 12937 (1990).

[158] K. Tai, A. Mysyrowicz, R. J. Fischer, R. E. Slusher, A. Y. Cho, Phys. Rev. Lett. **62**, 1784 (1989).

[159] J. M. Ménard, C. Poellmann, M. Porer, U. Leierseder, E. Galopin, A. Lemaïtre, A. Amo, J. Bloch, R. Huber, Nat. Commun. **5**, 4648 (2014).

[160] V. V. Pavlov, A. M. Kalashnikova, R. V. Pisarev, I. Sänger, D. R. Yakovlev, M. Bayer, Phys. Rev. Lett. **94**, 157404 (2005).

[161] J. Schmutzler, T. Kazimierczuk, Ö. Bayraktar, M. Aßmann, M. Bayer, S. Brodbeck, M. Kamp, Ch. Schneider, S. Höfling, Phys. Rev. B **89**, 115119 (2014).

[162] Ö. Bayraktar, *Propagations- und Kohärenzeigenschaften von Polaritonkondensaten*, Bachelor's thesis, TU Dortmund University (2013).

[163] A. Askitopoulos, H. Ohadi, A. V. Kavokin, Z. Hatzopoulos, P. G. Savvidis, P. G. Lagoudakis, Phys. Rev. B **88**, 041308 (2013).

[164] H. Deng, G. S. Solomon, R. Hey, K. H. Ploog, Y. Yamamoto, Phys. Rev. Lett. **99**, 126403 (2007).

[165] V. V. Belykh, N. N. Sibeldin, V. D. Kulakovskii, M. M. Glazov, M. A. Semina, Ch. Schneider, S. Höfling, M. Kamp, A. Forchel, Phys. Rev. Lett. **110**, 137402 (2013).

[166] J. Wiersig, C. Gies, F. Jahnke, M. Aßmann, T. Berstermann, M. Bayer, C. Kistner, S. Reitzenstein, Ch. Schneider, S. Höfling, A. Forchel, C. Kruse, J. Kalden, D. Hommel, Nature **460**, 245 (2009).

[167] M. Aßmann, F. Veit, J.-S. Tempel, Th. Berstermann, H. Stolz, M. van der Poel, J. M. Hvam, M. Bayer, Opt. Express **18**, 20229 (2010).

[168] R. J. Glauber, Phys. Rev. **130**, 2529 (1963).

[169] G. Roumpos, M. Lohse, W. H. Nitsche, J. Keeling, M. H. Szymańska, P. B. Littlewood, A. Löffler, S. Höfling, L. Worschech, A. Forchel, Y. Yamamoto, Proceedings of the National Academy of Sciences **109**, 6467 (2012).

[170] T. H. Maiman, Nature **187**, 493 (1960).

[171] R. Hanbury Brown, R. Q. Twiss, Nature **177**, 27 (1956).

[172] J. A. Armstrong, Archibald W. Smith, Phys. Rev. Lett. **14**, 68 (1965).

[173] M. Aßmann, *Photon Statistics of Semiconductor Light Sources*, Ph.D. thesis, TU Dortmund University (2010).

[174] C. Cohen-Tannoudji, B. Diu, F. Laloë, *Quantenmechanik* (Walter de Gruyter, 2007).

[175] R. J. Glauber, Phys. Rev. **131**, 2766 (1963).

[176] M. Aßmann, F. Veit, M. Bayer, M. van der Poel, J. M. Hvam, Science **325**, 297 (2009).

[177] G. Dasbach, M. Schwab, M. Bayer, D.N. Krizhanovskii, A. Forchel, Phys. Rev. B **66**, 201201 (2002).

[178] A. Kuther, M. Bayer, T. Gutbrod, A. Forchel, P. A. Knipp, T. L. Reinecke, R. Werner, Phys. Rev. B **58**, 15744 (1998).

[179] T. Lecomte, V. Ardizzone, M. Abbarchi, C. Diederichs, A. Miard, A. Lemaître, I. Sagnes, P. Senellart, J. Bloch, C. Delalande, J. Tignon, Ph. Roussignol, Phys. Rev. B **87**, 155302 (2013).

[180] K. Kusudo, N. Y. Kim, A. Löffler, S. Höfling, A. Forchel, Y. Yamamoto, Phys. Rev. B **87**, 214503 (2013).

[181] R. Spano, J. Cuadra, G. Tosi, C. Antón, C. A. Lingg, D. Sanvitto, M. D. Martín, L. Viña, P. R. Eastham, M. van der Poel, J. M. Hvam, New Journal of Physics **14**, 075018 (2012).

[182] F. Manni, K. G. Lagoudakis, B. Pietka, L. Fontanesi, M. Wouters, V. Savona, R. André, B. Deveaud-Plédran, Phys. Rev. Lett. **106**, 176401 (2011).

[183] J. Schmitt, T. Damm, D. Dung, F. Vewinger, J. Klaers, M. Weitz, Phys. Rev. Lett. **112**, 030401 (2014).

[184] M. Aßmann, F. Veit, M. Bayer, A. Löffler, S. Höfling, M. Kamp, A. Forchel, Phys. Rev. B **85**, 155320 (2012).

[185] B. Nelsen, G. Liu, M. Steger, D. W. Snoke, R. Balili, K. West, L. Pfeiffer, Phys. Rev. X **3**, 041015 (2013).

[186] T. Gao, P. S. Eldridge, T. C. H. Liew, S. I. Tsintzos, G. Stavrinidis, G. Deligeorgis, Z. Hatzopoulos, P. G. Savvidis, Phys. Rev. B **85**, 235102 (2012).

[187] H. S. Nguyen, D. Vishnevsky, Ch. Sturm, D. Tanese, D. Solnyshkov, E. Galopin, A. Lemaître, I. Sagnes, A. Amo, G. Malpuech, J. Bloch, Phys. Rev. Lett. **110**, 236601 (2013).

[188] P. Cristofolini, A. Dreismann, G. Christmann, G. Franchetti, N. G. Berloff, P. Tsotsis, Z. Hatzopoulos, P. G. Savvidis, J. J. Baumberg, Phys. Rev. Lett. **110**, 186403 (2013).

[189] T. C. H. Liew, A. V. Kavokin, I. A. Shelykh, Phys. Rev. Lett. **101**, 016402 (2008).

[190] T. Espinosa-Ortega, T. C. H. Liew, Phys. Rev. B **87**, 195305 (2013).

[191] F. Veit, M. Aßmann, M. Bayer, A. Löffler, S. Höfling, M. Kamp, A. Forchel, Phys. Rev. B **86**, 195313 (2012).

[192] C. Antón, T. C. H. Liew, G. Tosi, M. D. Martín, T. Gao, Z. Hatzopoulos, P. S. Eldridge, P. G. Savvidis, L. Viña, Phys. Rev. B **88**, 035313 (2013).

[193] V. Ardizzone, P. Lewandowski, M. H. Luk, Y. C. Tse, N. H. Kwong, A. Lücke, M. Abbarchi, E. Baudin, E. Galopin, J. Bloch, A. Lemaître, P. T. Leung, P. Roussignol, R. Binder, J. Tignon, S. Schumacher, Scientific Reports **3**, 3016 (2013).

[194] H. Haug, T. D. Doan, D. B. Tran Thoai, Phys. Rev. B **89**, 155302 (2014).

Publications and conference contributions

List of publications

1. **Johannes Schmutzler**, Dietmar Fröhlich, and Manfred Bayer.
   Signatures of coherent propagation of blue polaritons in Cu_2O.
   Physical Review B **87**, 245202 (2013).

2. **Johannes Schmutzler**, Franziska Veit, Marc Aßmann, Jean-Sebastian Tempel, Sven Höfling, Martin Kamp, Alfred Forchel, and Manfred Bayer.
   Determination of operating parameters for a GaAs-based polariton laser.
   Applied Physics Letters **102**, 081115 (2013).

3. **Johannes Schmutzler**, Tomasz Kazimierczuk, Ömer Bayraktar, Marc Aßmann, Sebastian Brodbeck, Martin Kamp, Christian Schneider, Sven Höfling, and Manfred Bayer.
   Influence of interactions with noncondensed particles on the coherence of a one-dimensional polariton condensate.
   Physical Review B **89**, 115119 (2014).

4. **Johannes Schmutzler**, Marc Aßmann, Thomas Czerniuk, Martin Kamp, Christian Schneider, and Sven Höfling, and Manfred Bayer.
   Nonlinear spectroscopy of exciton-polaritons in a GaAs-based microcavity.
   Physical Review B **90**, 075103 (2014).

5. **Johannes Schmutzler**, Przemyslaw Lewandowski, Marc Aßmann, Dominik Niemietz, Stefan Schumacher, Martin Kamp, Christian Schneider, Sven Höfling, and Manfred Bayer.
   All-optical flow control of a polariton condensate using only non-resonant excitation.
   Physical Review Letters, submitted.

Conference contributions

- September 2012: **Poster**, 11th International Workshop on Nonlinear Optics and Excitation Kinetics in Semiconductors (NOEKS), Stuttgart, Germany. *Double resonant sum-frequency generation in* Cu_2O.

- March 2013: **Regular talk**, DPG Spring Meeting of the Condensed Matter Section, Regensburg, Germany. *Coherent Propagation of blue Polaritons in* Cu_2O.
- April 2014: **Regular talk**, DPG Spring Meeting of the Condensed Matter Section, Dresden, Germany. *Determination of operating parameters for a GaAs-based polariton laser.*
- June 2014: **Regular talk**, Conference on Lasers and Electro-Optics (CLEO), San José, USA. *Influence of interactions with noncondensed particles on the coherence of a one-dimensional polariton condensate.*
- September 2014: **Regular talk**, 12th International Workshop on Nonlinear Optics and Excitation Kinetics in Semiconductors (NOEKS), Bremen, Germany. *Steering and manipulation of a polariton condensate using non-resonant laser excitation.*

Acknowledgments

Finally, I would like to thank many people who contributed to the research projects presented in this thesis and allowed me to have a great time in our physics department:

- Prof. Dr. Manfred Bayer for supervising my thesis, providing a great research environment and supporting my research projects.
- Prof. Dr. Dietmar Fröhlich for giving me so many insights into polariton physics and nonlinear spectroscopy, for explaining and demonstrating how to write a paper, for showing me so many tricks in the Lab and for the idea of approaching the blue-polariton in Cu_2O by sum-frequency generation.
- Dr. Marc A. Aßmann for supervising the microcavity related part of my thesis, for proofreading my thesis, countless valuable discussions and sharing his comprehensive knowledge regarding polariton related literature.
- Dr. Tomasz Kazimierczuk for his idea to operate the streak camera in a HBT-like approach, for code-writing and showing me several tricks in the Lab.
- Dr. Franziska Wishahi for introducing me into the spectroscopic techniques of the Correlation Lab and coworking on my first microcavity polariton project.
- Dr. Jean-Sebastian Tempel for proofreading an APL manuscript and giving valuable suggestions for the improvement of the storyline.
- Dr. Jörg Debus for sharing his comprehensive Lab know-how.
- Jun.-Prof. Dr. Stefan Schumacher and Przemyslaw Lewandowski for the numerical simulations of the polariton flow patterns and several valuable discussions.
- Thomas Czerniuk for performing Transfer-Matrix calculations.
- Dr. David Brunne for proofreading my thesis and giving me support for measurements performed in the OPO Lab.
- Lars Erik Kreilkamp for proofreading my thesis.
- Ömer Bayraktar for his valuable contribution to the photonic wire project.
- Dominik Niemietz for his great ongoing work on the polariton flow experiments.
- Benjamin Siebers, Philipp Glasenapp, Louis Biadala and Yasin Beyazit for a great and cooperative atmosphere in the office.

- Michaela Wäscher for her great patience with me, when I struggled with placing orders the correct way and other administrative issues...
- Lars Wieschollek and Thomas Stöhr for valuable technical support.
- Klaus Wiegers for his composure when getting asked again and again "Do we get Helium today? How is the machine running?"
- all E2-members for the fabulous atmosphere and for all the great activities (bicycle tours, barbecues, PHD defense preparation and parties, soccer games).